© 2022. Published by The Company of Biologists Ltd | Journal of Cell Science (2022) 135, jcs259178. doi:10.1242/jcs.259178

RESEARCH ARTICLE

Upregulated flotillins and sphingosine kinase 2 derail AXL vesicular traffic to promote epithelial-mesenchymal transition

Mallory Genest[1], Franck Comunale[1], Damien Planchon[1], Pauline Govindin[1], Dune Noly[1], Sophie Vacher[2], Ivan Bièche[2], Bruno Robert[3], Himanshu Malhotra[1], Andreas Schoenit[1], Liubov A. Tashireva[4], Josefina Casas[5,6], Cécile Gauthier-Rouvière[1,*,‡] and Stéphane Bodin[1,*,‡]

ABSTRACT

Altered endocytosis and vesicular trafficking are major players during tumorigenesis. Flotillin overexpression, a feature observed in many invasive tumors and identified as a marker of poor prognosis, induces a deregulated endocytic and trafficking pathway called upregulated flotillin-induced trafficking (UFIT). Here, we found that in non-tumoral mammary epithelial cells, induction of the UFIT pathway promotes epithelial-to-mesenchymal transition (EMT) and accelerates the endocytosis of several transmembrane receptors, including AXL, in flotillin-positive late endosomes. AXL overexpression, frequently observed in cancer cells, is linked to EMT and metastasis formation. In flotillin-overexpressing non-tumoral mammary epithelial cells and in invasive breast carcinoma cells, we found that the UFIT pathway-mediated AXL endocytosis allows its stabilization and depends on sphingosine kinase 2, a lipid kinase recruited in flotillin-rich plasma membrane domains and endosomes. Thus, the deregulation of vesicular trafficking following flotillin upregulation, and through sphingosine kinase 2, emerges as a new mechanism of AXL overexpression and EMT-inducing signaling pathway activation.

KEY WORDS: Flotillins, AXL, Endosomal trafficking, Sphingosine kinase 2, Epithelial to mesenchymal transition, Cancer

INTRODUCTION

Aberrant reactivation of epithelial-to-mesenchymal (EMT) transition, an essential embryonic process that is also crucial for tumor initiation and metastatic cancer cell dissemination (reviewed by Dongre and Weinberg, 2018), is a key step in cancer progression. EMT induction is orchestrated by a family of EMT-inducing transcription factors (e.g. ZEB1, ZEB2, Snail1 and Slug) that are regulated by multiple signaling pathways [e.g. TGFβ receptors and receptor tyrosine kinases (RTKs)] and the downstream signaling Ras/MAPK and phosphoinositide 3-kinase (PI3K)/AKT pathways (Puisieux et al., 2014). Because of EMT pleiotropic roles in the acquisition of invasive properties and therapeutic resistance, it is important to identify new inducers of this cellular program.

For example, AXL, a member of the TAM (Tyro3, AXL and Mer) family of RTKs, is an attractive candidate target for anticancer therapies (reviewed by Zhu et al., 2019). AXL expression is low in normal adult tissues, but is overexpressed in several tumors. This correlates negatively with overall survival. In many tumors, aberrant AXL expression is associated with EMT, invasion, metastasis formation, cell proliferation, tumor angiogenesis, reduced anti-cancer immune response, stem cell maintenance and treatment resistance (Gjerdrum et al., 2010; Gay et al., 2017). AXL is activated through several mechanisms, including binding to its ligand GAS6, homodimerization when overexpressed and crosstalk with other RTKs (Gay et al., 2017). However, the rarity of AXL genetic mutations and amplification events, despite its upregulation in many tumor types, suggests that AXL expression is mainly regulated by post-transcriptional/translational modifications.

The endosomal system accumulates activated receptors and signaling molecules. Endocytosis was considered for many years to be only a means of limiting signal transduction; however, its crucial role in maintaining and even generating signaling cascades is now acknowledged (Dobrowolski and De Robertis, 2008; Murphy et al., 2009). Deregulation of vesicular trafficking, particularly endocytosis, has emerged as a major player in tumorigenesis (Mellman and Yarden, 2013; Schmid, 2017). Consistently, upregulation of flotillin 1 and/or 2, two proteins involved in the formation of membrane invaginations, is a common feature of many invasive tumors and a poor prognostic marker (Berger et al., 2013; Pust et al., 2013; Zhao et al., 2015; Cao et al., 2016; Gauthier-Rouvière et al., 2020). When co-upregulated, flotillins promote plasma membrane (PM) invaginations, and favor an endocytic pathway called upregulated flotillin-induced trafficking (UFIT) (Glebov et al., 2006; Frick et al., 2007; Babuke et al., 2009) that targets protein cargos to non-degradative late endosomes (LEs) where flotillins accumulate (Dermine et al., 2001; Neumann-Giesen et al., 2007; Langhorst et al., 2008; Planchon et al., 2018). Several studies have reported that, in cancer cells, flotillins influence the activation of signaling pathways that promote EMT and cellular invasion, and that they are scaffolding factors for several signaling molecules (Amaddii et al., 2012). Therefore, the UFIT pathway, which is at the crossroads between endocytosis and signaling, has emerged as a crucial mechanism in the regulation of oncogenic pathways.

Here, to study the contribution of flotillin-induced deregulation of the endosomal system to EMT, we have reproduced the flotillin 1 and 2 co-upregulation observed in tumors in non-tumoral mammary cell lines (MCF10A and NMuMG) with low endogenous flotillin levels. Indeed, previous studies on the role of flotillin in EMT and cell invasion (Zhao et al., 2015; Cao et al., 2016) did not allow the determination of the exact contribution of flotillin upregulation and

[1]CRBM, University of Montpellier, CNRS, 1919 route de Mende, 34293 Montpellier, France. [2]Department of Genetics, Institut Curie, Paris 75005, France. [3]IRCM, Campus Val d'Aurelle, 208 avenue des Apothicaires, 34298 Montpellier, France. [4]Cancer Research Institute, Tomsk National Research Medical Center, Russian Academy of Sciences, Tomsk 634050, Russia. [5]Research Unit on BioActive Molecules (RUBAM), Department of Biological Chemistry, Institute for Advanced Chemistry of Catalonia (IQAC), Spanish Council for Scientific Research (CSIC), 08034 Barcelona, Spain. [6]Liver and Digestive Diseases Networking Biomedical Research Centre (CIBER-EHD), 28029 Madrid, Spain.
*These authors contributed equally to this work

‡Authors for correspondence (stephane.bodin@crbm.cnrs.fr; cecile.gauthier@crbm.cnrs.fr)

A.S., 0000-0003-3714-5636; S.B., 0000-0003-0926-403X

Handling Editor: Kathleen Green
Received 21 July 2021; Accepted 15 February 2022

Journal of Cell Science (2022) 135, jcs259178. doi:10.1242/jcs.259178

of the molecular mechanisms because they were carried out using cancer cell lines harboring several mutations in signaling and structural genes that promote EMT and invasion. In non-tumoral cells, we found that flotillin upregulation was sufficient to promote EMT and to activate key oncogenic signaling pathways. We identified AXL as a major contributor to flotillin upregulation-induced EMT. We showed that the UFIT pathway promotes AXL endocytosis towards flotillin-positive LEs and AXL stabilization, leading to its overexpression. Finally, in non-tumoral cell lines, where flotillins are upregulated, and in invasive breast cancer cells, where flotillins are endogenously overexpressed, AXL stabilization by the UFIT pathway depends on the sphingosine kinase 2 (SPHK2) that produces the bioactive lipid sphingosine 1-phosphate (S1P), a key signaling component of the sphingolipid metabolic network during tumorigenesis.

RESULTS

Flotillin upregulation in non-tumoral mammary epithelial cells induces EMT

To precisely determine the role of flotillin upregulation in EMT and the implicated molecular mechanisms, we used non-tumoral epithelial cell lines (human MCF10A and murine NMuMG) in which oncogenic pathways are not activated and endogenous flotillin expression levels are low. From these two cell lines, we generated stable cell lines (MFC10AF1F2 and NMuMGF1F2) that express flotillins at levels similar to those observed in MDA-MB-231 invasive breast cancer cells (Fig. S1A-C; Planchon et al., 2018).

First, to identify the gene expression changes and the downstream signaling pathways associated with flotillin upregulation, we compared, using RNA-sequencing (RNA-seq), the expression profiles of control MCF10AmCh cells (transfected with empty mCherry vector, mCh) and MCF10AF1F2 cells (transfected with flotillin 1-HA and flotillin 2-mCherry). Using two differential gene expression analysis pipelines (Tuxedo and DSeq2), we identified 232 upregulated and 570 downregulated genes (fold change 2.8, $P<0.05$) in MCF10AF1F2 cells compared with control cells (Table S1). Gene ontology (GO) cluster analysis (Fig. 1A) revealed that flotillin upregulation was associated with deregulation of genes involved in extracellular matrix, cell adhesion, migration, differentiation, apoptosis and signaling pathways, particularly MAP kinases. These processes are often deregulated during tumor development and particularly during EMT.

We compared the list of genes differentially expressed between MCF10AmCh and MCF10AF1F2 cells with the EMT transcriptional signature previously established by a meta-analysis that combined 18 independent gene expression studies on EMT induced by different treatments in different cell types (Gröger et al., 2012). In this EMT signature, 22/67 of the upregulated genes and 39/62 of the downregulated genes overlapped with the genes deregulated upon flotillin overexpression (Fig. 1B). We also confirmed the enrichment of the EMT signature in our ranked transcriptome profile by gene set enrichment analysis (GSEA) (Fig. 1C). The analysis of the top 20 up- and downregulated genes between MCF10AmCh and MCF10AF1F2 cells highlighted the decreased expression of E-cadherin and occludin, and the increased expression of ZEB1, fibronectin, vimentin and N-cadherin (Fig. 1D).

We validated these results in MCF10AF1F2 and NMuMGF1F2 cells by RT-qPCR (Fig. 1E and Fig. S1D), western blotting and immunocytochemistry analysis (Fig. 1F-H and Fig. S1E-G). We confirmed the downregulation (mRNA and protein) of the hallmark epithelial marker E-cadherin (Fig. 1E-G and Fig. S1D-F) and of the polarity marker ZO-1 (also known as TJP1) (Fig. 1H and Fig. S1G), and the upregulation of the mesenchymal markers N-cadherin and vimentin (Fig. 1E-G and Fig. S1D,G). Morphological analysis by scanning electron microscopy and F-actin cytoskeleton staining showed that cell polarity was lost in NMuMGF1F2 cells and in MCF10AF1F2 cells compared with NMuMGmCh cells and with MCF10AmCh cells, respectively (Fig. S1H-J).

Several transcription factors can inhibit E-cadherin expression (De Craene and Berx, 2013). Flotillin upregulation specifically induced ZEB1 and ZEB2 mRNA expression (Fig. 1I and Fig. S1K,L), and ZEB1 protein expression (Fig. 1J and Fig. S1M). ZEB1 localized in the nucleus (Fig. 1K and Fig. S1N). ZEB1 and ZEB2 knockdown in MCF10AF1F2 cells restored E-cadherin expression (Fig. 1J) and its accumulation at cell-cell contacts (Fig. 1L). This demonstrated the key role of ZEB1 and ZEB2 in E-cadherin downregulation upon flotillin upregulation. In conclusion, flotillin upregulation in non-tumoral mammary epithelial cells is sufficient to induce EMT.

Flotillin upregulation in non-tumoral mammary epithelial cells is sufficient to activate several oncogenic signaling pathways

The GO analysis of the genes differentially expressed between control and flotillin-upregulated MCF10A cells revealed a strong association with signal transduction pathways involving transmembrane RTKs and the MAPK pathway (Fig. 1A). Different bioinformatics analysis identified the PI3-K/AKT and Ras pathways: two major oncogenic signaling cascades (Table S2). In agreement, analysis using the human phospho-kinase array revealed the increased phosphorylation of at least four main tyrosine and serine/threonine kinases involved in oncogenic pathways [ERK1 and ERK2 (ERK1/2; also known as MAPK3 and MAPK1, respectively), FAK (also known as PTK2), AKT family proteins and Fyn] and of their substrates [Hsp27 (also known as HSPB1) and STAT] (Fig. 2A). We demonstrated Ras activation in MCF10AF1F2 cells (Fig. 2B), as well as ERK1/2, PI3K/AKT and STAT3 activation (Fig. 2C, Fig. S2A for NMuMG cells, Fig. 2D-F).

In MCF10A cells, expression of a hyperactive H-Ras mutant or its downstream effector PI3-K leads to ZEB1 and ZEB2-dependent E-cadherin downregulation and EMT via the transcriptional repression of ΔNp63α, the predominant p63 (also known as TP63) isoform in MCF10A cells (Yoh et al., 2016). In these cells, ΔNp63α downregulation is an EMT marker (Yoh et al., 2016; Hu et al., 2017). Flotillin upregulation in MCF10A cells led to the reduction of ΔNp63α and ΔNp63β expression (Fig. 2G,H and Fig. S2B; Table S1). We excluded the involvement of ZEB1 and ZEB2 in ΔNp63α downregulation through a negative feed-back loop because ZEB1 and ZEB2 knockdown did not rescue ΔNp63α expression in MCF10AF1F2 cells (Fig. 2H). Moreover, data obtained from a previously described (Planchon et al., 2018) cohort of 527 individuals with breast cancer indicated that flotillin 1 and ΔNp63 mRNA expression levels were negatively correlated (Fig. 2I).

High TGFβ signaling pathway activity contributes to tumor development and to EMT induction (Dongre and Weinberg, 2018). Flotillins participate in its activation in nasopharyngeal carcinoma (Zhao et al., 2015; Cao et al., 2016). Here, we found that flotillin upregulation in non-tumoral cells activated TGFβ signaling, as indicated by the higher SMAD3 phosphorylation (Fig. 2J and Fig. S2C) and the nuclear localization of phosphorylated SMAD3 in MCF10AF1F2 (Fig. 2K) and NMuMGF1F2 (Fig. S2D) cells compared with control cells (mCh).

We never detected activation of the NF-κB and WNT canonical pathways (Fig. S2E-G), although several oncogenic pathways were activated upon flotillin upregulation. Altogether, these data

Journal of Cell Science (2022) 135, jcs259178. doi:10.1242/jcs.259178

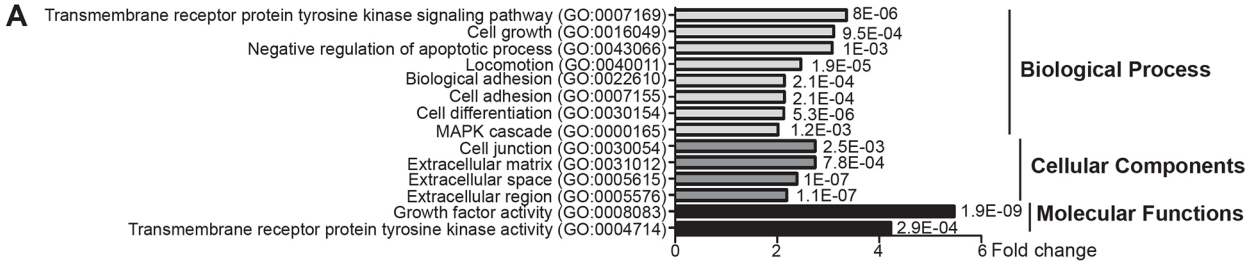

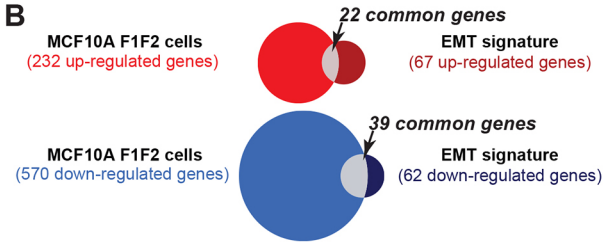

D

Top upregulated genes

	Symbol	Fold up	*P-value*
1	CTGF	14,811	3.81E-40
2	SERPINE2	12,754	3.88E-33
3	SRGN	5,557	3.74E-19
4	**ZEB1**	5,462	1.38E-16
5	**FN1**	17,147	2.21E-13
6	MAP1B	12,223	5.92E-13
7	NRZF1	6,466	5.59E-12
8	MMP2	8,789	7.51E-12
9	HAS2	9,963	9.37E-12
10	**VIM**	3.529	2.12E-11
11	FBLN5	8.92	8.18E-11
12	FBN1	7.881	1.93E-10
13	SPOCK1	8.295	1.56E-9
14	FGF2	3.053	2.70E-9
15	DCN	6.926	3.01E-7
16	DLC1	3.997	1.09E-6
17	**CDH2**	3.288	1.96E-6
18	PTX3	4.352	7.84E-5
19	WTN5A	3.132	2.11E-4
20	LUM	4.123	3.52E-4

Top downregulated genes

	Symbol	Fold down	*P-value*
1	DSG3	0.017	1.48E-107
2	EPCAM	0.020	3.77E-94
3	**CDH1**	0.006	3.13E-90
4	MPZL2	0.077	4.99E-62
5	LAD1	0.006	5.19E-56
6	TSPAN1	0.026	2.57E-54
7	SLC27A2	0.037	1.52E-51
8	FGFR2	0.071	3.76E-30
9	CDS1	0.134	9.03E-30
10	FGFR3	0.113	3.53E-29
11	LSR	0.043	3.29E-28
12	CXADR	0.057	5.02E-28
13	**OCLN**	0.034	3.83E-25
14	PRSS8	0.043	7.19E-25
15	KRT17	0.066	1.96E-19
16	RAPGEF5	0.105	1.17E-17
17	ST6GALNAC2	0.088	1.47E-16
18	IFI30	0.199	1.60E-16
19	ANK3	0.180	4.03E-15
20	SPINT1	0.252	6.98E-15

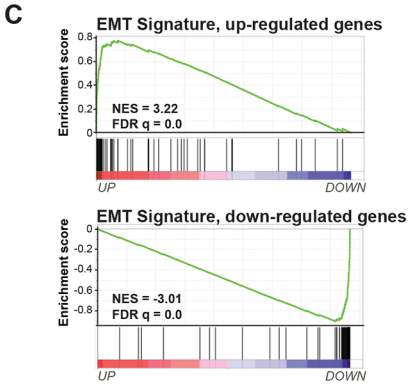

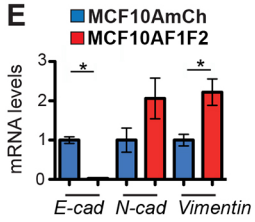

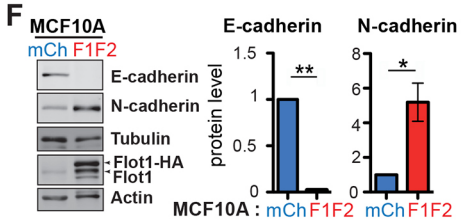

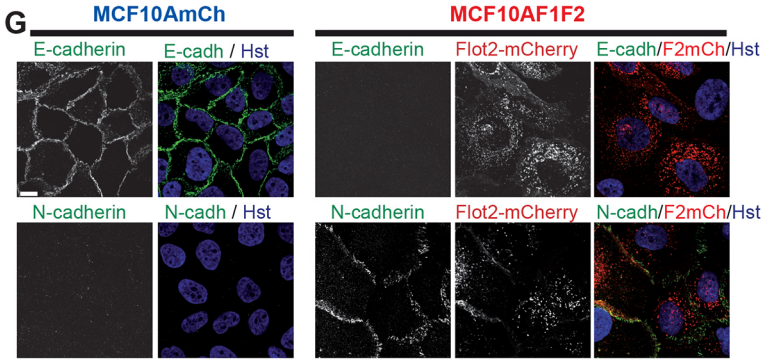

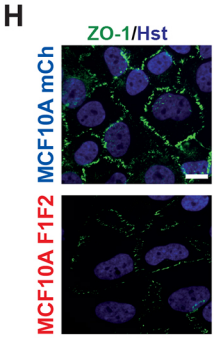

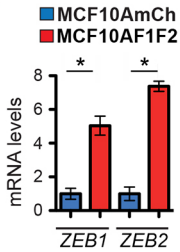

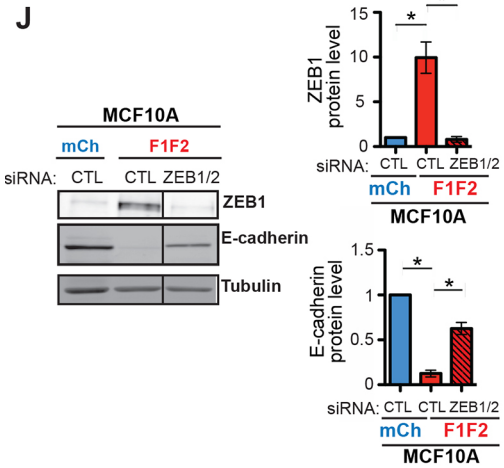

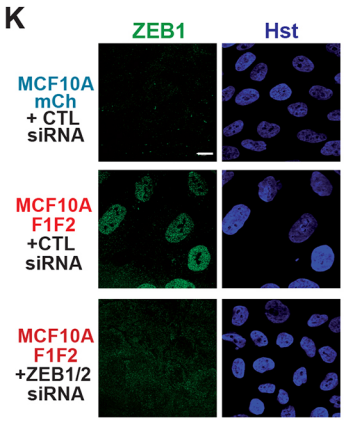

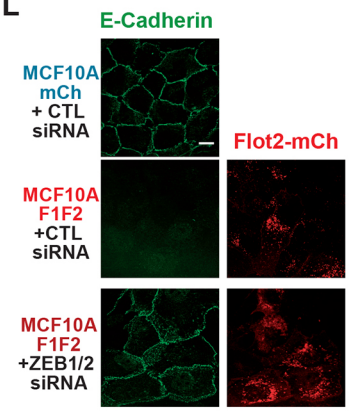

Fig. 1. See next page for legend.

Journal of Cell Science

Journal of Cell Science (2022) 135, jcs259178. doi:10.1242/jcs.259178

Fig. 1. Flotillin upregulation in non-tumoral epithelial mammary MCF10A cells induces EMT. (A) GO identification of the biological process, cellular component and molecular function terms associated with the 802 genes differentially expressed in MCF10AF1F2 versus MCF10AmCh cells. (B) Venn diagrams comparing the up- or downregulated (> or <2.8, P<0.05) genes identified by RNA-seq data analysis in MCF10AF1F2 versus MCF10AmCh cells with the EMT signature established by Gröger et al. (2012). (C) GSEA plots showing the enriched EMT-signature genes (upregulated, upper panel; downregulated, lower panel) in the ranked transcriptome profile. Green lines represent enrichment profiles. NES, normalized enrichment score; FDR, false discovery rate. Each hit from the EMT signature is represented by a vertical black bar, positioned along the ranked transcriptome profile with color-coded fold-change values. (D) List of genes with the highest fold-change among the genes up- and downregulated in MCF10AF1F2 cells and also found in the EMT-transcriptomic signature (Gröger et al., 2012). *P*-values were adjusted for multiple testing using the Benjamini-Hochberg procedure. (E) RT-qPCR analysis of E-cadherin, N-cadherin and vimentin in MCF10AmCh and MCF10AF1F2 cells. Data are mean±s.e.m. of four independent experiments. (F) Western blotting of E- and N-cadherin, tubulin and flotillin 1 in MCF10AmCh and MCF10AF1F2 cell lysates. Data are mean±s.e.m. of at least four independent experiments. (G,H) Confocal images showing the distribution of E- and N-cadherin, flotillin 2-mCherry and ZO-1 in MCF10AmCh and MCF10AF1F2 cells and of vimentin in NMuMGmCh and NMuMGF1F2 cells (immunocytochemistry analysis). Nuclei were stained with Hoechst (Hst; blue). In G, for vimentin, the *z* projection corresponds to the stacked signal of 30 planes performed every 0.3 µm. (I) RT-qPCR analysis of *ZEB1* and *ZEB2* in MCF10AmCh and MCF10AF1F2 cells. Data are mean±s.e.m. of four independent experiments. (J) Western blotting of ZEB1, E-cadherin and α-tubulin in lysates from MCF10AmCh and MCF10AF1F2 cells transfected with siRNAs against ZEB1 and ZEB2 or control siRNA against luciferase (CTL). Data are mean±s.e.m. of four independent experiments. (K,L) ZEB1 (K) and E-cadherin (L) distribution in MCF10AmCh cells and in ZEB1/2 siRNA- or CTL siRNA-transfected MCF10AF1F2 cells analyzed by immunofluorescence. In K, nuclei were stained with Hoechst (Hst). Images in G, H, K and L are representative of three independent experiments. Scale bars: 10 µm. *P<0.05, **P<0.01 (Mann-Whitney test, two-tailed *P*-values).

demonstrate that flotillin upregulation in cells without oncogenic mutations is sufficient to activate major oncogenic pathways, such as the Ras/ERK MAP kinase, AKT and TGFβ signaling cascades.

Flotillin upregulation in non-tumoral mammary epithelial cells increases the expression of AXL, a key player in flotillin-induced EMT

To identify how flotillin upregulation in non-tumoral mammary cells activates these oncogenic signaling pathways, we used a phospho-RTK array to simultaneously screen 49 tyrosine-phosphorylated RTKs. The tyrosine phosphorylation of 11 RTKs was increased by >1.4-fold in MCF10AF1F2 cells compared with MCF10AmCh cells (Fig. S2H,I). To validate these results for the three top receptors, we wanted to compare their Y-phosphorylation status in the two cell lines by western blotting using antibodies against phosphorylation at specific Y residues. Unfortunately, the available antibodies allowed us to validate this result only for AXL, but not for EphA4 and ALK. AXL phosphorylation was increased (2.53±0.71-fold) in MCF10AF1F2 cells compared with control MCF10AmCh cells, as was the AXL protein level (2.57±0.61-fold versus control) (Fig. 3A). The identical phospho-Y702 AXL/AXL ratio in MCF10AmCh and MCF10AF1F2 cells indicated that flotillin upregulation increased AXL protein levels but did not stimulate AXL phosphorylation (Fig. 3A). The expression level of the transferrin receptor CD71 (also known as TFRC) was comparable in both cell lines (Fig. S3A). We detected increased AXL level in cells grown in the presence of serum (Fig. S3B), which might contain its ligand GAS6, and also in serum-starved cells, indicating that flotillin upregulation promotes an increase in the AXL level in MCF10A cells independently of GAS6. Moreover, AXL expression was barely detectable in normal breast tissues, but was increased in breast tumor samples and was correlated with that of flotillin 1, particularly in the luminal and HER2 (also known as ERBB2)-positive breast cancer subtypes (Fig. S4A,B).

Flotillin upregulation promoting an increase in AXL levels did not occur at the transcriptional level (Fig. 3B). We assessed AXL stability by comparing AXL expression in MCF10AmCh and MCF10AF1F2 cells incubated with cycloheximide (CHX) to block protein synthesis. AXL decay was significantly slower in MCF10AF1F2 cells than in MCF10AmCh cells (Fig. 3C). This indicates that flotillin upregulation promotes AXL stabilization. We analyzed the contribution of AXL to EMT and cell migration induced by flotillin upregulation in MCF10A cells. AXL knockdown by siRNAs in MCF10AF1F2 cells decreased ZEB1 expression (Fig. 3D,E), reversed the E- to N-cadherin switch (Fig. 3D,F) and reduced the migration of the cells (Fig. 3G).

Altogether, these results showed that flotillin upregulation in non-tumoral mammary epithelial cells promotes AXL stabilization, leading to the increase of its phosphorylated form, as observed in many invasive cancer types. These results also revealed that AXL plays a central role in flotillin upregulation-induced EMT and cell migration in mammary epithelial cells.

AXL is a cargo of the UFIT pathway that is targeted to flotillin-positive LEs

Deregulated endocytosis and vesicular trafficking alter the fate of signaling receptors, affecting their expression level and downstream signaling (Dobrowolski and De Robertis, 2008; Gonnord et al., 2012; Schmid, 2017); hence, we asked whether AXL is an UFIT pathway cargo. We developed an optogenetic approach based on the CRY2-CIBN system (Nguyen et al., 2016) to force flotillin oligomerization by light illumination combined with total internal reflection fluorescence (TIRF) video microscopy (see Fig. 4A for the description of the experimental set up and Fig. S5A for the validation of the tools). Using MCF10A cells co-expressing flotillin 2-CIBN-mCherry, CRY2-mCitrin and AXL-Halo, upon light illumination to induce CRY2 oligomerization and binding to CIBN, we demonstrated the formation at the PM of domains that contained both flotillin 1 and 2 (Fig. 4B) and AXL-Halo (Fig. 4B and Fig. S5B,D, Movie 1). Using time-lapse imaging, we detected the co-endocytosis of flotillin 2-mCherry and AXL-GFP (characterized in Fig. S5C) from PM sites in MCF10AF1F2 cells where both proteins initially co-accumulated (Fig. 4C, Movie 2). In agreement, we showed that, in MCF10AmCh cells, AXL was mainly at the PM. Conversely, in MCF10AF1F2 cells, AXL was still detectable at the PM in flotillin-rich regions, but was enriched in flotillin-positive vesicles (Fig. 4D), which were positive for the LE marker CD63 (Fig. 4J). Similarly, in MDA-MB-231 mammary tumor cells, in which endogenous flotillins are overexpressed (Planchon et al., 2018), AXL and flotillins 1 and 2 colocalized at the PM and in intracellular vesicles (Fig. S5E,F) that were CD63 positive (Fig. 4K). AXL-GFP co-trafficked with flotillin 2-mCherry in living MCF10AF1F2 (Fig. S5G, Movie 3) and MDA-MB-231 cells (Fig. S5H, Movie 4). About 40% of the flotillin 2-mCherry-positive vesicles were positive for AXL-GFP, and half of AXL-GFP-containing vesicles were positive for flotillin 2-mCherry (Fig. S3C). Conversely, CD71, the expression of which remained unchanged upon flotillin upregulation (Fig. S3A), poorly colocalized with flotillin-positive endosomes (Fig. S3C). These findings show that flotillins and AXL are present in the same PM domains, from where they are co-endocytosed towards LEs where

Journal of Cell Science (2022) 135, jcs259178. doi:10.1242/jcs.259178

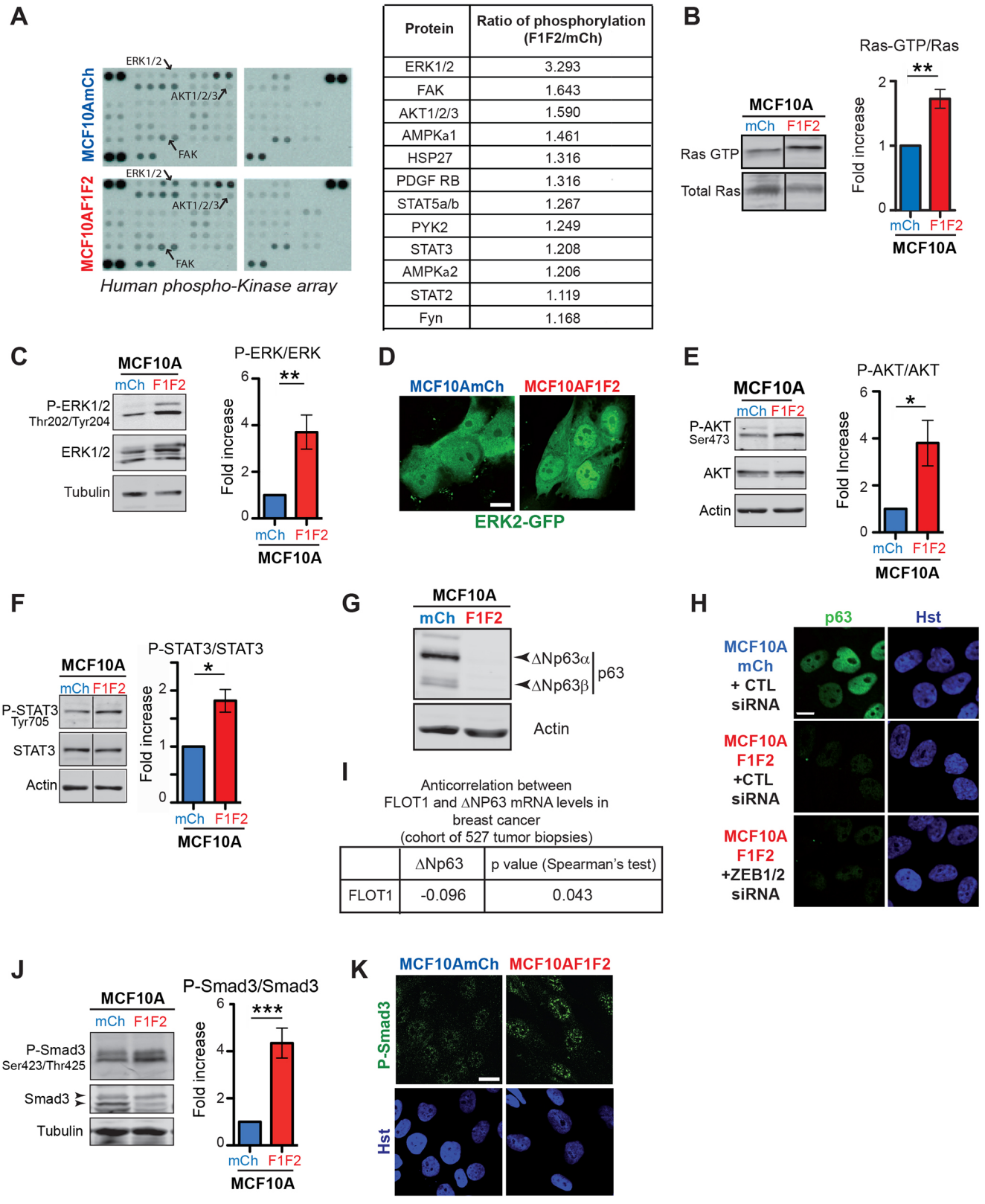

Protein	Ratio of phosphorylation (F1F2/mCh)
ERK1/2	3.293
FAK	1.643
AKT1/2/3	1.590
AMPKa1	1.461
HSP27	1.316
PDGF RB	1.316
STAT5a/b	1.267
PYK2	1.249
STAT3	1.208
AMPKa2	1.206
STAT2	1.119
Fyn	1.168

I

Anticorrelation between FLOT1 and ΔNP63 mRNA levels in breast cancer (cohort of 527 tumor biopsies)

	ΔNp63	p value (Spearman's test)
FLOT1	-0.096	0.043

Fig. 2. See next page for legend.

they co-accumulate. Similarly, in breast tumor samples, flotillin 1 and AXL accumulate in intracellular vesicles in malignant cells (Fig. S4C). This co-distribution of flotillins and AXL is in agreement with the detection of flotillin 1 and AXL complexes by co-immunoprecipitation experiments in MCF10AF1F2 cells (Fig. 4E).

To monitor the impact of flotillin upregulation on AXL endocytosis, we performed an AXL uptake assay using the D4

Journal of Cell Science

Journal of Cell Science (2022) 135, jcs259178. doi:10.1242/jcs.259178

Fig. 2. Flotillin upregulation promotes the activation of oncogenic signaling pathways. (A) Representative example of human phospho-kinase arrays incubated with MCF10AmCh and MCF10AF1F2 cell lysates. The table lists the 12 kinases and kinase substrates with the highest ratio of phosphorylation change between MCF10AF1F2 and MCF10AmCh cells. Values are the mean of two independent experiments. (B) Quantification of active GTP-bound Ras in cell lysates. The histogram shows Ras activity (mean±s.e.m. of five independent experiments) normalized to the amount of total protein. (C,E,F,J) Western blot analysis of ERK1 and ERK2 (C), AKT (E), STAT3 (F) and SMAD3 (G) phosphorylation status in cell lysates. The histograms show protein phosphorylation level normalized to the total amount of the considered protein in MCF10AF1F2 versus MCF10AmCh cells (mean±s.e.m. of at least four independent experiments). (D) ERK2-GFP distribution analyzed by confocal microscopy 36 h post-transfection. (G) Western blot analysis using an antibody against all p63 isoforms. (H) Confocal microscopy images in the indicated cells after staining with an antibody against all p63 isoforms and Hoechst (Hst). (I) Analysis of the correlation between *FLOT1* and *p63* mRNA levels in breast cancer biopsies from 527 patients (Planchon et al., 2018). (K) Confocal microscopy images of cells stained with an antibody against SMAD3 phosphorylated on S423/425 and Hoechst (Hst). In D, H and K, images are representative of three independent experiments. Scale bars: 10 µm. **P*<0.05, ***P*<0.01, ****P*<0.001 (Mann-Whitney test, two-tailed *P*-values).

antibody against the AXL extracellular domain coupled with immunocytochemical detection (Fig. S5I). Immediately after incubation with the D4 antibody, we detected cell-surface AXL signals in MCF10AmCh and MCF10AF1F2 cells (Fig. 4F). After 10 min of internalization, the AXL-D4 signal was more internalized in flotillin-positive endosomes in MCF10AF1F2 cells compared with MCF10AmCh cells (Fig. 4F). We obtained similar results by monitoring N-terminally Myc-tagged AXL surface expression with an anti-Myc antibody (Fig. S5J). Thus, AXL internalization occurs faster in cells in which flotillins are upregulated, which was confirmed using a cell surface biotinylation assay (Fig. 4G, upper panels). Reciprocally, to analyze the impact of flotillin downregulation on AXL internalization in MDA-MB-231 cells, we used the MDA-MB-231-shFlot2 cell line (Planchon et al., 2018). Flotillin downregulation slowed down AXL internalization (Fig. 4G, lower panels), and AXL accumulated at the PM in MDA-MB-231-shFlot2 cells (Fig. 4H,I). Conversely, CD71 internalization was not affected by flotillin upregulation (Fig. S3D), in agreement with its low presence in flotillin-positive vesicles (Fig. S3C). This indicates that flotillin upregulation does not affect the endocytosis and trafficking of all membrane receptors.

Flotillin-positive vesicles are LAMP1-, Rab7a- and CD63-positive LEs, previously characterized as non-degradative LEs on the basis of their very low staining for fluorescent cleaved DQ-BSA (Planchon et al., 2018). In agreement with AXL stabilization in flotillin-upregulated cells, we found AXL in flotillin-, CD63- and LAMP1-positive vesicles in MCF10AF1F2 cells [endogenous AXL (Fig. 4J, and Fig. S5K) and Myc-tagged AXL (Fig. S5L)] and in MDA-MB-231 cells (Fig. 4K). Similarly, the presence of AXL in LAMP1-positive vesicles in mammary tumor cells was recently demonstrated (Zajac et al., 2020). In flotillin-positive LEs, we also detected other signaling transmembrane receptors and oncogenic molecules that participate in tumorigenesis, such as EphA4, TGFβ (Fig. S6A-F) and K-Ras4B (Fig. S6G). Specifically, flotillin upregulation modified the distribution of K-Ras4B but not of any other Ras isoforms. K-Ras4B was localized at the PM in MCF10AmCh cells, and in flotillin-positive vesicles in MCF10AF1F2 cells (Fig. S6G). This correlated with the co-immunoprecipitation of K-Ras4B, but not of K-Ras4A, with flotillin 1 (Fig. S6H).

Altogether, these results showed that AXL is a cargo of the UFIT pathway. Flotillin upregulation accelerated AXL internalization and promoted AXL endocytosis toward flotillin-positive LEs.

Sphingosine kinase 2 is required for AXL stabilization through the UFIT pathway

To identify the molecular mechanisms linking AXL accelerated internalization and stabilization, and its sorting towards flotillin-positive LEs, we focused on sphingolipids, the metabolism of which is linked to endocytosis and flotillins. Indeed, flotillins bind to sphingosine, and sphingosine-1-phosphate (S1P) levels are reduced in cells from flotillin knockout mice (Riento et al., 2018). The bioactive lipid S1P is implicated in endocytosis and membrane remodeling (Kajimoto et al., 2013; Shen et al., 2014; Lima et al., 2017). S1P production, which is induced upon sphingosine phosphorylation by sphingosine kinase (SPHK) 1 or 2, has been linked to cancer progression (Pyne et al., 2018). SPHK1 and SPHK2 subcellular localization, and consequently S1P production compartmentalization, play an important role in their functions (Siow and Wattenberg, 2011). We hypothesized that flotillin-rich regions of membranes can concentrate sphingosine, where SPHKs could be recruited to locally generate S1P.

We examined sphingosine cell distribution after addition of fluorescent NBD-sphingosine in live cells. In MCF10AF1F2 cells, and also in MDA-MB-231 and Hs 578T breast cancer cells that express flotillin 2-mCherry, NBD-sphingosine was almost undetectable at the PM, but it accumulated strongly and rapidly in flotillin 2-mCherry-positive vesicles (Fig. 5A,B and Fig. S7A). Conversely, fluorescent Oregon Green-phosphatidylethanolamine poorly accumulated in flotillin 2-mCherry-positive vesicles (Fig. 5A).

Then, we investigated SPHK localization in MCF10AF1F2 and MDA-MB-231 cells expressing GFP-tagged SPHK1 or SPHK2 because no antibody is available for immunocytochemistry. We detected SPHK2-GFP in ∼70% of flotillin-positive vesicles (Fig. 5C-E, Movie 5), in contrast to SPHK1-GFP (Fig. 5D and Fig. S7B). In Hs 578T cells, SPHK2-GFP was also localized in flotillin-positive vesicle (Fig. S7E). SPHK2- and flotillin-positive vesicles also contained AXL (Fig. 5F, Movie 6), Rab7 (Fig. S7C) and CD63 (Fig. S7D). SPHK2 and flotillin 2 also colocalized at discrete sites of the PM, from which we could observe the fast co-endocytosis of both proteins (Fig. 5E, Movies 7 and 8). Flotillin upregulation increased SPHK2 recruitment to CD63-positive LEs (Fig. 5G), without modifying its protein expression level (Fig. S7F).

On the basis of these results and the finding that S1P level is reduced in cells derived from flotillin-KO mice (Riento et al., 2018), we asked whether flotillin upregulation increased S1P intracellular levels. Mass spectrometry quantification showed that S1P levels were 2.8-fold higher in MCF10AF1F2 than MCF10AmCh cells (Fig. 5H).

Owing to increased S1P levels in cells with upregulated flotillins and to SPHK2 enrichment in flotillin-positive membrane domains and flotillin-positive vesicles, we then asked whether S1P generation by SPHK2 was involved in AXL stabilization upon flotillin upregulation. Addition of the selective SPHK2 inhibitor (Riento et al., 2018) opaganib to cells expressing SPHK2-GFP led to its rapid dissociation from flotillin-positive endosomes that lasted for several hours (Fig. S7G, Movie 9). Incubation of MCF10AF1F2 or MDA-MB-231 cells with opaganib for only 4 h did not affect AXL expression level (Fig. 6A). However, in MCF10AF1F2 cells incubated with opaganib for 10 h, AXL levels were reduced to those observed in MCF10AmCh cells (Fig. 6A). AXL was similarly

Journal of Cell Science (2022) 135, jcs259178. doi:10.1242/jcs.259178

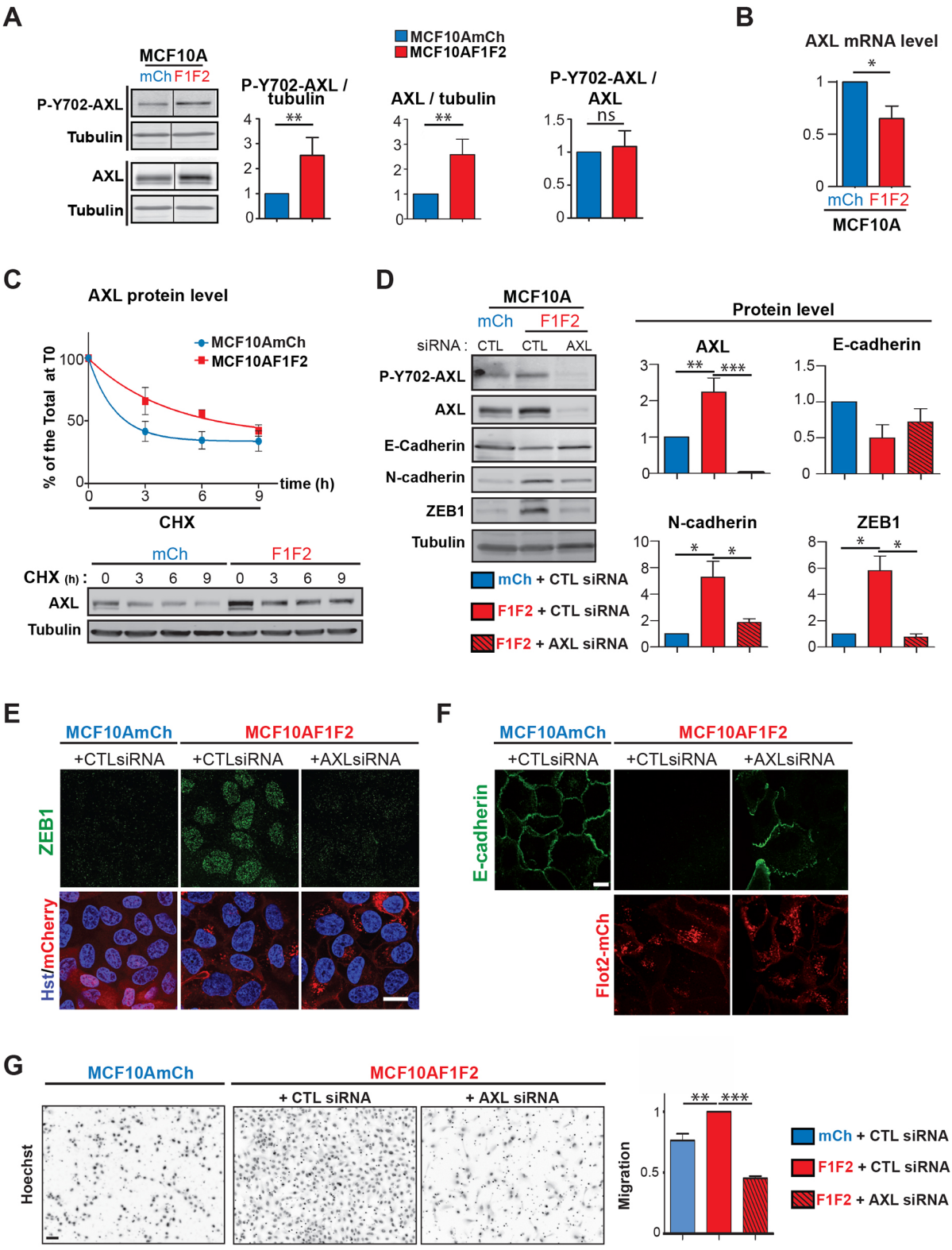

Fig. 3. See next page for legend.

decreased in MCF10F1F2 and MDA-MB-231 cells, where SPHK2 was efficiently knocked down by siRNA (Fig. 6B,C). Opaganib treatment also led to a decrease in AXL in MDA-MB-231shLuci and in Hs 578T cells (Fig. 6D and Fig. S7H) that express high flotillin levels. In MCF10AF1F2 and MDA-MB-231shLuci cells, SPHK2 inhibition decreased also ZEB1 levels (Fig. 6A-D), in agreement with our finding that its expression is AXL dependent (Fig. 3D,E). Of note, SPHK2 inhibition did not alter flotillin levels in MCF10AmCh and MCF10AF1F2 cells (Fig. 6A), or AXL levels in MCF10AmCh cells (Fig. 6A) and in MDA-MB-231-shFlot2 cells (Planchon et al., 2018) (Fig. 6D). This indicates that SPHK2 activity is required for maintaining high AXL levels specifically in

Fig. 3. AXL is stabilized upon flotillin upregulation and is involved in upregulated flotillin-induced EMT and cell migration. (A) Cell lysates were probed by western blotting with antibodies against AXL phospho-Y702, total AXL and tubulin. Results are expressed as fold increase compared with MCF10AmCh cells (data are mean±s.e.m. of six independent experiments). (B) RT-qPCR analysis of *AXL* expression. Results are expressed relative to the level in MCF10AmCh cells (data are mean±s.e.m. of four independent experiments). (C) Cells were incubated with cycloheximide (CHX, 100 µg/ml) and cell lysates collected at the indicated time points. AXL and tubulin levels were assessed by western blotting (representative western blots in lower panels). The graph shows the normalized AXL levels in each cell line during CHX incubation. Data are mean±s.e.m. of six to eight independent experiments depending on the time point, and are expressed as the percentage of AXL level at *t*=0. The exponential one phase decay curve was generated for each condition, the least squares fit method validated a significant difference (P=0.0033). (D) Cells were transfected with the indicated siRNAs and probed by western blotting. Data are mean±s.e.m. of four independent experiments, and are expressed as fold-increase versus MCF10AmCh. (E) ZEB1 nuclear localization (immunocytochemistry and co-staining with Hoechst) and (F) E-cadherin distribution (immunocytochemistry) in cells transfected with the indicated siRNAs. Scale bars: 10 µm. (G) Cells transfected with the indicated siRNAs were seeded in the top of Boyden chamber inserts in serum-free medium. Serum-containing medium, acting as chemoattractant, was placed in the bottom well. Representative inverted-microscopy images of Hoechst-stained nuclei of cells that migrated through the pores. The histogram (data are mean±s.e.m. of at least four independent experiments) shows the quantification of cell migration. Scale bar: 50 µm. Images in E,F are representative of at least four independent experiments. *P<0.05, **P<0.01, ***P<0.001 (Mann-Whitney test, two-tailed P-values).

the context of flotillin upregulation. Moreover, in agreement with the limited SPHK1-GFP localization in flotillin-positive vesicles (Fig. 5D and Fig. S7B), SPHK1 inhibition using PF543 had no effect on AXL levels in MCF10AF1F2 and MDA-MB-231 cells (Fig. S7I).

To confirm that SPHK2 was involved in AXL stabilization downstream of upregulated flotillins, we examined AXL levels in MCF10AF1F2 and MDA-MB-231shLuci cells incubated with CHX to inhibit protein synthesis. CHX considerably decreased AXL level in both cell lines, and the effect was stronger in cells co-incubated with opaganib (Fig. 6E). In agreement, in cells exposed to CHX for up to 9 h, AXL decay was more pronounced in cells in which SPHK2 was knocked down than in controls (Fig. 6F). Conversely, CD71, which poorly localized in flotillin-positive endosomes (Fig. S3C) and the endocytosis of which was not influenced by flotillin level and SPHK2 activity (Fig. S3A,D,E), remained stable upon incubation with CHX, even in cells in which SPHK2 was silenced (Fig. S3F). This demonstrated that SPHK2 activity was involved in AXL stabilization, but not in stimulating its synthesis.

We next investigated how SPHK2 contributed to AXL stabilization. As SPHK2 co-accumulated with flotillins at the PM before endocytosis (Fig. 5E, Movies 7, 8), we analyzed its participation in flotillin-mediated AXL endocytosis. We compared AXL internalization rate and cell surface level in cells incubated or not (control) with opaganib for only 4 h. This short incubation time, when AXL decrease is not yet detectable (Fig. 6A,D), allows a more straightforward analysis of AXL internalization and level at the cell surface. AXL internalization was significantly decreased when SPHK2 was inhibited in both MCF10AF1F2 and MDA-MB-231shLuci cells (Fig. 6G,H). In agreement, incubation with opaganib increased AXL expression at the cell surface in both cell lines (Fig. 6I,J). This indicates that SPHK2 participates in flotillin-mediated AXL endocytosis. In accordance with the finding that CD71 internalization is not influenced by flotillin level (Fig. S3D), we found that it was not altered by SPHK2 inhibition (Fig. S3E). This confirmed that CD71 is not endocytosed through the UFIT pathway. In agreement with the finding that AXL knockdown inhibited MCF10AF1F2 cell migration (Fig. 3G), SPHK2 inhibition or knockdown also reduced their migration (Fig. S7J), in addition to decreasing AXL level (Fig. 6A,B). In conclusion, our data demonstrate that the lipid kinase SPHK2, which colocalizes with flotillins at the PM and in LEs, possibly by locally generating S1P, is required to divert flotillin-mediated AXL endocytosis towards the UFIT pathway in order to promote its stabilization, thus favoring cell migration.

DISCUSSION

Here, we demonstrate that flotillin upregulation in non-tumoral mammary cell lines devoid of oncogenic mutations is sufficient to activate oncogenic signaling pathways that lead to EMT induction, a key step towards cancer cell invasion. Moreover, flotillin upregulation led to the stabilization of AXL through the UFIT pathway that promotes endocytosis of several cargos from the PM toward flotillin-positive LEs (Fig. 7). This requires the lipid kinase SPHK2, which demonstrates the role of sphingolipid metabolism on this UFIT pathway. Our findings demonstrate the unprecedented role of flotillin-induced endosomal trafficking on AXL upregulation, a major feature of several invasive tumors.

Flotillins are upregulated in many tumor types, and their upregulation is predictive of aggressive tumor behavior (reviewed by Gauthier-Rouvière et al., 2020). Flotillin co-upregulation is necessary and sufficient to promote breast, nasopharyngeal and rhabdomyosarcoma cancer cell invasion (Liu et al., 2015; Cao et al., 2016; Planchon et al., 2018). Their specific role in metastasis formation was demonstrated in flotillin 2 knockout mice (Berger et al., 2013). EMT is a crucial step in tumor initiation and cancer cell dissemination, but the contribution of flotillins to this process remained to be addressed (Zhao et al., 2015). Previous studies were performed in cancer cell lines with mutations in both signaling and structural genes that promote EMT induction and invasion. To determine the exact contribution of flotillin upregulation to this crucial process and the molecular mechanisms that are specifically deregulated, we co-upregulated flotillins 1 and 2 in immortalized non-tumoral mammary cell lines that physiologically display low flotillin expression levels. Flotillin upregulation was sufficient to promote EMT and activation of key signaling pathways involved in EMT induction. We identified AXL as a key upstream actor. However, other receptors implicated in mammary tumor development might also be co-deregulated, according to the results of our phospho-RTK arrays (Fig. S2H,I) and the presence in flotillin positive-endosomes of EphA4 and TGFβ receptors (Fig. S6) (Pardali and Moustakas, 2007; Gjerdrum et al., 2010; Gregory et al., 2011; Hachim et al., 2017). Following flotillin upregulation, Ras and PI3K and the downstream signaling pathways, which are frequently activated in several cancers (Bailey et al., 2018), were induced in MCF10A cells that do not harbor mutations in these cancer driver genes (Bessette et al., 2015). Moreover, flotillin upregulation mimics oncogenic Ras activation that in MCF10A mammary cells has been correlated with ΔNp63α downregulation, PI3-K/AKT activation and ZEB1- and ZEB2-mediated EMT (Yoh et al., 2016). These findings show that flotillin upregulation mimics the effects of cancer driver gene mutations, acts as an EMT driver, and promotes tumor cell invasion (Planchon et al., 2018).

We demonstrate that flotillin upregulation deregulates the trafficking of PM receptors, and identify them as new cargos of the UFIT pathway. This endocytic pathway emerges in the context

Journal of Cell Science (2022) 135, jcs259178. doi:10.1242/jcs.259178

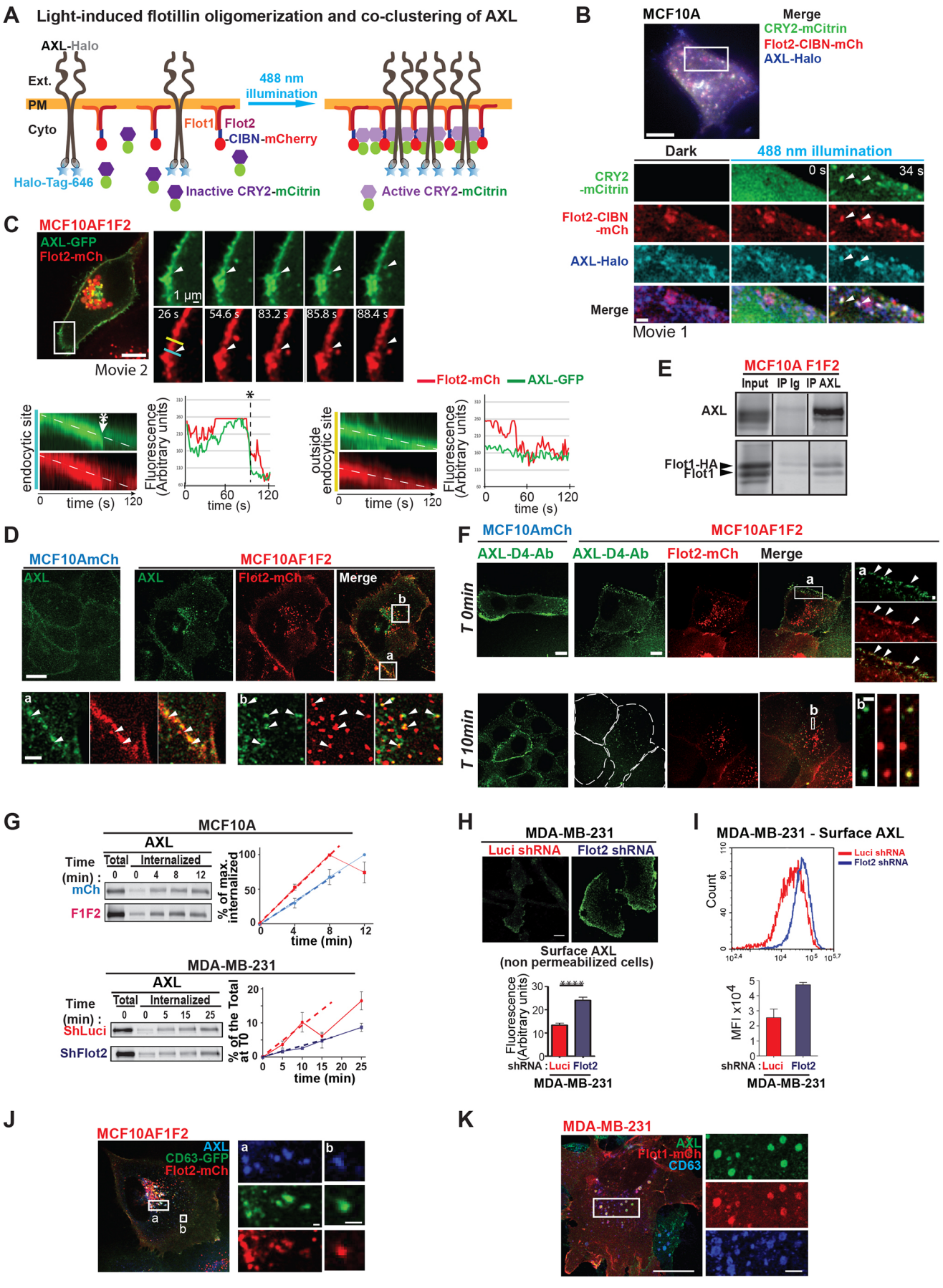

Fig. 4. See next page for legend.

Journal of Cell Science (2022) 135, jcs259178. doi:10.1242/jcs.259178

Fig. 4. AXL is a cargo of the UFIT pathway. (A) Schematic representation of the optogenetic system used to induce flotillin oligomerization. Flotillin 2-CIBN-mCherry, CRY2-mCitrin and AXL-Halo were co-expressed in MCF10A cells. Light illumination (488 nm) induces CRY2 oligomerization and its binding to CIBN, allowing the oligomerization of flotillin 2-CIBN-mCherry with flotillin 1. AXL-Halo is trapped in the light-induced flotillin microdomains. (B) Still images from a TIRF-microscopy movie of a MCF10A cell co-expressing CRY2-mCitrin, flotillin 2-CIBN-mCherry and AXL-Halo. Representative image of a cell 15 s after starting the 488 nm illumination to perform CRY2 binding to flotillin 2-CIBN-mCh and subsequent oligomerization (see also Fig. S5 for the validation of the tools). Fig. S5D shows the same cell with separate images for CRY2-mCitrin, flotillin 2-mCherry and AXL-Halo signals at different times before and after illumination. Magnified images from the boxed area taken before (dark) and after 488 nm illumination. Arrowheads indicate CRY2-mCitrin and flotillin 2-CIBN-mCherry clusters accumulating AXL-Halo (Movie 1). Images are representative of five independent experiments. (C) Still images of a time-lapse series of one MCF10AF1F2 cell expressing AXL-GFP to show flotillin 2/AXL colocalization at the PM and their co-endocytosis at PM sites (arrowheads). Kymographs show the temporal variation of the GFP and mCherry signals along two line-scans (blue at the endocytic site; yellow outside the endocytic site). Graphs show the intensity variation of both signals along the dotted white lines on the kymographs. The left kymograph shows AXL-GFP and flotillin 2-mCherry co-accumulation at the PM followed by a concomitant drop of both signals (at around 83 s, indicated by the asterisk). The right kymograph shows that both AXL-GFP and flotillin 2-mCherry signals remained stable at the PM outside the endocytic site (Movie 2). (D) Endogenous AXL distribution in MCF10AmCh and MCF10AF1F2 cells analyzed by confocal microscopy after immunofluorescence staining. Higher magnification images of the two boxed regions show AXL colocalization with flotillin 2-mCherry at the PM (a) and in intracellular vesicles (b; white arrowheads). (E) AXL was immunoprecipitated from MCF10AF1F2 cell lysates, and flotillin 1 co-immunoprecipitation was assessed by immunoblotting. Ig, non-relevant immunoglobulins used for control immunoprecipitation. Results are representative of three independent experiments. (F) Cells were incubated with the anti-AXL D4 antibody at 4°C and then at 37°C for 10 min to allow AXL internalization. AXL and flotillin 2-mCherry signals were analyzed by immunocytochemistry. Arrowheads indicate AXL/flotillin 2 colocalization. Images are representative of at least five independent experiments. Scale bars: 10 µm in the main images; 1 µm in the magnified images. Fig. S5I shows results from an AXL immunofluorescence staining of the same MCF10F1F2 cell 10 min after internalization. It indicates that the vesicles labeled by the D4 antibody are indeed positive for AXL. (G) AXL internalization kinetics in the indicated cell lines. Surface proteins were labeled with biotin at 4°C, and cells were incubated at 37°C for the indicated times to allow endocytosis. AXL presence in the internalized biotinylated fraction was probed by immunoblotting and quantified as the percentage of the maximum level of internalized protein (reached at 12 and 8 min in MCF10AmCh and MCF10AF1F2 cells, respectively). After simple linear regression, the AXL internalization rates (dashed lines) were 8.48±1.28 and 12.43±0.48%/min in MCF10AmCh and MCF10AF1F2 cells, respectively. Comparison of the slopes using GraphPad Prism revealed a significant 1.45-fold increase (P=0.0088) upon flotillin upregulation. In MDA-MB-231shLuci and MDA-MB-231shFlot2, results are expressed as the percentage of the maximum level of surface-labeled AXL at t=0. Similarly, after simple linear regression, comparison of the AXL internalization rates from 0 until 10 min (dashed lines) showed a significant 3.66-fold decrease (P=0.0009) upon flotillin downregulation. Data are mean±s.e.m. of four independent experiments. (H) In fixed non-permeabilized cells, AXL expression was analyzed using the D4 antibody against AXL extracellular domain and an Alexa488-conjugated anti-human secondary antibody. Images were acquired in the same illumination conditions for MDA-MB-231-shLuci cells (control) and MDA-MB-231-shFlot2cells (knocked down for flotillins). The mean fluorescence intensity was quantified in each area delimited by the cell outline (n=53 MDA-MB-231-shLuci cells and n=41 MDA-MB-231-shFlot2cells). Values are expressed in arbitrary units (mean±s.e.m.). (I) Fixed, non-permeabilized cells were labeled with the D9 anti-AXL antibody and a Alexa488-conjugated secondary antibody, and analyzed by FACS. Results are expressed as the mean fluorescence intensity (MFI) from three independent experiments. (J,K) Immunofluorescence analysis by confocal microscopy of endogenous AXL expression in MCF10AF1F2 cells that express CD63-GFP (J) and of endogenous AXL and CD63 in MDA-MB-231 cells that express flotillin 1-mCherry (K). Higher magnification images of the boxed regions show AXL signal in flotillin 2-mCherry- (J), flotillin 1-mCherry- (K) and CD63-positive vesicles (J,K). Images are representative of three independent experiments. Scale bars: 10 µm for the main images; 2 µm for the magnified images. ****P<0.0001 (Mann-Whitney test, two-tailed P-values).

of flotillin upregulation, and the proteins located in the flotillin-containing PM microdomains are endocytosed and delivered to flotillin-positive non-degradative LEs (Planchon et al., 2018). Besides their weak degradative activity (Planchon et al., 2018), these vesicles have characteristics of signaling endosomes because they contain activated RTKs (Fig. 4 and Fig. S6), and also the cancer driver K-Ras4B, which is associated with increased Ras activity upon flotillin upregulation (Fig. S6G and Fig. 2B). Interestingly, K-Ras and activated ERK1/2 are recruited to Rab7-positive endosomes (Lu et al., 2009). Endosomes act as signaling platforms to facilitate the multiplexing of signaling molecules that, in turn, affect the endosomal system by modifying the number, size and position of endosomes, and ultimately the trafficking of signaling molecules (Murphy et al., 2009; Villaseñor et al., 2016). The UFIT pathway is a key player in connecting deregulation of endocytosis and signaling in cancer cells.

This is illustrated here for AXL, a cargo of the UFIT pathway that is crucial to sustain EMT-promoting signaling upon flotillin upregulation. AXL is expressed in solid cancers, particularly breast carcinoma, where its level is associated with high risk of metastases and poor prognosis (Gjerdrum et al., 2010; Asiedu et al., 2014). AXL expression is correlated with the acquisition of a mesenchymal phenotype, invasive properties and treatment resistance. AXL is an attractive therapeutic target, and several AXL inhibitors are currently in preclinical and clinical development (Leconet et al., 2014, 2017; Gay et al., 2017). Although AXL overexpression in tumors is attributed to post-transcriptional regulation, the underlying mechanisms are unknown. When overexpressed, AXL activation is ligand independent and is the result of its oligomerization and/or association with other RTKs (Goyette et al., 2018). Using an optogenetic system to force flotillin oligomerization, we demonstrated the formation of flotillin/AXL clusters at the PM that are co-endocytosed. The UFIT pathway allows AXL delivery to flotillin-positive endosomes and AXL stabilization. Thus, flotillin upregulation emerges as a new control mechanism in the ligand-independent regulation of AXL post-transcriptional regulation. Previous studies identified ligand-independent AXL stabilization at the cell surface through its association with the HER2 receptor (Goyette et al., 2018), ligand-dependent AXL sequestration in cholesterol-enriched PM domains and internalization (Paolino et al., 2014; Antony et al., 2018). To our knowledge, this is the first report to describe AXL stabilization following its endocytosis. This flotillin/AXL link is also observed in invasive breast tumor cells. Indeed, AXL is very weakly expressed in non-tumoral breast lesions, whereas its expression is broadly detected in all malignant breast tumor subtypes (Goyette et al., 2018). AXL expression appears to be correlated with that of flotillin 1, especially in the luminal and HER2-positive subtypes (Fig. S4).

Our discoveries open a new interesting perspective for cancer therapy. Inhibition of flotillin functions might affect the efficacy of anti-AXL (which had promising results in preclinical models of pancreatic and breast tumors; Ye et al., 2010; Leconet et al., 2014, 2017) and anti-RTK antibodies by increasing the membrane receptor availability at the cell surface, particularly in flotillin-positive tumors. Endocytosis is dysregulated in human tumors. Its inhibition increases the availability of therapeutic monoclonal antibody targets and promotes antibody-dependent cell cytotoxicity (Joseph et al., 2019; Chew et al., 2020).

Journal of Cell Science (2022) 135, jcs259178. doi:10.1242/jcs.259178

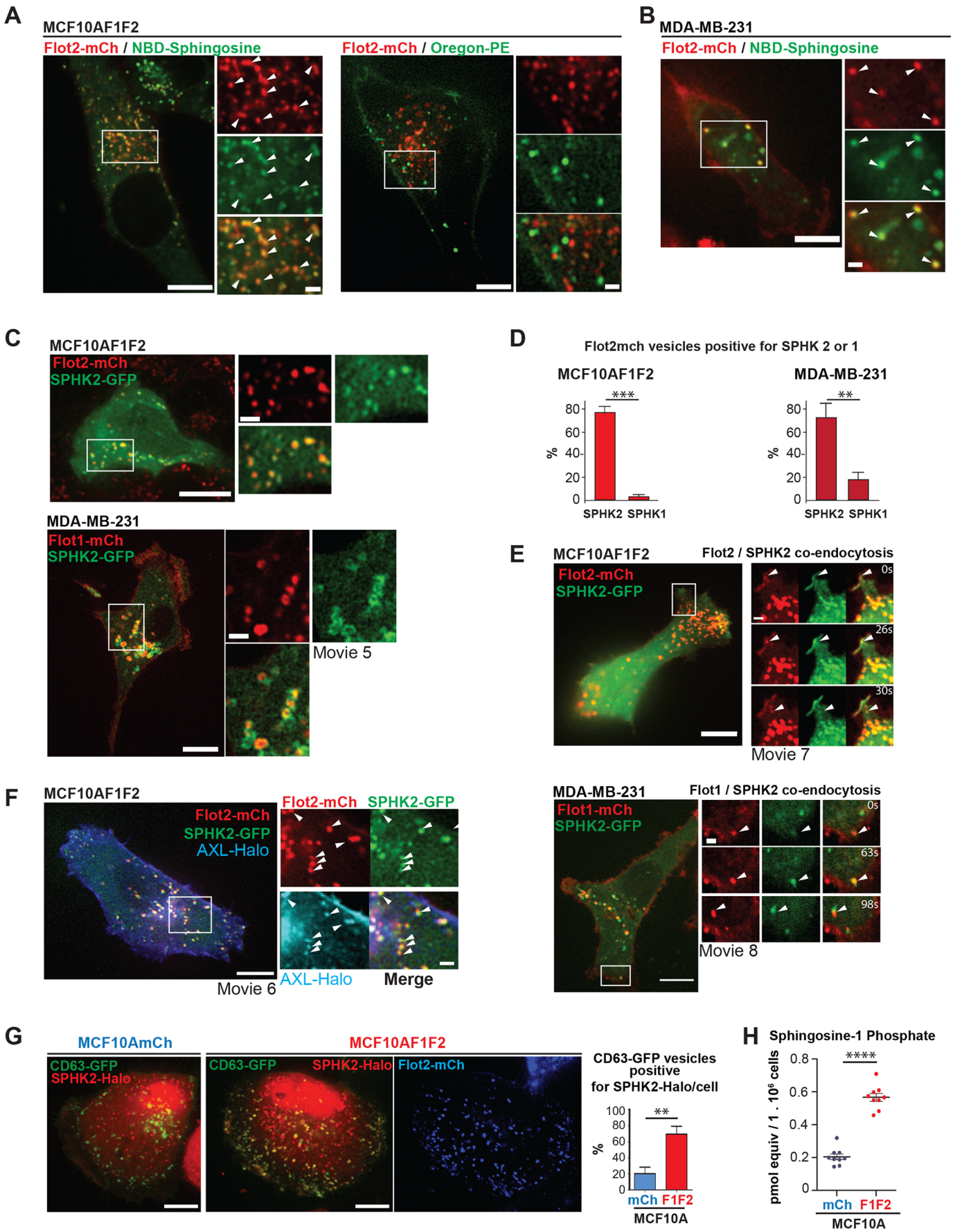

Fig. 5. See next page for legend.

Journal of Cell Science (2022) 135, jcs259178. doi:10.1242/jcs.259178

Fig. 5. SPHK2 is localized at flotillin-positive endocytic sites and at flotillin-positive LEs where AXL is present. (A,B) Live MCF10AF1F2 cells (A) and MDA-MB-231 cells (B) expressing flotillin 2-mCherry were incubated with NBD-sphingosine (A,B) or Oregon-Green-phosphatidylethanolamine (PE) (A) for 5 min. Images were acquired by spinning disk confocal microscopy. Still images acquired at 5 min and 25 min after addition of the fluorescent lipid are shown. White arrowheads indicate flotillin 2-mCherry-positive vesicles with NBD-sphingosine. (C) MCF10AF1F2 cells expressing SPHK2-GFP (top) and MDA-MB-231 cells co-expressing flotillin 1-mCherry or flotillin 2-mCherry and SPHK2-GFP (bottom) were imaged by spinning disk confocal microscopy (Movie 5). (D) Histograms show the quantification of flotillin 2-mCherry-positive vesicles where SPHK2-GFP or SPHK1-GFP was detected (see Fig. S7C,D). Data are mean±s.e.m. (n=300 vesicles in 10 MCF10AF1F2 cells; n=100 vesicles in 10 MDA-MB-231 cells co-expressing flotillin 2-mCherry and SPHK2 or SPHK1-GFP). (E) Still images from spinning disk confocal microscopy showing the fast co-endocytosis of flotillin 2-mCherry and SPHK2-GFP following their co-accumulation at the PM (indicated by the arrowheads) in MCF10AF1F2 cells (upper panels, Movie 7) and MDA-MB-231 cells (lower panels, Movie 8). (F) Still image from spinning disk confocal microscopy of live MCF10AF1F2 cells co-expressing SPHK2-GFP and AXL-Halo. Arrowheads indicate flotillin-positive vesicles containing SPHK2-GFP and AXL-Halo (Movie 6). The image is representative of several cells observed in three independent experiments. (G) MCF10AmCh and MCF10A F1F2 cells were co-transfected with CD63-GFP and SPHK2-Halo labeled with Halo-Tag-Janelia Fluor 646. Representative images acquired by spinning disk confocal microscopy of live cells. To better visualize the CD63-GFP and SPHK2-Halo colocalization, the SPHK2-Halo and flotillin 2-mCherry signals were pseudo-colored in red and blue, respectively. The presence of SPHK2-Halo in CD63-GFP-positive vesicles was quantified (n=372 vesicles in 10 MCF10AmCh cells; n=455 vesicles in 10 MCF10AF1F2 cells) and expressed as the percentage per cell of CD63-GFP-labeled vesicles positive for SPHK2-Halo. (H) Sphingosine-1-phosphate level was measured by quantitative mass spectrometry in three independent experiments (three independent MCF10AmCh and MCF10AF1F2 cell samples per experiment). The graph (pmol equiv/1.10^6 cells) shows the level in each sample. Data are mean±s.e.m. Scale bars: 10 µm in the main images; 2 µm in the magnified images. **P<0.01, ***P<0.001, ****P<0.0001 (Mann-Whitney test, two-tailed P-values).

Flotillin upregulation-induced AXL stabilization requires the activity of SPHK2, a lipid enzyme that maintains the cellular sphingolipid homeostasis and is a target for cancer therapies (Neubauer et al., 2016; Britten et al., 2017). SPHK2 colocalizes with flotillin-positive domains at the PM and is enriched in flotillin-positive endosomes, in agreement with previous findings showing SPHK2 localization in multivesicular endosomes in K562 leukemia cells (Mohamed et al., 2017). Flotillin binding to sphingosine and ectopic flotillin overexpression allow the formation of sphingosine domains that could favor SPHK2 recruitment (Riento et al., 2018). We found that SPHK2 inhibition or knock-down in cells with upregulated flotillins reduced AXL endocytosis (Fig. 6E,F) and AXL expression levels (Fig. 6A-D), and decreased cell invasion (Fig. S7J). Accordingly, SPHK2 inhibition did not affect AXL level in control MCF10A and in MDA-MB-231 invasive breast cells where flotillins were knocked down. In these cells, AXL accumulated at the PM, suggesting that the UFIT pathway targets AXL to flotillin-positive endosomes to escape degradation. AXL can be degraded at the PM or in the cytoplasm, through several mechanisms involving metalloproteases or gamma secretases, or the proteasome and the autophagic pathway (Krishnamoorthy et al., 2013; Bae et al., 2015; Rao et al., 2020). It remains to be determined from which degradation mechanism(s) the UFIT pathway protects AXL.

SPHK catalyzes S1P production from sphingosine and there is a strong causal association between overactive SPHK, S1P generation and cancer (Hatoum et al., 2017). SPHK2 is involved in MDA-MB-453 cell migration toward EGF (Hait et al., 2005), and SPHK2 upregulation promotes oncogenesis. Moreover, results from a phase 1 clinical trial support the use of SPHK2 inhibitors in cancer (Neubauer et al., 2016; Britten et al., 2017). Showing that SPHK2 inhibition affects AXL might help to understand the anti-tumoral function of these inhibitors and the role of SPHK2 during tumor development, which is unknown. The UFIT pathway does not influence SPHK2 expression level (Fig. S7E), but affects its recruitment to cell membranes, at flotillin-rich endocytic sites (Fig. 5D), and to flotillin-positive endosomes (Fig. 5E). In agreement, modifications of SPHK2 localization are linked to tumorigenesis (Siow and Wattenberg, 2011; Neubauer et al., 2019). Additional studies are required to understand how sphingolipid modifications participate in endocytic events at the PM and how they influence endosome fusion, motion and/or function.

In conclusion, this study adds new evidences for a crucial gain-of-function role of upregulated flotillins during EMT. We found that the UFIT pathway, by perturbing sphingolipid metabolism, allows the endocytosis of several PM receptors, particularly AXL, a major RTK during oncogenesis. AXL targeting to flotillin-positive LEs promotes its stabilization and signaling during EMT.

MATERIALS AND METHODS

Cell lines

All cell lines were authenticated, tested for contamination and cultured in a 37°C incubator with 5% CO_2. The MCF10A mammary epithelial cell line (American Type Culture Collection, ATCC CRL-10317) and the derived MCF10AmCh and MCF10AF1F2 cell lines were grown in DMEM/HAM F-12 medium supplemented with 5% horse serum (Gibco, Thermo), 10 µg/ml insulin, 20 ng/ml EGF, 0.5 µg/ml hydrocortisone and 100 ng/ml cholera toxin. The NMuMG mouse mammary epithelial cell line (ATCC CRL-1636) and the derived NMuMGmCh and NMuMG-F1F2 cell lines were grown in DMEM supplemented with 10% fetal bovine serum (FBS) (S1810-100; Biowest), 100 units/ml penicillin, 100 µg/ml streptomycin and 10 µg/ml insulin (I9278; Sigma-Aldrich). The human breast adenocarcinoma cell line MDA-MB-231 (ATCC HTB-26) and the MDA-MB-231shLuci- and MDA-MB-231-shFlot2-derived cell lines (described by Planchon et al., 2018), and the Hs 578T cell line were grown in DMEM with 10% FBS (Biowest, Eurobio). Retrovirus production in Phoenix cells (Garry Nolan, Center for Clinical Sciences Research, Stanford University, USA), infection and selection were performed as described previously (Fortier et al., 2008). Cells were grown continuously in 1 µg/ml puromycin and 200 µg/ml hygromycin.

The MCF10AF1F2 and NMuMGF1F2 cell lines that stably overexpress flotillin 1 and 2 were generated by double retroviral infection of two vectors encoding the chimeric proteins flotillin 2-mCherry and flotillin 1-HA (described by Planchon et al., 2018), followed by selection for resistance against puromycin and hygromycin. Cells were then sorted by flow cytometry according to the mCherry fluorescence signal.

Plasmids and transfections

peGFP-N1-AXL was generated by subcloning the human AXL sequence (NM_021913.4) amplified by PCR using the primers 5′-AAGCTTAT-GGCGTGGCGGTGCCCCAGG-3′ and 5′-GAATTCCGGCACCATCC-TCCTGCCCTG 3′ between the HindIII and EcoRI sites in peGFP-N1. pHalo-N1-AXL was obtained by replacing GFP by the Halo-sequence in peGFP-N1-AXL between HindIII and EcoRI. To generate the pBabe-Flot2-CIBN-mCherry construct, the sequence encoding the CIBN domain was amplified by PCR using the primers 5′-GAATTCTAATGAATGGAGC-TATAGGAGG-3′ and 5′-CGGATTATATTCATGTACCGGTCACACA-3′, and inserted, using the EcoRI and AgeI sites, between flotillin 2 and mCherry in the pBabe-Flot2-mCherry plasmid (Planchon et al., 2018). The peGFP-ERK2 construct was a gift from Dr H. Farhan (University of Oslo, Norway). The CD63-GFP plasmid was a gift from Dr A. Weaver (Vanderbilt University, Nashville, TN, USA) (Sung et al., 2015). The Rab7a-GFP plasmid has been described previously (Planchon et al., 2018).

Journal of Cell Science (2022) 135, jcs259178. doi:10.1242/jcs.259178

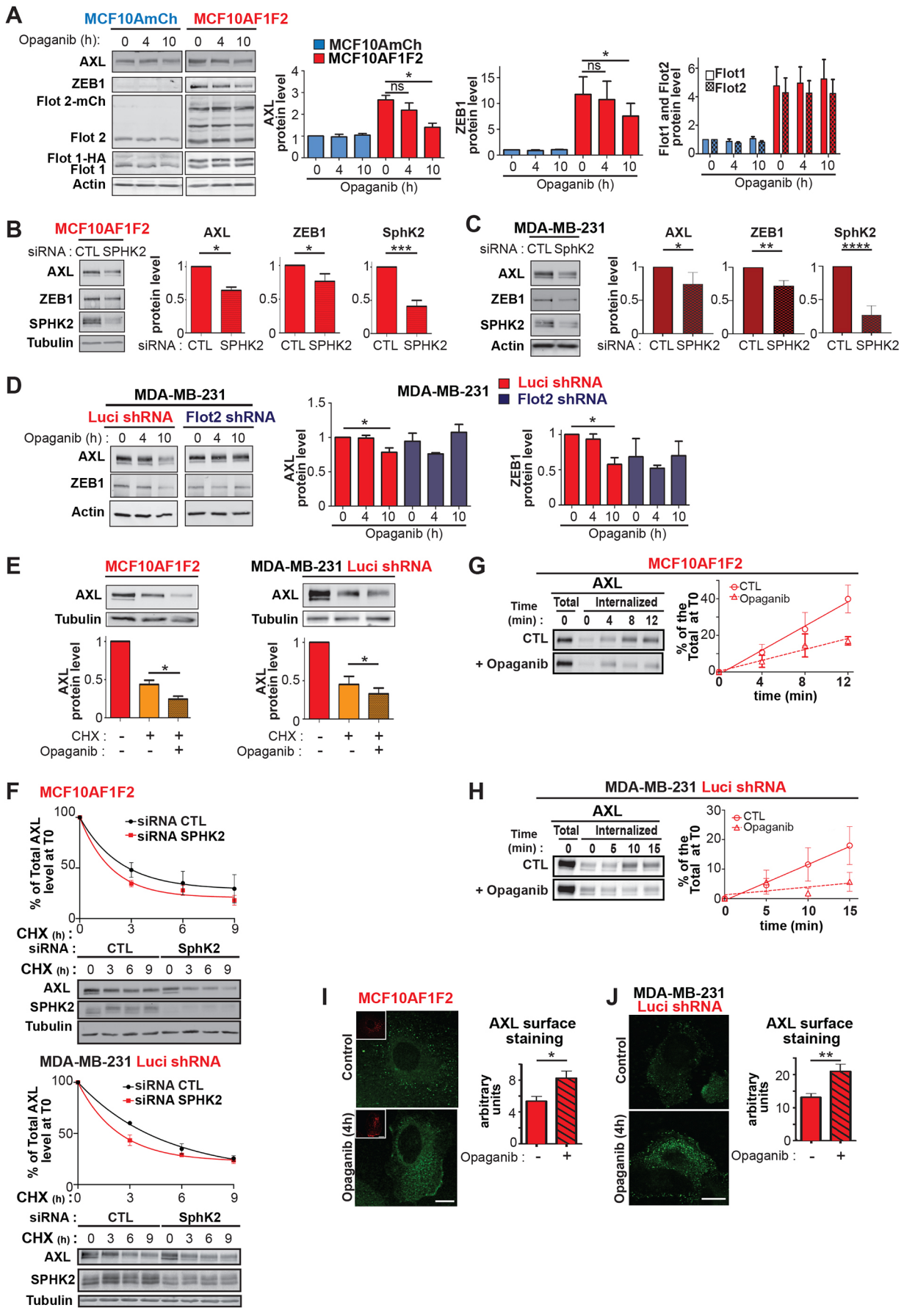

Fig. 6. See next page for legend.

Journal of Cell Science

Journal of Cell Science (2022) 135, jcs259178. doi:10.1242/jcs.259178

Fig. 6. Sphingosine kinase 2 controls AXL endocytosis and its stabilization. (A) Cells were incubated with opaganib (50 µM). AXL, ZEB1, and flotillin 1 and 2 were analyzed by western blotting in cell lysates. The protein level normalized to the actin signal is expressed as the fold increase versus control (MCF10AmCh cells) (data are mean±s.e.m., four independent experiments). (B,C) MCF10AF1F2 (B) and MDA-MB-231 (C) cells were transfected with the indicated siRNAs. siRNA efficacy was tested by western blotting with anti-SPHK2, -AXL, -ZEB1 and -tubulin/actin antibodies. Histograms show the level of each protein (data are mean±s.e.m. of four independent experiments) normalized to the tubulin/actin signal and expressed as fold increase compared with CTL. (D) MDA-MB-231shLuci (control) and MDA-MB-231shFlot2 cells were incubated with opaganib (50 µM). AXL, ZEB1 and actin were analyzed by western blotting in cell lysates. The histograms show the level of each protein normalized to the actin signal and expressed as fold increase compared with control (mean±s.e.m. of five independent experiments). (E) MCF10AF1F2 and MDA-MB-231shLuci cells were incubated with or without opaganib for 10 h. When indicated, cycloheximide (CHX) was added 4 h after the beginning of opaganib incubation. AXL was analyzed by western blotting in whole-cell lysates. The histograms show AXL level (data are mean±s.e.m. of four independent experiments) normalized to the tubulin signal, and expressed as fold increase compared with control (no treatment). (F) MCF10AF1F2 and MDA-MB-231shLuci cells were transfected with the indicated siRNAs for 72 h and incubated with cycloheximide (CHX, 100 µg/ml). AXL levels were assessed by western blotting in cell lysates. The exponential one-phase decay curves show AXL level at the different time points (as a percentage of the total level at *t*=0). Data are mean±s.e.m. for four (MCF10AF1F2 cells) and five (MDA-MB-231 cells) independent experiments. The least squares fit method validated the difference in AXL decay (P=0.044 for MCF10AF1F2 cells and P=0.0025 for MDA-MB-231 cells). (G,H) AXL internalization kinetics in MCF10AF1F2 (G) and in MDA-MB-231shLuci cells (H) pre-incubated or not (CTL) with opaganib (50 µM, 4 h). Surface proteins were labeled with biotin at 4°C, and cells were incubated at 37°C to allow endocytosis. AXL presence in the internalized biotinylated fraction was probed by western blotting. Results are expressed as the percentage of the maximum level of surface labeled AXL at *t*=0 and are the mean±s.e.m. of four independent experiments. After simple linear regression, in MCF10AF1F2 cells, the AXL internalization rates were 3.30±0.66 and 1.49±0.39%/min in the CTL and opaganib conditions, respectively. Comparison of the slopes with GraphPad Prism revealed a significant 2.2-fold decrease (P=0.0025) in opaganib-treated cells. In MDA-MB-231 shLuci cells, the internalization rates were 1.22±0.37 and 0.26±0.24%/min in the CTL and opaganib conditions, respectively, with a 4.69-fold decrease (P=0.0399) in opaganib-treated cells. (I,J) Fixed non-permeabilized cells were stained for AXL using the anti-AXL D4 antibody. Images of control- and opaganib-treated cells (50 µM, 4 h) were acquired in the same conditions. Representative images are shown (in MCF10AF1F2 cells, the insets show flotillin 2-mCherry signal). The mean fluorescence intensity was quantified in the area defined by the outline of each individual cell. Results are expressed as arbitrary units: mean±s.e.m. of 23 (MCF10AF1F2) and 22 (MDA-MB-231shLuci) measurements. Scale bars: 10 µm for the main images and 2 µm in the insets. *P<0.05, **P<0.01, ***P<0.001, ****P<0.0001 (Mann-Whitney test, two-tailed P-values).

The pCMV3-N-Myc human AXL (HG10279-NM) plasmid was purchased from Sino Biological. The peGFP-C1-KRas4A, peGFP-C3-KRas4B, peGFP-C3-HRas and peGFP-C3-NRas plasmids were gifts from Dr M. Philips (NYU Cancer Institute, New York, USA). The phCMV3-Flot1-HA plasmid was a gift from Dr V. Niggli (University of Bern, Switzerland) and pmCherry-N1-Flot2 has been previously described (Planchon et al., 2018). The plasmids encoding the different TAp63 α,β,γ and ΔNp63 α,β,γ isoforms were gifts from Dr C. Caron de Fromentel (INSERM UMR590, Lyon, France) (Petitjean et al., 2008), the PCS2+chickenEphA4-GFP plasmid was a gift from Prof F. Fagotto (CRBM, Montpellier, France) (Rohani et al., 2014). The TGFβRI-GFP and TGFβRII-Flag constructs were gifts from Dr R. Derynck (UCSF, San Francisco, CA, USA) (Budi et al., 2015). The SPHK1-GFP and SPHK2-GFP constructs were gifts from Prof. P. de Camilli (Yale School of Medicine, New Haven, CT, USA) (Shen et al., 2014). The SPHK2-Halo plasmid was obtained by replacing GFP with the Halo-sequence between EcoRI and NotI. The CRY2-mCitrin plasmid was a gift from Prof. W. Do Heo (KAIST, Dajeon, South Korea), previously described by Nguyen et al. (2016). The TfR(CD71)-GFP vector was purchased from Addgene (#45060). Cells were transfected with the indicated constructs using the JetPEI or JetPrime Transfection Reagents (Polyplus Transfection).

Antibodies and reagents

Mouse antibodies used were against: actin (1:5000, A5441, Sigma), flotillin 1 (1:1000, 610820, BD Biosciences), flotillin 2 (1:100, 610383, BD Biosciences), E-cadherin (used for MCF10A cells, 1:1000, 13-1700, Life Technologies), E-cadherin (used for NMuMG cells, 1:500 immunofluorescence, 1:2000 western blot, 610181, BD Biosciences), N-cadherin (1:200 immunofluorescence, 1:2000 western blot, 61920, BD Biosciences), LAMP1 (used for MCF10A cells, 1:1000, 555798, BD Biosciences), CD63 (1:300, 857.770.000, Diaclone), SMAD3 (1:500, MA5-15663, ThermoFisher), vimentin (1:100, V6630, Sigma), α-tubulin (1:200, Hybridoma Mab356), phosphorylated ERK1/2 at T202/Y204 [1:1000, 9106, Cell Signaling Technology (CST)], AKT (1:1000, 2920, CST), pan-Ras (1:500, OP40, Millipore), phosphorylated Y (1:50, Hybridoma G10) and STAT3 (1:1000, 9139, CST). Rabbit antibodies were against flotillin 1 (1:50, F1180, Sigma), flotillin 2 (1:100, 3436, CST), AXL (1:1000, 8661, CST), phosphorylated AXL at Y702 (1:250, D12B2, CST), ERK1/2 (1:1000, 9102, CST), phosphorylated AKT at S473 (1:1000, 4060, CST), ZEB1 (1:200, sc-25388, Santa Cruz), ZO-1 (1:200, 61-7300, Invitrogen), phosphorylated SMAD3 at S423/425 (1:2000, ab52903, Abcam), p63 (1:2000, ab124762, Abcam), phosphorylated EphA2,3,4 at Y588/596 (1:200, ab62256, Abcam), EphA4 (1:200, a gift from Dr Greenberg, Harvard University, Boston, MA, USA) (Rohani et al., 2014), phosphorylated STAT3 at Y705 (1:1000, 9131S, CST), p65-NFκB (1:1000, sc372, Santa Cruz), β-catenin (1:2000, C2206, Sigma, 2206), HA-tag (1:250, 71-5500, Invitrogen), Flag-tag (1:1000, F7425, Sigma), Myc-tag (1:100, 06549, Millipore) and SPHK2 (1:1000, 32346, CST). The humanized anti-AXL antibody D4 (https://patents.google.com/patent/EP3229836A1/en?oq=EP3229836A1) and the mouse anti-AXL antibody D9 (Leconet et al., 2014) were gifts from Dr B. Robert (ICRM, Montpellier, France). Alexa-488-, -546- and -633-conjugated secondary antibodies were from Thermo Scientific (Alexa-488-anti-mouse antibody, A-11017, 1:2000; Alexa-546-anti-mouse antibody, A-11018, 1:2000; Alexa-633 anti-mouse antibody, A21050, 1:1000; Alexa-488-anti-rabbit antibody A-11034, 1:2000; Alexa-546-anti-rabbit antibody, A-11035 dilution, 1:2000; Alexa-633 anti-rabbit antibody, A21070, 1:1000). Alexa-Fluor-488-phalloidin was from Invitrogen and Hoechst 33342 (0.1 mg/ml; #B2261) was from Sigma-Aldrich. Lipopolysaccharide (LPS) (Sigma, L5668) was used at 1 µg/ml for 1 h. Halo-tagged proteins were labeled by incubating cells with 200 nM HaloTag Ligand conjugated to Janelia Fluor 646 (Promega) for 30 min before imaging. Opaganib (ABC294640) (used at 50 µM up to 10 h) and PF543 (used at 10 µM up to 24 h) were from Selleckchem. Cycloheximide (used at 100 µg/ml for 6 h) was from Sigma-Aldrich.

RNA interference

The pSIREN-RetroQ-Flot2-shRNA (targeting both human and murine Flot2) and pSIREN-RetroQ-Luciferase shRNA vectors have been previously described (Guillaume et al., 2013). Luciferase shRNA (shLuci) was used as a control (Fortier et al., 2008). For RNA-mediated interference experiments, cells were transfected using interferin (Polyplus Transfection) with siRNA oligonucleotide duplexes (Eurogentec). The sequences of the siRNA duplexes were: for human ZEB1, 5′ GGUAGAUGGUAAUGUAAUA 3′ matching the human ZEB1 sequence (NM_001128128.2) (Lehmann et al., 2016); for human ZEB2, 5′ GCAUGUAUGCAUGUGACUU 3′ matching the human ZEB2 sequence (NM_014795.3) (Xia et al., 2010); for human AXL, 5′ CGAAAUCCUCUAUGUCAACAU 3′ matching the human AXL sequence (NM_021913.4) (Antony et al., 2016); control siRNA (Eurogentec, SR-CL000-005); for human SphK2, 5′ GCUGGGCUGUC-CUUCAACCU 3′, matching the human SphK2 sequence (NM_020126.4) (Hait et al., 2005).

Gel electrophoresis and immunoblotting

Protein concentrations in whole-cell lysates were determined with the BCA protein assay kit (Pierce). Proteins from whole-cell lysates (20-60 µg) were

Journal of Cell Science (2022) 135, jcs259178. doi:10.1242/jcs.259178

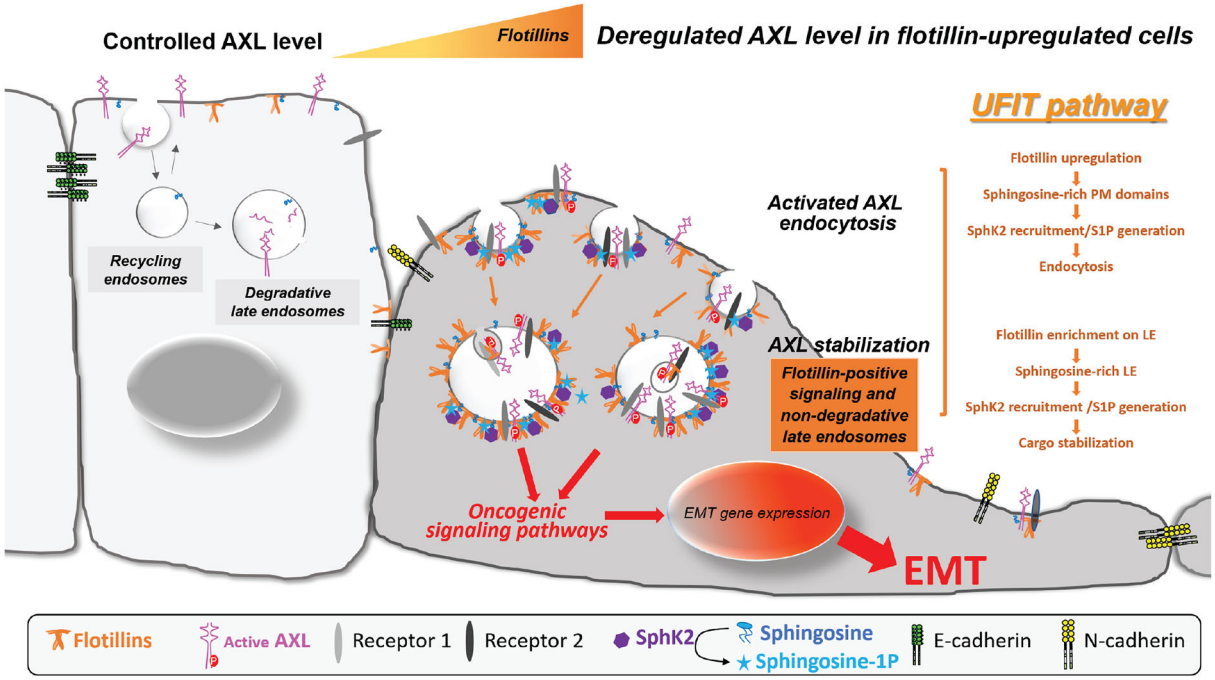

Fig. 7. The UFIT pathway promotes AXL stabilization and EMT. Flotillin 1 and 2 co-upregulation favors their oligomerization and the formation of flotillin-rich microdomains at the PM that initiate the UFIT pathway. At these membrane sites, signaling receptors, including the AXL, are trapped. As sphingosine molecules bind to flotillins, they are concentrated in flotillin-rich microdomains. This favors the recruitment of SPHK2 that phosphorylates sphingosine and promotes S1P production. S1P could promote endocytosis at the PM and influence the LE function. Through the UFIT pathway, AXL is delivered to flotillin-positive LEs, leading to its stabilization. Consequently, these flotillin-positive LEs favor the activation of EMT-promoting oncogenic signaling pathways.

separated on 8-10-12% polyacrylamide gels and transferred to Immobilon-FL membranes (Millipore). Primary and secondary antibodies were diluted in blocking buffer (Millipore) containing 0.1% Tween 20. Detection and analysis were performed using the Odyssey Infrared imaging system (LI-COR Biosciences). Immunoblots were quantified by densitometry using Odyssey V3.0 and Fiji.

Immunoprecipitation

The rabbit polyclonal anti-AXL (CST, 8661) antibody (1 µg) was incubated with Dynabeads Protein G (25 µl) at room temperature for 1 h. Antibody coated-beads were then incubated with 1 mg of proteins from post-nuclear supernatants of the indicated cells at 4°C for 2 h, washed and loaded on SDS-PAGE. Immunoprecipitates were analyzed by western blotting.

Phospho-RTK and phospho-kinase arrays

The Proteome Profiler Human Phospho-RTK array kit and human phospho-kinase antibody array kit (R&D Systems) were used according to the manufacturer's instructions. Both array types were incubated with 200 µg of proteins from post-nuclear supernatants isolated from each tested cell line maintained in complete culture medium for 48 h after seeding.

Measurement of Ras activity

Cells were lysed in lysis buffer A [50 mM Tris (pH 7.5), 10 mM $MgCl_2$, 0.3 M NaCl, 2% (v/v) IGEPAL]. Lysates were then incubated with 30 µg of Ras-GTP Binding Domain (RBD of human c-Raf kinase) fused with GST associated with beads (RF02, Cytoskeleton) at 4°C for 1 h. Prior to incubation with beads, 1/20 of each cell lysate was collected to be used as 'input'. Precipitates and inputs were revealed by western blotting using an anti-pan-Ras antibody.

AXL uptake assays

Cells were seeded in 12 mm sterile poly-lysine-coated round glass coverslips and grown to 60-70% confluence. After 15 min incubation at 4°C in serum-free medium, cells were incubated at 4°C in serum-free medium containing 250 µg/ml of D4 anti-AXL humanized antibody for 45 min. Alternatively, cells transfected with the plasmid encoding N-terminally Myc-tagged AXL (N-Myc-AXL) were incubated with the anti-Myc (9E10) antibody. Cells were extensively washed with cold serum-free medium to remove unbound antibodies and surface-bound antibodies were internalized by incubating cells at 37°C in serum-free medium for the indicated time points. Cells were then fixed and permeabilized, and the internalized primary antibody molecules were detected using the appropriate fluorescent secondary antibody (FITC-conjugated anti-human IgG for cells incubated with the D4 antibody, and Alexa488-conjugated anti-mouse IgG for cells that express N-Myc-AXL). Samples were then processed as described in the 'Immunofluorescence, image acquisition and analysis' section.

Surface biotinylation assays and internalization experiments

Cells were seeded and after 24 h were washed with ice-cold PBS, incubated with biotin NHS [0.2 mg/ml in PBS (pH 7.9)] at 4°C for 45 min, and shifted to 37°C for the indicated times. Cells were then incubated with Mesna buffer at 4°C for 15 min to remove the remaining cell-surface biotin, followed by a 10 min incubation at 4°C with iodoacetamide to stop the action of Mesna. Cells were then scraped in lysis buffer [10 mM Pipes (pH 7), 100 mM NaCl, 300 mM sucrose, 3 mM $MgCl_2$, 0.5% (v/v) IGEPAL CA-640, 1 mM EDTA, 1 mM Na_3VO_4 and protease inhibitor cocktail] and the post-nuclear supernatants were harvested after centrifugation (800 ***g***, 4°C for 10 min). One cell plate was lysed immediately after biotinylation and before incubation with Mesna buffer, and was used to estimate the amount of total labeled surface proteins. An equal protein amount for each time point was incubated with streptavidin-coated agarose beads (at 4°C for 45 min). After two washes in PBS, beads were precipitated and resuspended in Laemmli buffer. Samples were separated by SDS-PAGE followed by western blotting with antibodies against AXL and CD71.

Results from the experiments performed using MCF10AmCh and MCF10AF1F2 cells were not expressed as the percentage of total surface-labeled AXL at t=0 min because AXL expression level in MCF10AF1F2 cells was much stronger than in MCF10AmCh cells (see Figs 3A and 4G). In these conditions, expressing the data classically as the percentage of the

Journal of Cell Science (2022) 135, jcs259178. doi:10.1242/jcs.259178

maximum level of surface-labeled AXL at t=0 min would have led to a strong underestimation of any difference in the internalization rate. Thus, to estimate correctly the internalization rate, results at each time point were expressed as the percentage of the maximum level of internalized protein (reached at 8 min for MCF10AF1F2 cells and at 12 min for MCF10A cells). Because the AXL expression level remained unchanged between untreated MDA-MB-231shLuci cells, MDA-MB-231shLuci cells incubated with opaganib for 4 h and MDA-MB-231shFlot2 cells, and between untreated MCF10AF1F2 cells and MCF10AF1F2 cells incubated with opaganib for 4 h, results at each time point were expressed as the percentage of the maximum level of surface-labeled AXL or CD71 at t=0 min.

Immunofluorescence, image acquisition and analysis

Cells were fixed in 3.2% paraformaldehyde for 10 min, followed by a 2 min permeabilization with 0.1% Triton X-100 or by a 10 min permeabilization with 0.05% saponin, and a 15 min saturation in the presence of 2% BSA. Cells were then incubated with primary and secondary antibodies. For CD63, LAMP1 and flotillin immunostaining, cells were fixed and permeabilized with acetone/methanol (v/v, 1/1) at −20°C for 2 min. Images were taken with a confocal SP5-SMD microscope (Leica) with 40×/1.3 or 63×/1.4 oil HCX PL APO CS objectives (Leica), and captured with a hybrid detector (Leica HyD) controlled using the C software. In some cases, stacks of confocal images with a step size of 0.3 µm were processed with Imaris (Bitplane, Zurich, Switzerland) for visualization and volume rendering. Images were processed using Adobe Photoshop and assembled using Adobe Illustrator. For the colocalization measurements of flotillin1/2-mCherry with AXL-GFP, CD71-GFP and SPHK1/2-GFP in vesicles, images were analyzed with the Fiji software and using the Icy software (http://icy.bioimageanalysis.org); a detailed protocol will be provided upon request.

Quantification of AXL surface staining

Fixed non-permeabilized cells were immunostained using the monoclonal D4 antibody against AXL extracellular domain and an Alexa Fluor 488-conjugated anti-human secondary antibody. Images were acquired by confocal microscopy under identical illuminated conditions. Using the Fiji software, the outline of each cell was defined and the mean fluorescence intensity (taking into account the cell surface) was quantified in the area defined by the outline.

Optogenetic and TIRF microscopy

MCF10A cells were co-transfected with vectors encoding CRY2-mCitrin, flotillin 2-CIBN-mCherry and AXL-Halo labeled with the Halo-Tag-Ligand-Janelia Fluor 646. TIRF images were acquired using an inverted Nikon microscope and a 100×/1.49 oil objective controlled using the Metamorph software (1 image/s). First, Flot2-CIBN-mCherry and AXL-Halo were imaged for 10 s before 488 nm illumination. Cells were then globally illuminated by 22 pulses (1 pulse/s, 100 ms time length for each pulse) of 488 nm light, and CRY2-mCitrin, Flot2-CIBN-mCherry and AXL-Halo signals were simultaneously imaged for 3 min.

Imaging of cells with NBD-sphingosine and Oregon Green-phosphatidylethanolamine

Live cells were incubated with NBD-sphingosine or Oregon Green 488-phosphatidylethanolamine (Avanti-Polar lipids) (0.5 µM) added to the culture medium, and cells were imaged by spinning disk confocal microscopy.

S1P quantitative analysis

Sphingolipid extracts, fortified with internal standards (*N*-dodecanoylsphingosine, *N*-dodecanoylglucosylsphingosine, *N*-dodecanoylsphingosylphosphorylcholine, C17-sphinganine and C17-sphinganine 1-phosphate; 0.2 nmol each), were prepared and analyzed by UPLC-TOF MS as described previously (Cingolani et al., 2014), except for SoP, which was analyzed as follows. Analysis of the extracts was performed with a system consisting of Acquity ultraperformance liquid chromatography (UPLC) (Waters) connected to a triple-quadrupole mass spectrometer (Xevo TQ-S, Waters) and controlled by Waters/Micromass MassLynx software. Detection was performed with an electrospray interface operating in the positive ion mode, capillary voltage set to 3.1 kV, source temperature at 150°C and desolvation temperature at 500°C. The following selected reaction monitoring transitions were acquired: C17 D-*erythro*-dihydrosphingosine-1-phosphate, 368-252 Da, cone voltage 30 V, collision energy 20 eV; and S1P, 380–264 Da, cone voltage 30 V, collision energy 20 eV.

Quantification of SPHK2-GFP delocalization from flotillin-positive LEs

MCF10AF1F2 cells that express SPHK2-GFP were imaged by spinning disk confocal microscopy (1 image/15 min). The Fiji software and images acquired at 0 and 90 min after opaganib (50 µM) addition in the culture medium were used to define same-size individual regions of interest (ROIs) surrounding one flotillin 2-mCherry-positive vesicle. For each ROI, the mean intensity corresponding to the mCherry and the GFP signals were quantified. To take into account the decrease in signal intensity due to photobleaching, quantifications were also carried out on three ROIs of the same size, but outside flotillin 2-mCherry-positive vesicles. The mean of the obtained values was considered as background and subtracted from the GFP and mCherry signals measured in the ROIs surrounding vesicles. The GFP/mCherry signal ratio was then individually calculated for each ROI surrounding a vesicle on images acquired at 0 and 90 min after opaganib addition.

Time-lapse imaging experiments

Time-lapse imaging experiments were performed using an inverted Spinning disk Nikon Ti Andor CSU-X1 microscope equipped with a focus Fluor 100× objective (NA 0.55). Time-series images were acquired with a EMCCD iXon897 Andor camera controlled by the Andor iQ3 software. Time lapse was started 24/48 h after transfection. Time series of the captured images were saved as tiff files that were compiled into avi movies using Fiji software.

Scanning electron microscopy

PBS-washed cells were fixed with 2.5% glutaraldehyde in PHEM buffer (pH 7.2) at room temperature for 1 h, and then washed in PHEM buffer. Fixed cells were dehydrated using a graded ethanol series (30-100%), followed by 10 min in graded ethanol-hexamethyldisilazane and 10 min in hexamethyldisilazane. Samples were then sputter coated with a 10 nm gold film and examined using a scanning electron microscope (Hitachi S4000, at CoMET, MRI-RIO Imaging, Biocampus, INM Montpellier France) and a lens detector with an acceleration voltage of 10 kV at calibrated magnifications.

RNA isolation and sequencing

Total RNA was prepared from MCF10AmCh and MCF10AF1F2 cells using the RNeasy Mini Kit (Qiagen) according to the manufacturer's instructions. RNA quantity and quality were determined with an Agilent RNA 600 Nano Bioanalyser (Agilent Technologies), and total RNA was concentrated to 100 ng/µl. Pure RNA preparations without DNA or protein contamination were used for sequencing. Libraries, processed by Fasteris (Geneva, Switzerland), were prepared with the TruSeq Stranded mRNA Library Prep Kit from Illumina. Fragments were sequenced on an Illumina Hi-Seq 4000 sequencer according to the manufacturer's instructions.

Differential analysis of transcriptomic data

The differential gene expression analysis was carried out using three replicates per condition to compare the transcript levels between MCF10AmCh and MCF10AF1F2 cells. Two analysis methods were used: DESeq (http://bioconductor.org/packages/release/bioc/html/DESeq2.html) and Tuxedo (http://cufflinks.cbcb.umd.edu/).

Genes with a P_{adj}<0.05 were assigned as differentially expressed. The Deseq2 and Tuxedo results were compared. Only genes with an expression fold change >2.8 were considered. Using this criterion, 802 up- and downregulated genes were identified.

Gene functional classification: GO term enrichment analysis and gene set enrichment analysis

The PANTHER (protein annotation through evolutionary relationship, version 13.1) classification system (http://www.pantherdb.org/) was used to

Journal of Cell Science (2022) 135, jcs259178. doi:10.1242/jcs.259178

perform a gene ontology (GO) enrichment. Enriched terms were considered statistically significant when P_{adj}<0.05, and a minimum of five genes were grouped for each significant term. GO terms were categorized in three major functional groups: 'biological process', 'molecular function' and 'cellular component'. A gene set enrichment analysis (GSEA) was performed with the GSEA software v4.1.0. The pre-ranked method was used and the number of permutations was set to 1000. Gene sets with adjusted *q*-values (FDR) <0.25 were considered significant (Subramanian et al., 2005).

Reverse transcription-quantitative real-time PCR (RT-qPCR)

RNA was extracted from the indicated cell lines as described above. mRNA samples were then reverse transcribed to cDNA using SuperScript II Reverse Transcriptase (Thermo Fisher Scientific) and qPCR was performed using an LC480 apparatus (Roche) with the SYBR Green PCR Master Mix (Applied Biosystems). The primer sequences were: for human *CDH1*, forward 5′-TCATGAGTGTCCCCCGGTAT-3′ and reverse 5′-CAGCCGCTTTCAGATTTTCAT-3′; for human *CDH2*, forward 5′-GGCAGAAGAGAGACTGGGTC-3′ and reverse 5′-GAGGCTGGTCAGCTCCTGGC-3′; for human vimentin, Duplex QT00095795 (Qiagen); for human *ZEB1*, forward 5′-GCACCTGAAGAGGACCAGAG-3′ and reverse 5′-TGCATCTGGTGTTCCATTTT-3′; for human *ZEB2*, forward 5′-GGGAGAATTGCTTGATGGAGC-3′ and reverse 5′-TCTCGCCCGAGTGAAGCCTT-3′; for human *MRPL19* (internal control), forward 5′-GGGATTTGCATTCAGAGATCAG-3′ and reverse 5′-GGAAGGGCATCTCGTAAG-3′; for murine *Cdh1*, forward 5′-GGTCTCTTGTCCCCACA-3′ and reverse 5′-CCTGACCCACACCAAAGTCT-3′; for murine *Cdh2*, forward 5′-AGGGTGGACGTCATTGTAGC-3′ and reverse 5′-CTGTTGGGGTCTGTCAGGAT-3′; for murine vimentin, forward 5′-AATGCTTCTCTGGCACGTCT-3′ and reverse 5′-GCTCCTGGATCTCTTCATCG-3′; for murine *Zeb1*, forward 5′-GCTCAGCCAGGAACCCGCAG-3′ and reverse 5′-TGGGCACCCTCTGCCACACA-3′; for murine *Zeb2*, forward 5′-ATGGCAACACATGGGTTTAGTGGC-3′ and reverse 5′-ATTGGACTCTGAGCAGATGGGTGT-3′; for murine *Mrpl32* (internal control), forward 5′-TTAAGCGAAACTGGCGGAAAC-3′ and reverse 5′-TTGTTGCTCCCATAACCGATG-3′; and for human AXL, forward 5′-GTGGGCAACCCAGGGAATATC-3′ and reverse 5′-GTACTGTCCCGTGTCGGAAAG-3′.

RT-qPCR analysis of breast tumor samples

The mRNA levels of flotillin 1 and ΔNp63 in tumor samples from the cohort of patients with breast cancer were analyzed as described previously (Rossé et al., 2014).

Boyden chamber migration assay

Cells (5×10^4) were seeded on the upper chamber of the Boyden chamber inserts (Corning FluoroBlok cell culture insert, 8 µm pores) in 250 µl of DMEM/F12 with 1% horse serum. In the lower chamber, complete medium (750 µl) was added, as a chemoattractant. Opaganib (50 µM) was added in the upper and lower chambers.

After 14 h, cells at the bottom of the filter were fixed with 3.2% paraformaldehyde and stained with Hoechst. The nucleus of cells that had migrated through the pores was imaged with an EVOS microscope (Life Technologies) using a 10× objective. Semi-automatic quantification was performed with Fiji. For each experiment, each condition was performed in triplicate.

Patients and specimens

Patients (*n*=43) with invasive breast carcinoma were treated at the Cancer Research Institute, Tomsk NRMC (Tomsk, Russia). Frozen and formalin-fixed paraffin-embedded (FFPE) tumor tissue specimens obtained during surgery were used for immunofluorescence analyses.

The histological type was defined according to the World Health Organization recommendations (Lakhani et al., 2012). Tumor grade was determined using the Bloom and Richardson grading system (Bloom and Richardson, 1957). The expression of estrogen receptor (ER) and progesterone receptor (PR) was scored using the HSCORE method (Kinsel et al., 1989). HER2 expression was analyzed by immunohistochemistry and calculated on a scale 0-3+, according to the ASCO/CAP guidelines (Wolff et al., 2007). Ki-67 expression was calculated as the percentage of Ki-67-positive tumor cells relative to all tumor cells. Molecular subtypes were categorized on the basis of the primary tumor ER, PR, HER2 and Ki-67 status, according to the St Gallen recommendations (Wolff et al., 2007): luminal A (ER^+ and/or PR^+, $HER2^-$ and Ki-67<20%), luminal B (ER^+ and/or PR^+, $HER2^{+/-}$ and Ki-67≥20%), $HER2^+$ (ER^- and PR^-, $HER2^+$) and triple negative (ER^-, PR^- and $HER2^-$). The study procedures were in accordance with the Helsinki Declaration (1964, amended in 1975 and 1983). This study was approved by the institutional review board of the Cancer Research Institute, Tomsk National Research Medical Center, Tomsk, Russia; all patients signed an informed consent for voluntary participation.

Clinicopathological characteristics were noted for the patients who gave the breast cancer samples used for the analysis (Fig. S4).

Triple-negative subtype

Patient 1: 65-year-old woman, invasive carcinoma (left side), T2N1M0, grade 3, ER^-, PR^-, $HER2^-$, Ki-67-positive cells (50%), triple negative. Lymph node positive (one metastasis from six lymph nodes). Five courses of neoadjuvant chemotherapy.

Patient 2: 55-year-old woman, invasive carcinoma (left side), T1N0M1, multifocal, grade 2, ER^-, PR^-, $HER2^-$, Ki-67-positive cells (31%), triple negative. Lymph node negative (0 metastases in seven lymph nodes). Six courses of neoadjuvant chemotherapy.

Patient 3: 55-year-old woman, invasive carcinoma (left side), T2N1M0, grade 2, ER^-, PR^-, $HER2^-$, Ki-67-positive cells (31%), triple negative. Lymph node negative (0 metastases in seven lymph nodes). Six courses of neoadjuvant chemotherapy.

Patient 4: 55-year-old woman, invasive carcinoma (left side), T1N0M0, grade 3, ER^-, PR^-, $HER2^-$, Ki-67-positive cells (52%), triple negative. Lymph node-negative (0 metastases from 11 lymph nodes). No neoadjuvant chemotherapy.

Patient 5: 48-year-old woman, invasive carcinoma (right side), T2N1M0, grade 3, ER^-, PR^-, $HER2^-$, Ki-67-positive cells (37%), triple negative. Lymph node positive (two metastases from eight lymph nodes). Five courses of neoadjuvant chemotherapy.

Patient 6: 48-year-old woman, invasive carcinoma (left side), T2N1M0, grade 3, ER^-, PR^-, $HER2^-$, Ki-67-positive cells (80%), triple negative. Lymph node negative (0 metastases from 10 lymph nodes). Six courses of neoadjuvant chemotherapy.

Patient 7: 24-year-old woman, invasive carcinoma (left side), T4N0M0, grade 2, ER^-, PR^-, $HER2^-$, Ki-67-positive cells (60%), triple negative. Lymph node negative (0 metastases from 10 lymph nodes). Six courses of neoadjuvant chemotherapy.

Patient 8: 59-year-old woman, invasive carcinoma (right side), T1N1M0, grade 2, ER^-, PR^-, $HER2^-$, Ki-67-positive cells (61%), triple negative. Lymph node positive (one metastasis from eight lymph nodes). No neoadjuvant chemotherapy.

Patient 9: 51-year-old woman, invasive carcinoma (right side), T2N1M0, grade 2, ER^-, PR^-, $HER2^-$, Ki-67-positive cells (48%), triple negative. Lymph node positive (one metastasis from 10 lymph nodes). Five courses of neoadjuvant chemotherapy.

Patient 10: 65-year-old woman, invasive carcinoma (left side), T1N1M0, grade 2, ER^-, PR^-, $HER2^-$, Ki-67-positive cells (50%), triple negative. Lymph node positive (one metastasis from 10 lymph nodes). No neoadjuvant chemotherapy.

Patient 11: 60-year-old woman, invasive carcinoma (left side), T2N0M0, grade 2, ER^-, PR^-, $HER2^-$, Ki-67-positive cells (45%), triple negative. Lymph node negative (0 metastases from eight lymph nodes). No neoadjuvant chemotherapy.

Patient 12: 43-year-old woman, invasive carcinoma (left side), T2N0M0, grade 2, ER^-, PR^-, $HER2^-$, Ki-67-positive cells (60%), triple negative. Lymph node negative (0 metastases from eight lymph nodes). No neoadjuvant chemotherapy.

Patient 13: 54-year-old woman, invasive carcinoma (right side), T2N1M0, grade 3, ER^-, PR^-, $HER2^-$, Ki-67-positive cells (60%), triple negative. Lymph node positive (one metastasis from 11 lymph nodes). Six courses of neoadjuvant chemotherapy.

Journal of Cell Science (2022) 135, jcs259178. doi:10.1242/jcs.259178

Patient 14: 65-year-old woman, invasive carcinoma (left side), T3N2M0, grade 2, ER$^-$, PR$^-$, HER2$^-$, Ki-67-positive cells (80%), triple negative. Lymph node positive (four metastasis from 12 lymph nodes). Six courses of neoadjuvant chemotherapy.

Patient 15: 59-year-old woman, invasive carcinoma (left side), T1N1M0, grade 2, ER$^-$, PR$^-$, HER2$^-$, Ki-67-positive cells (74%), triple negative. Lymph node positive (one metastasis from nine lymph nodes). Six courses of neoadjuvant chemotherapy.

Luminal subtype

Patient 1: 49-year-old woman, invasive carcinoma (right side), T2N0M0, grade 2, ER+, PR+, HER2$^-$, Ki-67-positive cells (10%), luminal. Lymph node negative (0 metastases in three lymph nodes). No neoadjuvant chemotherapy.

Patient 2: 66-year-old woman, invasive carcinoma (right side), T2N1M0, grade 2, ER$^+$, PR$^+$, Her2$^-$, Ki-67-positive cells (35%), luminal. Lymph node positive (3/10 lymph nodes with metastases). No neoadjuvant chemotherapy.

Patient 3: 40-year-old woman, invasive carcinoma (right side), T2N1M0, grade 2, ER$^+$, PR$^+$, HER2$^-$, Ki-67-positive cells (33%), luminal. Lymph node positive (2/10 lymph nodes with metastases). No neoadjuvant chemotherapy.

Patient 4: 46-year-old woman, invasive carcinoma (right side), T2N1M0, grade 2, ER$^+$, PR$^-$, HER2$^-$, Ki-67-positive cells (12%), luminal. Lymph node positive (5/6 lymph nodes with metastases). No neoadjuvant chemotherapy.

Patient 5: 57-year-old woman, invasive carcinoma (right side), T4N3M0, grade 2, ER$^+$, PR$^+$, HER2$^-$, Ki-67-positive cells (17%), luminal. Lymph node positive (2/6 lymph nodes with metastases). Six courses of neoadjuvant chemotherapy.

Patient 6: 32-year-old woman, invasive carcinoma (right side), T2N1M0, grade 2, ER$^+$, PR$^+$, HER2$^-$, Ki-67-positive cells (10%), luminal. Lymph node positive (6/10 lymph nodes with metastases). No neoadjuvant chemotherapy.

Patient 7: 60-year-old woman, invasive carcinoma (left side), T2N1M0, grade 2, ER$^+$, PR$^+$, HER2$^-$, Ki-67-positive cells (30%), luminal. Lymph node positive (2/11 lymph nodes with metastases). Six courses of neoadjuvant chemotherapy.

Patient 8: 45-year-old woman, invasive carcinoma (right side), T2N1M0, grade 2, ER$^+$, PR$^-$, HER2$^-$, Ki-67-positive cells (21%), luminal. Lymph node negative (0 metastases from 8 lymph nodes). No neoadjuvant chemotherapy.

Patient 9: 36-year-old woman, invasive carcinoma (left side), T2N0M0, grade 2, ER$^+$, PR$^+$, HER2$^-$, Ki-67-positive cells (28%), luminal. Lymph node negative (0 metastases from six lymph nodes). No neoadjuvant chemotherapy.

Patient 10: 60-year-old woman, invasive carcinoma (left side), T2N0M0, grade 3, ER$^+$, PR$^+$, HER2$^-$, Ki-67-positive cells (10%), luminal. Lymph node negative (0 metastases from 10 lymph nodes). No neoadjuvant chemotherapy.

Patient 11: 55-year-old woman, invasive carcinoma (left side), T2N1M0, grade 3, ER$^+$, PR$^+$, HER2$^-$, Ki-67-positive cells (25%), luminal. Lymph node positive (1/10 lymph nodes with metastases). No neoadjuvant chemotherapy.

Patient 12: 56-year-old woman, invasive carcinoma (left side), T2N1M0, grade 2, ER$^+$, PR$^+$, HER2$^-$, Ki-67-positive cells (10%), luminal. Lymph node positive (2/7 lymph nodes with metastases). No neoadjuvant chemotherapy.

Patient 13: 62-year-old woman, invasive carcinoma (right side), T1N0M0, grade 2, ER$^+$, PR$^-$, HER2$^-$, Ki-67-positive cells (20%), luminal. Lymph node negative (0 metastases from 10 lymph nodes). Six courses of neoadjuvant chemotherapy.

Patient 14: 48-year-old woman, invasive carcinoma (left side), T2N0M0, grade 2, ER$^+$, PR$^-$, HER2$^-$, Ki-67-positive cells (10%), luminal. Lymph node negative (0 metastasis in 9 lymph nodes). No neoadjuvant chemotherapy.

Patient 15: 56-year-old woman, invasive carcinoma (left side), T2N1M0, grade 2, ER$^+$, PR$^+$, HER2$^+$, Ki-67-positive cells (25%), luminal. Lymph node positive (1/10 lymph nodes with metastases). Six courses of neoadjuvant chemotherapy.

Patient 16: 52-year-old woman, invasive carcinoma (right side), T2N2M0, grade 3, ER$^+$, PR$^+$, HER2$^-$, Ki-67-positive cells (33%), luminal. Lymph node positive (6/18 lymph nodes with metastases). Six courses of neoadjuvant chemotherapy.

Patient 17: 53-year-old woman, invasive carcinoma (right side), T1N1M0, grade 2, ER$^+$, PR$^-$, HER2$^-$, Ki-67-positive cells (12%), luminal. Lymph node negative (0 metastases in 8 lymph nodes). No neoadjuvant chemotherapy.

HER2 subtype

Patient 1: 47-year-old woman, invasive carcinoma (right side), multifocal, T4N2aM0, grade 3, ER$^-$, PR$^-$, HER2$^+$; Ki-67-positive cells (65%). Lymph node positive (7/16 lymph nodes with metastases). Six courses of neoadjuvant chemotherapy.

Patient 2: 52-year-old woman, invasive carcinoma (left side), T2N1M0, grade 2, ER$^-$, PR$^-$, HER2$^+$; Ki-67-positive cells (42%). Lymph node positive (6/18 lymph nodes with metastases). No neoadjuvant chemotherapy. Distant metastasis in liver and lung.

Patient 3: 58-year-old woman, invasive carcinoma (right side), T1N0M0, grade 2, ER$^-$, PR$^-$, HER2$^+$; Ki-67-positive cells (35%). Lymph node positive (6/10 lymph nodes with metastases). Six courses of neoadjuvant chemotherapy.

Patient 4: 37-year-old woman, invasive carcinoma (right side), T2N0M0, grade 2, ER$^-$, PR$^-$, HER2$^+$; Ki-67-positive cells (50%). Lymph node negative (0/11 lymph nodes with metastases). Six courses of neoadjuvant chemotherapy.

Patient 5: 56-year-old woman, invasive carcinoma (left side), T3N1M0, grade 3, ER$^-$, PR$^-$, HER2$^+$; Ki-67-positive cells (34%). Lymph node positive (1/15 lymph nodes with metastases). Six courses of neoadjuvant chemotherapy.

Patient 6: 64-year-old woman, invasive carcinoma (left side), T2N0M0, grade 2, ER$^-$, PR$^-$, HER2$^+$; Ki-67-positive cells (70%). Lymph node negative (0 lymph nodes with metastases from 6 lymph nodes). Six courses of neoadjuvant chemotherapy.

Patient 7: 41-year-old woman, invasive carcinoma (left side), T2N1M0, grade 2, ER$^-$, PR$^-$, HER2$^+$; Ki-67-positive cells (76%). Lymph node negative (0 lymph nodes with metastases from 8 lymph nodes). Six courses of neoadjuvant chemotherapy.

Patient 8: 51-year-old woman, invasive carcinoma (right side), T2N1M0, grade 2, ER$^-$, PR$^-$, HER2$^+$; Ki-67-positive cells (60%). Lymph node positive (2/6 lymph nodes with metastases). Six courses of neoadjuvant chemotherapy.

Patient 9: 50-year-old woman, invasive carcinoma (left side), T2N1M0, grade 2, ER$^-$, PR$^-$, HER2$^+$; Ki-67-positive cells (54%). Lymph node positive (2/8 lymph nodes with metastases). Six courses of neoadjuvant chemotherapy.

Patient 10: 53-year-old woman, invasive carcinoma (right side), multifocal, T3N1M0, grade 2, ER$^-$, PR$^-$, HER2$^+$; Ki-67-positive cells (55%). Lymph node positive (1/15 lymph nodes with metastases). Six courses of neoadjuvant chemotherapy.

Patient 11: 56-year-old woman, invasive carcinoma (right side), T3N2M0, grade 3, ER$^-$, PR$^-$, HER2$^+$; Ki-67-positive cells (45%). Lymph node positive (8 metastases in 10 lymph nodes). Six courses of neoadjuvant chemotherapy.

Cancer-free samples

The clinicopathological characteristics of the patients without cancer who gave the breast samples used for this expression analysis were:

Patient 1: 32-year-old woman, fibrocystic breast disease (left side).
Patient 2: 54-year-old woman, fibrocystic breast disease (left side).
Patient 3: 45-year-old woman, fibrocystic breast disease (left side).
Patient 4: 55-year-old woman, fibrocystic breast disease (right side).
Patient 5: 37-year-old woman, fibrocystic breast disease (right side).
Patient 6: 28-year-old woman, fibrocystic breast disease (left side).

Immunofluorescence staining of patient tumor samples

FFPE tumor sections (7 µm) were deparaffinized, rehydrated, processed for heat-induced epitope retrieval with EDTA buffer (pH 8.0) using PT Link

(Dako, Denmark), and blocked with 3% bovine serum albumin (Amresco, USA) in PBS. Expression of flotillin 1 (F1180, 1:50, Sigma) and AXL (C89E7, CST) was assessed using the BondRXm immunostainer (Leica). TSA visualization was performed with Opal 520 and Opal 690 (Opal seven-color IHC Kit; NEL797B001KT; PerkinElmer), nuclei were stained with DAPI, and samples were mounted in Fluorescence Mounting Medium (Dako, Denmark). Samples were analyzed using the Vectra 3.0 Automated Quantitative Pathology Imaging System (PerkinElmer).

Statistical analysis

All statistical analyses and graphs were performed with GraphPad Prism version 9. All data were first tested for normality using the Kolmogorov-Smirnov normality test. For experiments with $n>30$, an unpaired, two-tailed Student's *t*-test was used to identify significant differences between experimental conditions. For experiments with $n<30$, the non-parametric Mann-Whitney *U*-test was used. The *n* value and number of independent experiments are listed in the figure legends. At least four independent experiments were performed. In the figures, only significant differences are indicated. For experiments measuring AXL and CD71 decay over time upon incubation with CHX, non-linear regression with least squares fitting was used.

Acknowledgements

We thank Peggy Raynaud, Dominique Helmlinger, Dylane Detilleux, Christelle Dantec, Dimitris Xirodimas and Nathalie Abadie-Andrieu. We acknowledge the imaging facility MRI (supported by the French National Research Agency ANR-10-INBS-04).

Competing interests

The authors declare no competing or financial interests.

Author contributions

Conceptualization: M.G., F.C., C.G.-R., S.B.; Methodology: M.G., F.C., P.G., B.R., A.S., C.G.-R., S.B., D.N., J.C.; Validation: C.G.-R., S.B.; Formal analysis: S.V., I.B., L.A.T., S.B., D.N., J.C.; Investigation: M.G., F.C., D.P., P.G., H.M., A.S., L.A.T., C.G.-R., S.B., D.N.; Writing - original draft: C.G.-R., S.B.; Writing - review & editing: C.G.-R., S.B.; Visualization: C.G.-R., S.B.; Supervision: C.G.-R., S.B.; Project administration: C.G.-R., S.B.; Funding acquisition: C.G.-R., S.B.

Funding

This work was supported by the Fondation pour la Recherche Médicale (DEQ20161136700) and the Fondation ARC pour la recherche sur le cancer (ARCPJA32020060002078). Collection of breast tumor samples was supported by the Russian Science Foundation (19-75-30016). C.G.-R. was supported by the Institut National de la Santé et de la Recherche Médicale.

Data availability

The RNAseq data have deposited in GEO under accession number GSE190176.

Peer review history

The peer review history is available online at https://journals.biologists.com/jcs/article-lookup/doi/10.1242/jcs.259178.

References

Amaddii, M., Meister, M., Banning, A., Tomasovic, A., Mooz, J., Rajalingam, K. and Tikkanen, R. (2012). Flotillin-1/reggie-2 protein plays dual role in activation of receptor-tyrosine kinase/mitogen-activated protein kinase signaling. *J. Biol. Chem.* **287**, 7265-7278. doi:10.1074/jbc.M111.287599

Antony, J., Tan, T. Z., Kelly, Z., Low, J., Choolani, M., Recchi, C., Gabra, H., Thiery, J. P. and Huang, R. Y.-J. (2016). The GAS6-AXL signaling network is a mesenchymal (Mes) molecular subtype-specific therapeutic target for ovarian cancer. *Sci. Signal.* **9**, ra97. doi:10.1126/scisignal.aaf8175

Antony, J., Zanini, E., Kelly, Z., Tan, T. Z., Karali, E., Alomary, M., Jung, Y., Nixon, K., Cunnea, P., Fotopoulou, C. et al. (2018). The tumour suppressor OPCML promotes AXL inactivation by the phosphatase PTPRG in ovarian cancer. *EMBO Rep.* **19**, e45670. doi:10.15252/embr.201745670

Asiedu, M. K., Beauchamp-Perez, F. D., Ingle, J. N., Behrens, M. D., Radisky, D. C. and Knutson, K. L. (2014). AXL induces epithelial-to-mesenchymal transition and regulates the function of breast cancer stem cells. *Oncogene* **33**, 1316-1324. doi:10.1038/onc.2013.57

Babuke, T., Ruonala, M., Meister, M., Amaddii, M., Genzler, C., Esposito, A. and Tikkanen, R. (2009). Hetero-oligomerization of reggie-1/flotillin-2 and reggie-2/flotillin-1 is required for their endocytosis. *Cell. Signal.* **21**, 1287-1297. doi:10.1016/j.cellsig.2009.03.012

Bae, S. Y., Hong, J.-Y., Lee, H.-J., Park, H. J. and Lee, S. K. (2015). Targeting the degradation of AXL receptor tyrosine kinase to overcome resistance in gefitinib-resistant non-small cell lung cancer. *Oncotarget* **6**, 10146-10160. doi:10.18632/oncotarget.3380

Bailey, M. H., Tokheim, C., Porta-Pardo, E., Sengupta, S., Bertrand, T., Weerasinghe, A., Colaprico, A., Wendl, M. C., Kim, J., Reardon, B. et al. (2018). Comprehensive characterization of cancer driver genes and mutations. *Cell* **173**, 371-385.e18. doi:10.1016/j.cell.2018.02.060

Berger, T., Ueda, T., Arpaia, E., Chio, I. I. C., Shirdel, E. A., Jurisica, I., Hamada, K., You-Ten, A., Haight, J., Wakeham, A. et al. (2013). Flotillin-2 deficiency leads to reduced lung metastases in a mouse breast cancer model. *Oncogene* **32**, 4989-4994. doi:10.1038/onc.2012.499

Bessette, D. C., Tilch, E., Seidens, T., Quinn, M. C. J., Wiegmans, A. P., Shi, W., Cocciardi, S., Mccart-Reed, A., Saunus, J. M., Simpson, P. T. et al. (2015). Using the MCF10A/MCF10CA1a breast cancer progression cell line model to investigate the effect of active, mutant forms of EGFR in breast cancer development and treatment using gefitinib. *PLoS ONE* **10**, 1-25. doi:10.1371/journal.pone.0125232

Bloom, H. J. G. and Richardson, W. W. (1957). Histological grading and prognosis in breast cancer a study of 1409 cases of which 359 have been followed for 15 years. *Br. J. Cancer* **11**, 359-377. doi:10.1038/bjc.1957.43

Britten, C. D., Garrett-Mayer, E., Chin, S. H., Shirai, K., Ogretmen, B., Bentz, T. A., Brisendine, A., Anderton, K., Cusack, S. L., Maines, L. W. et al. (2017). A phase I study of ABC294640, a first-in-class sphingosine kinase-2 inhibitor, in patients with advanced solid tumors. *Clin. Cancer Res.* **23**, 4642-4650. doi:10.1158/1078-0432.CCR-16-2363

Budi, E. H., Muthusamy, B.-P. and Derynck, R. (2015). The insulin response integrates increased TGF-β signaling through Akt-induced enhancement of cell surface delivery of TGF-β receptors. *Sci. Signal.* **8**, ra966. doi:10.1126/scisignal.aaa9432

Cao, S., Cui, Y., Xiao, H., Mai, M., Wang, C., Xie, S., Yang, J., Wu, S., Li, J., Song, L. et al. (2016). Upregulation of flotillin-1 promotes invasion and metastasis by activating TGF-β signaling in nasopharyngeal carcinoma. *Oncotarget* **7**, 4252-4264. doi:10.18632/oncotarget.6483

Chew, H. Y., De Lima, P. O., Gonzalez Cruz, J. L., Banushi, B., Echejoh, G., Hu, L., Joseph, S. R., Lum, B., Rae, J., O'Donnell, J. S. et al. (2020). Endocytosis inhibition in humans to improve responses to ADCC-mediating antibodies. *Cell* **180**, 895-914.e27. doi:10.1016/j.cell.2020.02.019

Cingolani, F., Casasampere, M., Sanllehí, P., Casas, J., Bujons, J. and Fabrias, G. (2014). Inhibition of dihydroceramide desaturase activity by the sphingosine kinase inhibitor SKI II. *J. Lipid Res.* **55**, 1711-1720. doi:10.1194/jlr.M049759

De Craene, B. , and Berx, G. (2013). Regulatory networks defining EMT during cancer initiation and progression. *Nat. Rev. Cancer* **13**, 97-110. doi:10.1038/nrc3447

Dermine, J.-F., Duclos, S., Garin, J., St-Louis, F., Rea, S., Parton, R. G. and Desjardins, M. (2001). Flotillin-1-enriched lipid raft domains accumulate on maturing phagosomes. *J. Biol. Chem.* **276**, 18507-18512. doi:10.1074/jbc.M101113200

Dobrowolski, R. and De Robertis, E. M. (2008). Endocytic control of growth factor signalling: multivesicular bodies as signalling organelles. *Nat. Rev. Mol. Cell Biol.* **13**, 53-60. doi:10.1038/nrm3244

Dongre, A. and Weinberg, R. A. (2018). New insights into the mechanisms of epithelial-mesenchymal transition and implications for cancer. *Nat. Rev. Mol. Cell Biol.* **20**, 69-84. doi:10.1038/s41580-018-0080-4

Fortier, M., Comunale, F., Kucharczak, J., Blangy, A., Charrasse, S. and Gauthier-Rouvière, C. (2008). RhoE controls myoblast alignment prior fusion through RhoA and ROCK. *Cell Death Differ.* **15**, 1221-1231. doi:10.1038/cdd.2008.34

Frick, M., Bright, N. A., Riento, K., Bray, A., Merrified, C. and Nichols, B. J. (2007). Coassembly of flotillins induces formation of membrane microdomains, membrane curvature, and vesicle budding. *Curr. Biol.* **17**, 1151-1156. doi:10.1016/j.cub.2007.05.078

Gauthier-Rouvière, C., Bodin, S., Comunale, F. and Planchon, D. (2020). Flotillin membrane domains in cancer. *Cancer Metastasis Rev.* **39**, 361-374. doi:10.1007/s10555-020-09873-y

Gay, C. M., Balaji, K. and Byers, L. A. (2017). Giving AXL the axe: targeting AXL in human malignancy. *Br. J. Cancer* **116**, 415-423. doi:10.1038/bjc.2016.428

Gjerdrum, C., Tiron, C., Hoiby, T., Stefansson, I., Haugen, H., Sandal, T., Collett, K., Li, S., Mccormack, E., Gjertsen, B. T. et al. (2010). Axl is an essential epithelial-to-mesenchymal transition-induced regulator of breast cancer metastasis and patient survival. *Proc. Natl Acad. Sci. USA* **107**, 1124-1129. doi:10.1073/pnas.0909333107

Glebov, O. O., Bright, N. A. and Nichols, B. J. (2006). Flotillin-1 defines a clathrin-independent endocytic pathway in mammalian cells. *Nat. Cell Biol.* **8**, 46-54. doi:10.1038/ncb1342

Gonnord, P., Blouin, C. M. and Lamaze, C. (2012). Membrane trafficking and signaling: Two sides of the same coin. *Semin. Cell Dev. Biol.* **23**, 154-164. doi:10.1016/j.semcdb.2011.11.002

Goyette, M.-A., Duhamel, S., Aubert, L., Pelletier, A., Savage, P., Thibault, M.-P., Johnson, R. M., Carmeliet, P., Basik, M., Gaboury, L. et al. (2018). The receptor

tyrosine kinase AXL is required at multiple steps of the metastatic cascade during HER2-positive breast cancer progression. *Cell Rep.* **23**, 1476-1490. doi:10.1016/j.celrep.2018.04.019

Gregory, P. A., Bracken, C. P., Smith, E., Bert, A. G., Wright, J. A., Roslan, S., Morris, M., Wyatt, L., Farshid, G., Lim, Y.-Y. et al. (2011). An autocrine TGF-/ZEB/miR-200 signaling network regulates establishment and maintenance of epithelial-mesenchymal transition. *Mol. Biol. Cell* **22**, 1686-1698. doi:10.1091/mbc.e11-02-0103

Gröger, C. J., Grubinger, M., Waldhör, T., Vierlinger, K. and Mikulits, W. (2012). Meta-analysis of gene expression signatures defining the epithelial to mesenchymal transition during cancer progression. *PLoS ONE* **7**, 1-10. doi:10.1371/journal.pone.0051136

Guillaume, E., Comunale, F., Do Khoa, N., Planchon, D., Bodin, S. and Gauthier-Rouviere, C. (2013). Flotillin microdomains stabilize cadherins at cell-cell junctions. *J. Cell Sci.* **126**, 5293-5304. doi:10.1242/jcs.133975

Hachim, I. Y., Villatoro, M., Canaff, L., Hachim, M. Y., Boudreault, J., Haiub, H., Ali, S. and Lebrun, J.-J. (2017). Transforming growth factor-beta regulation of Ephrin Type-A receptor 4 signaling in breast cancer cellular migration. *Sci. Rep.* **7**, 14976. doi:10.1038/s41598-017-14549-9

Hait, N. C., Sarkar, S., Le Stunff, H., Mikami, A., Maceyka, M., Milstien, S. and Spiegel, S. (2005). Role of sphingosine kinase 2 in cell migration toward epidermal growth factor. *J. Biol. Chem.* **280**, 29462-29469. doi:10.1074/jbc.M502922200

Hatoum, D., Haddadi, N., Lin, Y., Nassif, N. T. and Mcgowan, E. M. (2017). Mammalian sphingosine kinase (SphK) isoenzymes and isoform expression: challenges for SphK as an oncotarget. *Oncotarget* **8**, 36898-36929. doi:10.18632/oncotarget.16370

Hu, L., Liang, S., Chen, H., Lv, T., Wu, J., Chen, D., Wu, M., Sun, S., Zhang, H., You, H. et al. (2017). ΔNp63α is a common inhibitory target in oncogenic PI3K/Ras/Her2-induced cell motility and tumor metastasis. *Proc. Natl Acad. Sci. USA* **114**, E3964-E3973. doi:10.1073/pnas.1617816114

Joseph, S. R., Gaffney, D., Barry, R., Hu, L., Banushi, B., Wells, J. W., Lambie, D., Strutton, G., Porceddu, S. V., Burmeister, B. et al. (2019). An ex vivo human tumor assay shows distinct patterns of EGFR trafficking in squamous cell carcinoma correlating to therapeutic outcomes. *J. Investig. Dermatol.* **139**, 213-223. doi:10.1016/j.jid.2018.06.190

Kajimoto, T., Okada, T., Miya, S., Zhang, L. and Nakamura, S.- (2013). Ongoing activation of sphingosine 1-phosphate receptors mediates maturation of exosomal multivesicular endosomes. *Nat. Commun.* **4**, 2712. doi:10.1038/ncomms3712

Kinsel, L. B., Szabo E., Greene, G. L., Konrath, J., Leight, G. S. and McCarty, K. S., Jr (1989). Immunocytochemical analysis of estrogen receptors as a predictor of prognosis in breast cancer patients: comparison with quantitative biochemical methods. *Cancer Res.* **49**, 1052-1056.

Krishnamoorthy, G. P., Guida, T., Alfano, L., Avilla, E., Santoro, M., Carlomagno, F. and Melillo, R. M. (2013). Molecular mechanism of 17-allylamino-17-demethoxygeldanamycin (17-AAG)-induced AXL receptor tyrosine kinase degradation. *J. Biol. Chem.* **288**, 17481-17494. doi:10.1074/jbc.M112.439422

Lakhani, S. R., Schnitt, S. J. and Tan Ph, V. M. (2012). World Health Organization Classification of Tumours of the Breast. WHO classification of tumours of the breast: views of a working group that convened for a consensus and editorial meeting at the International Agency for Research on Cancer (IARC), Lyon, September 1-3, 2011. 4. ed.

Langhorst, M. F., Jaeger, F. A., Mueller, S., Sven Hartmann, L., Luxenhofer, G. and Stuermer, C. A. O. (2008). Reggies/flotillins regulate cytoskeletal remodeling during neuronal differentiation via CAP/ponsin and Rho GTPases. *Eur. J. Cell Biol.* **87**, 921-931. doi:10.1016/j.ejcb.2008.07.001

Leconet, W., Larbouret, C., Chardès, T., Thomas, G., Neiveyans, M., Busson, M., Jarlier, M., Radosevic-Robin, N., Pugnière, M., Bernex, F. et al. (2014). Preclinical validation of AXL receptor as a target for antibody-based pancreatic cancer immunotherapy. *Oncogene* **33**, 5405-5414. doi:10.1038/onc.2013.487

Leconet, W., Chentouf, M., Du Manoir, S., Chevalier, C., Sirvent, A., Aït-Arsa, I., Busson, M., Jarlier, M., Radosevic-Robin, N., Theillet, C. et al. (2017). Therapeutic activity of anti-AXL antibody against triple-negative breast cancer patient-derived xenografts and metastasis. *Clin. Cancer Res.* **23**, 2806-2816. doi:10.1158/1078-0432.CCR-16-1316

Lehmann, W., Mossmann, D., Kleemann, J., Mock, K., Meisinger, C., Brummer, T., Herr, R., Brabletz, S., Stemmler, M. P. and Brabletz, T. (2016). ZEB1 turns into a transcriptional activator by interacting with YAP1 in aggressive cancer types. *Nat. Commun.* **7**, 10498. doi:10.1038/ncomms10498

Lima, S., Milstien, S. and Spiegel, S. (2017). Sphingosine and sphingosine kinase 1 involvement in endocytic membrane trafficking. *J. Biol. Chem.* **292**, 3074-3088. doi:10.1074/jbc.M116.762377

Liu, Y., Lin, L., Huang, Z., Ji, B., Mei, S., Lin, Y. and Shen, Z. (2015). High expression of flotillin-2 is associated with poor clinical survival in cervical carcinoma. *Int. J. Clin. Exp. Pathol.* **8**, 622-628.

Lu, A., Tebar, F., Alvarez-Moya, B., López-Alcalá, C., Calvo, M., Enrich, C., Agell, N., Nakamura, T., Matsuda, M. and Bachs, O. (2009). A clathrin-dependent pathway leads to KRas signaling on late endosomes en route to lysosomes. *J. Cell Biol.* **184**, 863-879. doi:10.1083/jcb.200807186

Mellman, I. and Yarden, Y. (2013). Endocytosis and cancer. *Cold Spring Harbor Perspect. Biol.* **5**, a016949. doi:10.1101/cshperspect.a016949

Mohamed, N. N. I., Okada, T., Kajimoto, T. and Nakamura, S.-I. (2017). Essential role of sphingosine kinase 2 in the regulation of cargo contents in the exosomes from K562 cells. *Kobe J. Med. Sci* **63**, 123-129. http://www.med.kobe-u.ac.jp/journal/contents/63/E123.pdf.

Murphy, J. E., Padilla, B. E., Hasdemir, B., Cottrell, G. S. and Bunnett, N. W. (2009). Endosomes: A legitimate platform for the signaling train. *Proc. Natl Acad. Sci. USA* **106**, 17615-17622. doi:10.1073/pnas.0906541106

Neubauer, H. A., Pham, D. H., Zebol, J. R., Moretti, P. A. B., Peterson, A. L., Leclercq, T. M., Chan, H., Powell, J. A., Pitman, M. R., Samuel, M. S. et al. (2016). An oncogenic role for sphingosine kinase 2. *Oncotarget* **7**, 64886-64899. doi:10.18632/oncotarget.11714

Neubauer, H. A., Tea, M. N., Zebol, J. R., Gliddon, B. L., Stefanidis, C., Moretti, P. A. B., Pitman, M. R., Costabile, M., Kular, J., Stringer, B. W. et al. (2019). Cytoplasmic dynein regulates the subcellular localization of sphingosine kinase 2 to elicit tumor-suppressive functions in glioblastoma. *Oncogene* **38**, 1151-1165. doi:10.1038/s41388-018-0504-9

Neumann-Giesen, C., Fernow, I., Amaddii, M. and Tikkanen, R. (2007). Role of EGF-induced tyrosine phosphorylation of reggie-1/flotillin-2 in cell spreading and signaling to the actin cytoskeleton. *J. Cell Sci.* **120**, 395-406. doi:10.1242/jcs.03336

Nguyen, M. K., Kim, C. Y., Kim, J. M., Park, B. O., Lee, S., Park, H. and Heo, W. D. (2016). Optogenetic oligomerization of Rab GTPases regulates intracellular membrane trafficking. *Nat. Chem. Biol.* **12**, 431-436. doi:10.1038/nchembio.2064

Paolino, M., Choidas, A., Wallner, S., Pranjic, B., Uribesalgo, I., Loeser, S., Jamieson, A. M., Langdon, W. Y., Ikeda, F., Fededa, J. P. et al. (2014). The E3 ligase Cbl-b and TAM receptors regulate cancer metastasis via natural killer cells. *Nature* **507**, 508-512. doi:10.1038/nature12998

Pardali, K. and Moustakas, A. (2007). Actions of TGF-β as tumor suppressor and pro-metastatic factor in human cancer. *Biochim. Biophys. Acta Rev. Cancer* **1775**, 21-62. doi:10.1016/j.bbcan.2006.06.004

Petitjean, A., Ruptier, C., Tribollet, V., Hautefeuille, A., Chardon, F., Cavard, C., Puisieux, A., Hainaut, P. and Caron De Fromentel, C. (2008). Properties of the six isoforms of p63: P53-like regulation in response to genotoxic stress and cross talk with δNp73. *Carcinogenesis* **29**, 273-281. doi:10.1093/carcin/bgm258

Planchon, D., Rios Morris, E., Genest, M., Comunale, F., Vacher, S., Bièche, I., Denisov, E. V., Tashireva, L. A., Perelmuter, V. M., Linder, S. et al. (2018). MT1-MMP targeting to endolysosomes is mediated by upregulation of flotillins. *J. Cell Sci.* **131**, jcs218925. doi:10.1242/jcs.218925

Puisieux, A., Brabletz, T. and Caramel, J. (2014). Oncogenic roles of EMT-inducing transcription factors. *Nat. Cell Biol.* **16**, 488-494. doi:10.1038/ncb2976

Pust, S., Klokk, T. I., Musa, N., Jenstad, M., Risberg, B., Erikstein, B., Tcatchoff, L., Liestøl, K., Danielsen, H. E., Van Deurs, B. et al. (2013). Flotillins as regulators of ErbB2 levels in breast cancer. *Oncogene* **32**, 3443-3451. doi:10.1038/onc.2012.357

Pyne, N. J., El Buri, A., Adams, D. R. and Pyne, S. (2018). Sphingosine 1-phosphate and cancer. *Adv. Biol. Regul.* **68**, 97-106. doi:10.1016/j.jbior.2017.09.006

Rao, L., Mak, V. C. Y., Zhou, Y., Zhang, D., Li, X., Fung, C. C. Y., Sharma, R., Gu, C., Lu, Y., Tipoe, G. L. et al. (2020). p85β regulates autophagic degradation of AXL to activate oncogenic signaling. *Nat. Commun.* **11**, 2291. doi:10.1038/s41467-020-16061-7

Riento, K., Zhang, Q., Clark, J., Begum, F., Stephens, E., Wakelam, M. J. and Nichols, B. J. (2018). Flotillin proteins recruit sphingosine to membranes and maintain cellular sphingosine-1-phosphate levels. *PLoS ONE* **13**, 1-18. doi:10.1371/journal.pone.0197401

Rohani, N., Parmeggiani, A., Winklbauer, R. and Fagotto, F. (2014). Variable combinations of specific Ephrin Ligand/Eph receptor pairs control embryonic tissue separation. *PLoS Biol.* **12**, e1001955. doi:10.1371/journal.pbio.1001955

Rossé, C., Lodillinsky, C., Fuhrmann, L., Nourieh, M., Monteiro, P., Irondelle, M., Lagoutte, E., Vacher, S., Waharte, F., Paul-Gilloteaux, P. et al. (2014). Control of MT1-MMP transport by atypical PKC during breast-cancer progression. *Proc. Natl. Acad. Sci. USA* **111**, E1872-E1879. doi:10.1073/pnas.1400749111

Schmid, S. L. (2017). Reciprocal regulation of signaling and endocytosis: implications for the evolving cancer cell. *J. Cell Biol.* **216**, 2623-2632. doi:10.1083/jcb.201705017

Shen, H., Giordano, F., Wu, Y., Chan, J., Zhu, C., Milosevic, I., Wu, X., Yao, K., Chen, B., Baumgart, T. et al. (2014). Coupling between endocytosis and sphingosine kinase 1 recruitment. *Nat. Cell Biol.* **16**, 652-662. doi:10.1038/ncb2987

Siow, D. and Wattenberg, B. (2011). The compartmentalization and translocation of the sphingosine kinases: Mechanisms and functions in cell signaling and sphingolipid metabolism. *Crit. Rev. Biochem. Mol. Biol.* **46**, 365-375. doi:10.3109/10409238.2011.580097

Subramanian, A., Tamayo, P., Mootha, V. K., Mukherjee, S., Ebert, B. L., Gillette, M. A., Paulovich, A., Pomeroy, S. L., Golub, T. R., Lander, E. S. et al. (2005).

Gene set enrichment analysis: A knowledge-based approach for interpreting genome-wide expression profiles. *Proc. Natl Acad. Sci. USA* **102**, 15545-15550. doi:10.1073/pnas.0506580102

Sung, B. H., Ketova, T., Hoshino, D., Zijlstra, A. and Weaver, A. M. (2015). Directional cell movement through tissues is controlled by exosome secretion. *Nat. Commun.* **6**, 7164. doi:10.1038/ncomms8164

Villaseñor, R., Kalaidzidis, Y. and Zerial, M. (2016). Signal processing by the endosomal system. *Curr. Opin. Cell Biol.* **39**, 53-60. doi:10.1016/j.ceb.2016.02.002

Wolff, A. C., Hammond, M. E. H., Schwartz, J. N., Hagerty, K. L., Allred, D. C., Cote, R. J., Dowsett, M., Fitzgibbons, P. L., Hanna, W. M., Langer, A. et al. (2007). American Society of Clinical Oncology/College of American Pathologists guideline recommendations for human epidermal growth factor receptor 2 testing in breast cancer. *J. Clin. Oncol.* **26**, 118-145. doi:10.1200/JCO.2006.09.2775

Xia, H., Ng, S. S., Jiang, S., Cheung, W. K. C., Sze, J., Bian, X.-W., Kung, H.- and Lin, M. C. (2010). miR-200a-mediated downregulation of ZEB2 and CTNNB1 differentially inhibits nasopharyngeal carcinoma cell growth, migration and invasion. *Biochem. Biophys. Res. Commun.* **391**, 535-541. doi:10.1016/j.bbrc.2009.11.093

Ye, X., Li, Y., Stawicki, S., Couto, S., Eastham-Anderson, J., Kallop, D., Weimer, R., Wu, Y. and Pei, L. (2010). An anti-Axl monoclonal antibody attenuates xenograft tumor growth and enhances the effect of multiple anticancer therapies. *Oncogene* **29**, 5254-5264. doi:10.1038/onc.2010.268

Yoh, K. E., Regunath, K., Guzman, A., Lee, S.-M., Pfister, N. T., Akanni, O., Kaufman, L. J., Prives, C. and Prywes, R. (2016). Repression of p63 and induction of EMT by mutant Ras in mammary epithelial cells. *Proc. Natl Acad. Sci. USA* **113**, E6107-E6116. doi:10.1073/pnas.1613417113

Zajac, O., Leclere, R., Nicolas, A., Meseure, D., Marchiò, C., Vincent-Salomon, A., Roman-Roman, S., Schoumacher, M. and Dubois, T. (2020). AXL controls directed migration of mesenchymal triple-negative breast cancer cells. *Cells* **9**, 247. doi:10.3390/cells9010247

Zhao, L., Lin, L., Pan, C., Shi, M., Liao, Y., Bin, J. and Liao, W. (2015). Flotillin-2 promotes nasopharyngeal carcinoma metastasis and is necessary for the epithelial-mesenchymal transition induced by transforming growth factor-β. *Oncotarget* **6**, 9781-9793. doi:10.18632/oncotarget.3382

Zhu, C., Wei, Y. and Wei, X. (2019). AXL receptor tyrosine kinase as a promising anti-cancer approach: Functions, molecular mechanisms and clinical applications. *Mol. Cancer* **18**, 153. doi:10.1186/s12943-019-1090-3

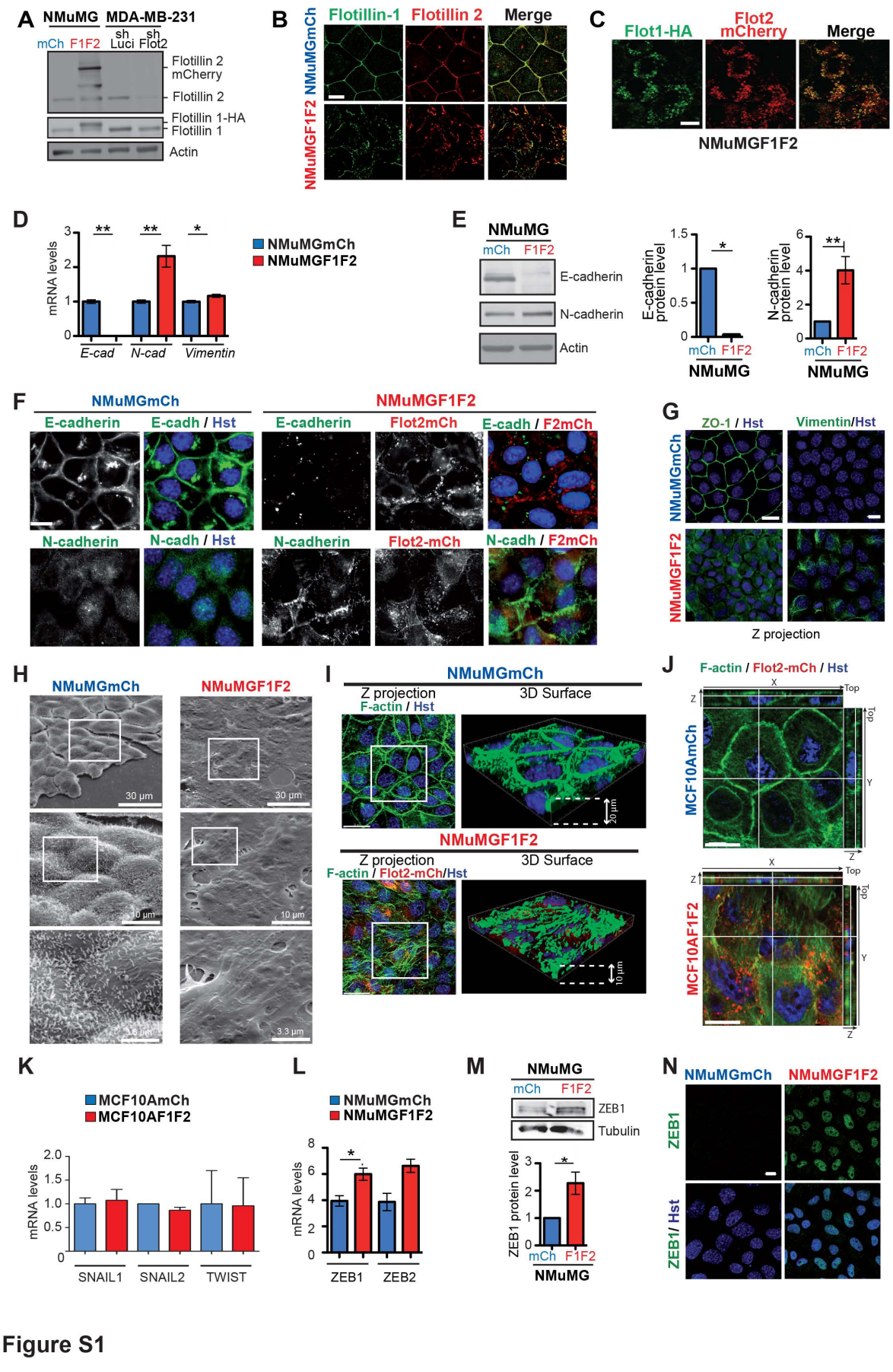

Figure S1

Fig. S1. Flotillin upregulation induces EMT in the NMuMG non-tumoral murine epithelial mammary cell line.

A) Lysates of NMuMG cells that stably express mCherry (NMuMGmCh) or both flotillin 1-HA and flotillin 2-mCherry (NMuMGF1F2) were analyzed by western blotting using antibodies against flotillin 1 and flotillin 2. In NMuMGF1F2 cells, flotillin levels were comparable to those detected in the invasive mammary tumor MDA-MB-231 cell line. Lysates from MDA-MB-231shFlot2 cells (generated using a shRNA against *FLOT2* to knockdown both flotillins [18]) also were analyzed. Actin was used as loading control.

B) Confocal images showing that endogenous flotillin 1 and 2 are localized at the plasma membrane in NMuMGmCh cells. In NMuMGF1F2 cells, they translocate to vesicular compartments, where they co-localize, as previously shown in MCF10AF1F2 and in MDA-MB-231 cells [18].
C) Confocal images showing the co-localization of flotillin 1-HA and flotillin 2-mCherry in intracellular vesicles in NMUMGF1F2 cells.
D) RT-qPCR analysis of the mRNA levels of E-cadherin, N-cadherin and vimentin in NMuMGmCh and NMuMGF1F2 cells. Histograms show the mean ± SEM of 4 independent experiments.
E, M) Western blots performed using NMuMGmCh and NMuMGF1F2 cell lysates to compare the amount of E- and N-cadherin (E), and ZEB1 (M). Histograms show the mean ± s.e.m. of at least 4 independent experiments.
F, G) Comparison of the distribution of endogenous E-, N-cadherin (F), and ZO-1 and vimentin (G) in NMuMGmCh and NMuMGF1F2 cells analyzed by immunofluorescence. Nuclei are stained with Hoechst (Hst, blue).

H) Scanning electron microscopy images of the monolayer formed by NMuMGmCh and NMuMGF1F2 cells.
I, J) F-actin cytoskeleton organization in NMuMGmCh and NMuMGF1F2 cells (I) and in MCF10AmCh and MCF10AF1F2 cells (J). Confluent cells were fixed and stained for F-actin (green) using Alexa488-Phalloidin. Nuclei (blue) were stained with Hoechst (flotillin2-mCherry signal is shown in the bottom panels). **(I)** Z-projection and 3D surface reconstruction of NMuMGmCh and NMuMGF1F2 cells was performed with 35 plans and 22 plans every 0.3.µm for NMuMGmCh and NMuMGF1F2 cells, respectively. **(J)** A stack of images was acquired by confocal microscopy (26 and 21 plans every 0.2 µm for MCF10AmCh and MCF10AF1F2 cells, respectively). The shown X-Y image corresponds to one single plane passing through the apical/top of the cell. X-Z and Y-Z projections along the indicated axes are shown.
K, L) *Characterization of the transcriptional repressors of E-cadherin expression*. RT-qPCR analysis of the mRNA levels of Snail1, Snail2, TWIST in MCF10AmCh and MCF10AF1F2 cells (K) and Zeb1 and 2 in NMuMGmCh and NMuMGF1F2 cells (L). Histograms show the mean ± s.e.m. of 4 independent experiments.
N) Confocal images of ZEB1 localization and nuclei stained with Hoechst (Hst, blue) in NMuMGmCh and NMuMGF1F2 cells.
Images in B, C, F, G, I, J and N are representative of cells observed in at least 3 independent experiments Scale bars: 10 µm.
*P<0.05 and **P<0.01 were determined with the Mann-Whitney test, two-tailed P-values (D, E, L, M).

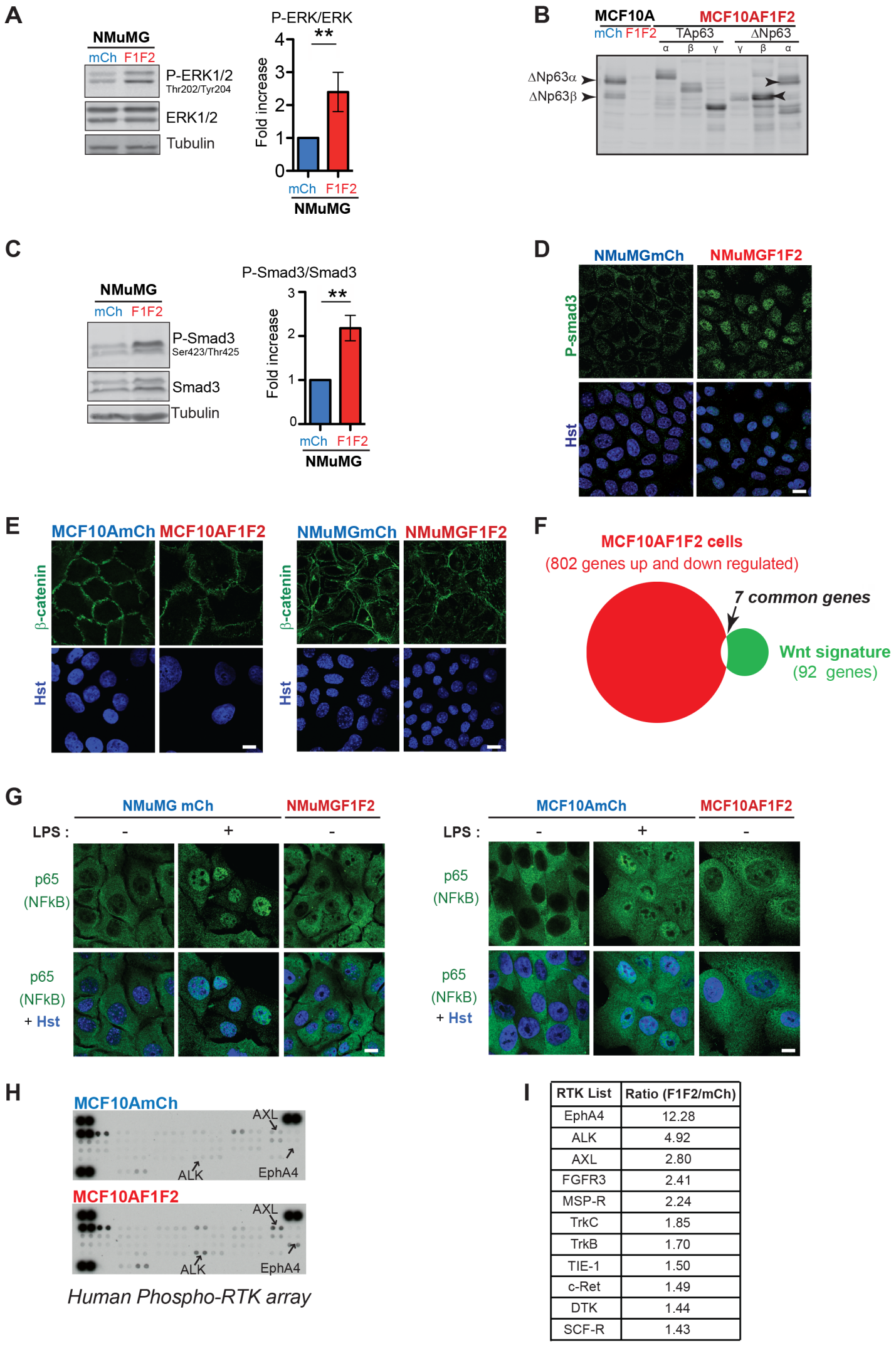

RTK List	Ratio (F1F2/mCh)
EphA4	12.28
ALK	4.92
AXL	2.80
FGFR3	2.41
MSP-R	2.24
TrkC	1.85
TrkB	1.70
TIE-1	1.50
c-Ret	1.49
DTK	1.44
SCF-R	1.43

Figure S2

Fig. S2. Determination of the p63 isoforms expressed in MCF10AmCh cells and downregulated in MCF10AF1F2 cells. Identification of non-activated signaling pathways downstream of flotillin upregulation in mammary epithelial cells. Screening for activated RTKs upon flotillin upregulation.

A, C) Cell lysates from NMuMGmCh and NMuMGF1F2 cells were analyzed by western blotting to evaluate the phosphorylation status of ERK1/2 (B) and SMAD3 (C). Histograms (mean ± s.e.m. of 4 independent experiments) show the quantification of the phosphorylation signal normalized to the total amount of each protein.

B) *Characterization of the p63 isoforms expressed in MCF10AmCh and MCF10AF1F2 cells*. Western blot analysis of the p63 isoforms in lysates from MCF10AmCh, MCF10AF1F2 and MCF10AF1F2 cells transfected with different non-tagged p63 isoforms (TAp63γ ,β ,α or ΔNp63γ ,β ,α) using an antibody against all p63 isoforms. ΔNp63α and to a lesser extent ΔNp63β are the two mains isoforms expressed in MCF10A cells. The expression of ΔNp63α and of ΔNp63β was abolished in MCF10AF1F2 cells (as shown in fig. 2G).

D) NMuMGmCh and NMuMGF1F2 cells were labeled with an antibody against SMAD3 phosphorylated on S423/425 and with Hoechst (Hst).

E, F, G) *The oncogenic NF-kB and WNT canonical signaling pathways are not activated following flotillin upregulation in MCF10A and NMuMG cells*. **E)** β-catenin distribution, analyzed by immunofluorescence is similar in MCF10AmCh and MCF10AF1F2 cells and in NMuMGmCh and NMuMGF1F2 cells, and no nuclear staining was detected, indicating that the WNT canonical pathway is not activated. Nuclei are stained with Hoechst (Hst). **F)** Venn diagrams illustrating the small overlap between the 802 differentially expressed genes identified by RNA-seq in MCF10AF1F2 cells versus MCF10AmCh cells and the 92 differentially expressed genes of an established WNT signature (http://web.stanford.edu/group/nusselab/cgi-bin/wnt/target_genes). Only 7/92 genes overlapped. **G)** Cellular distribution of the NF-kB p65 subunit, analyzed by immunofluorescence, in MCF10AmCh and MCF10AF1F2 cells and in NMuMGmCh and NMuMGF1F2 cells. In all cases, NF-kB p65 was excluded from the nucleus, indicating that the NF-kB pathway is not activated upon flotillin upregulation. As positive control, MCF10AmCh cells and NMuMGmCh cells were stimulated with lipopolysaccharide (LPS; 1µg/ml, 1h) to induce NF-kB p65 translocation to the nucleus.

H) Flotillin upregulation increases the phosphorylation level of several RTKs. Human phospho-Receptor Tyrosine kinase arrays were incubated with 200 µg of MCF10AmCh or MCF10AF1F2 cell lysates (cultured in the presence of serum) and processed as described by the manufacturer. One array example is shown.

I) List of the 11 RTKs with the highest increase in phosphorylation in MCF10AF1F2 compared with MCF10AmCh cells (data from 2 independent experiments).

Images in D, E, G are representative of at least 3 independent experiments. Scale bars: 10 µm.

**P<0.01 was determined with the Mann-Whitney test, two-tailed P-values (A, C).

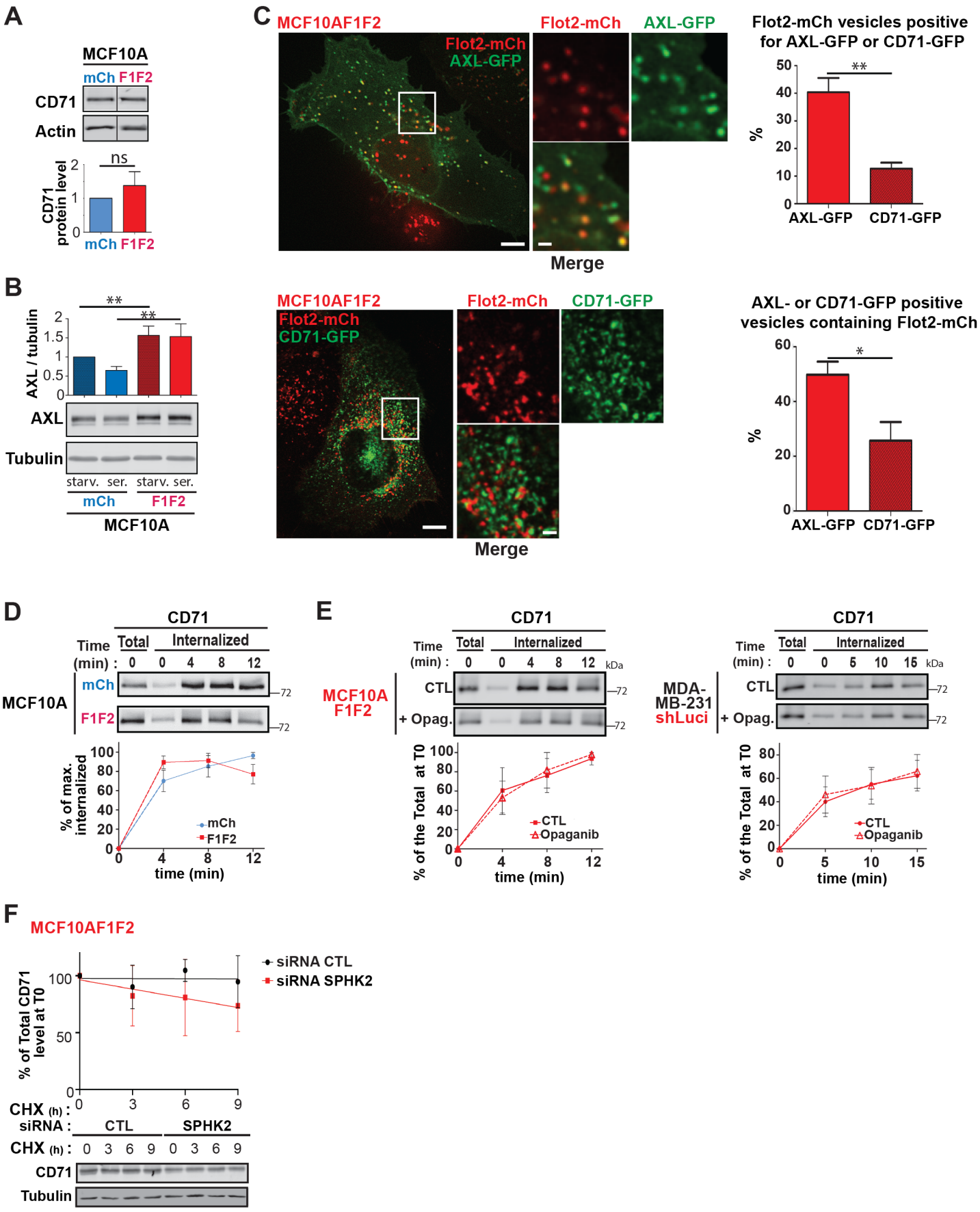

Figure S3

Fig. S3. The transferrin receptor CD71 is not a cargo of the UFIT pathway.

A) *Flotillin upregulation does not affect CD71 level.* Cell lysates of MCF10AmCh and MCF10AF1F2 cells were probed by western blotting with antibodies against CD71 and actin. Results are expressed as fold-change compared with MCF10AmCh cells and are the mean ± s.e.m. of 4 independent experiments.
B) *Flotillin upregulation promotes AXL protein level increase independently of serum stimulation.* Lysates from MCF10AmCh and MCF10AF1F2 cells, serum-starved for 16h (starv.) or maintained in the presence of serum (ser.), were probed by western blotting with antibodies against AXL and tubulin. Results are expressed as fold-change compared with MCF10AmCh cells in serum-starved conditions and are the mean ± s.e.m. of 5 independent experiments.
C) *The transferrin receptor CD71 poorly localizes in flotillin-positive late endosomes compared with AXL.* Live MCF10AF1F2 cells that express CD71-GFP or AXL-GFP were imaged by spinning disk confocal microscopy. Images are representative of several cells in 3 independent experiments. Scale bars: 10 µm in the main image and 2 µm in the magnified images from the boxed area. The histograms show the percentage of Flotillin2-mCherry (Flot2-mCh)-positive vesicles containing AXL-GFP or CD71-GFP (upper histogram), and the percentage of AXL-GFP- or CD71-GFP-positive vesicles containing Flot2-mCh (lower histogram). Results are the mean ± s.e.m. (n=690 Flot2-mCh-positive vesicles and n=746 AXL-GFP labeled vesicles in 21 AXL-GFP-expressing MCF10AF1F2 cells ; and n=1511 Flot2-mCh-positive vesicles and n=1207 AXL-GFP labeled vesicles in 20 CD71-GFP-expressing MCF10AF1F2 cells).
D) *Flotillin upregulation does not affect the transferrin receptor endocytosis.* Kinetics of CD71 (transferrin receptor) internalization in MCF10AmCh and MCF10AF1F2 cells analyzed in the same experiments presented in figure 4G. Surface proteins were labeled with biotin at 4°C and cells were incubated at 37°C for the indicated times to allow endocytosis. CD71 presence in the internalized biotinylated fraction was analyzed by western blotting using relevant antibodies, and quantified as the percentage of the maximum level of internalized protein. Results are expressed as the mean ± s.e.m. of 4 independent experiments. The CD71 internalization rates were not significantly different between cell lines at 4, 8 and 12 min.
E) *SPHK2 inhibition has no impact on CD71 internalization in flotillin-upregulated cells.* Kinetics of CD71 internalization in MCF10AF1F2 and in MDA-MB-231shLuci cells untreated (CTL) or pre-treated with Opaganib (50µM, 4h), as in figure 6G and H. Surface proteins were labeled with biotin at 4°C, and cells were incubated at 37°C for the indicated times to allow endocytosis. Opaganib was maintained throughout the experiments. CD71 presence in the internalized biotinylated fraction was probed by western blotting using relevant antibodies. Results are expressed as the percentage of the maximum level of CD71 surface level at T0 and are the mean ± SEM of 4 independent experiments. CD71 internalization rates were not significantly different between control and Opaganib-treated cells in both cell lines. Simple linear regression analysis with GraphPad Prism did not detect any difference between the curves (p=0.77 for MCF10AF1F2 cell and P=0.96 for MDA-MB-231 cells)
F) In contrast to AXL (fig. 6G), *CD71 internalization rate is not modified by SPHK2 knock-down*. MCF10AF1F2 cells were transfected with siRNAs against luciferase (CTL) or SPHK2 for 72 hours, incubated with cycloheximide (CHX, 100µg/ml), and the cell lysates were collected at the indicated time points. CD71 levels were assessed by western blot analysis. The graph shows the level of CD71 expressed as the percentage of the total level at T0. The results are the mean ± s.e.m. of 4 independent experiments. Simple linear regression analysis with GraphPad Prism did not detect any was established under each condition. According to Graph Pad Prism, the slopes of the curves obtained for each condition were not considered as significantly different between conditions (P=0.1236).
*P<0.05 and **P<0.01 were determined with the Mann-Whitney test, two-tailed P-values (A, B, C)

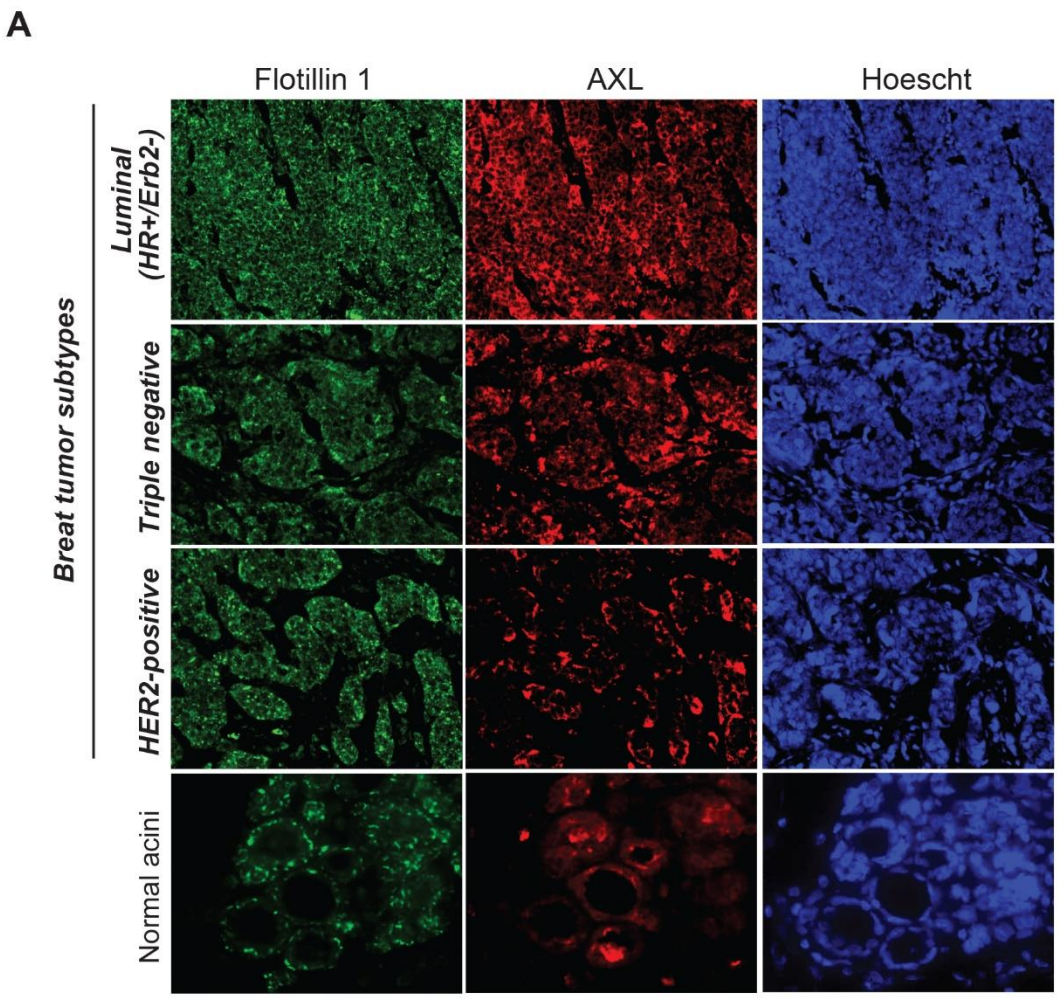

Figure S4

Fig. S4. ***Flotillin 1 and AXL are co-expressed in invasive breast tumor cells.***

A) Immunofluorescence analysis of flotillin 1 and AXL in invasive breast tumor tissue sections in one patient sample for each breast tumor subtype and in non-tumoral breast tissue. Nuclei were stained with DAPI. Scale bar: 10µm.

B) Immunofluorescence analysis of flotillin 1 and AXL expression in 6 non-tumoral breast tissue samples and 43 breast tumor samples (Luminal n= 17, Triple Negative n =15, $HER2^{+}$ =11). Co-expression was calculated in the different subtypes with the Vectra 3.0 Automated Quantitative Pathology Imaging System. Results show the mean ± s.e.m.

C) High magnification immunofluorescence images of flotillin 1 and AXL expression in a luminal B invasive breast tumor section. Nuclei were stained with Hoechst. Arrows indicate flotillin 1 and AXL colocalization in intracellular vesicles. Scale bar: 10µm.

*P<0.05 and **P<0.01 were determined with the Mann-Whitney test, two-tailed P-values (B)

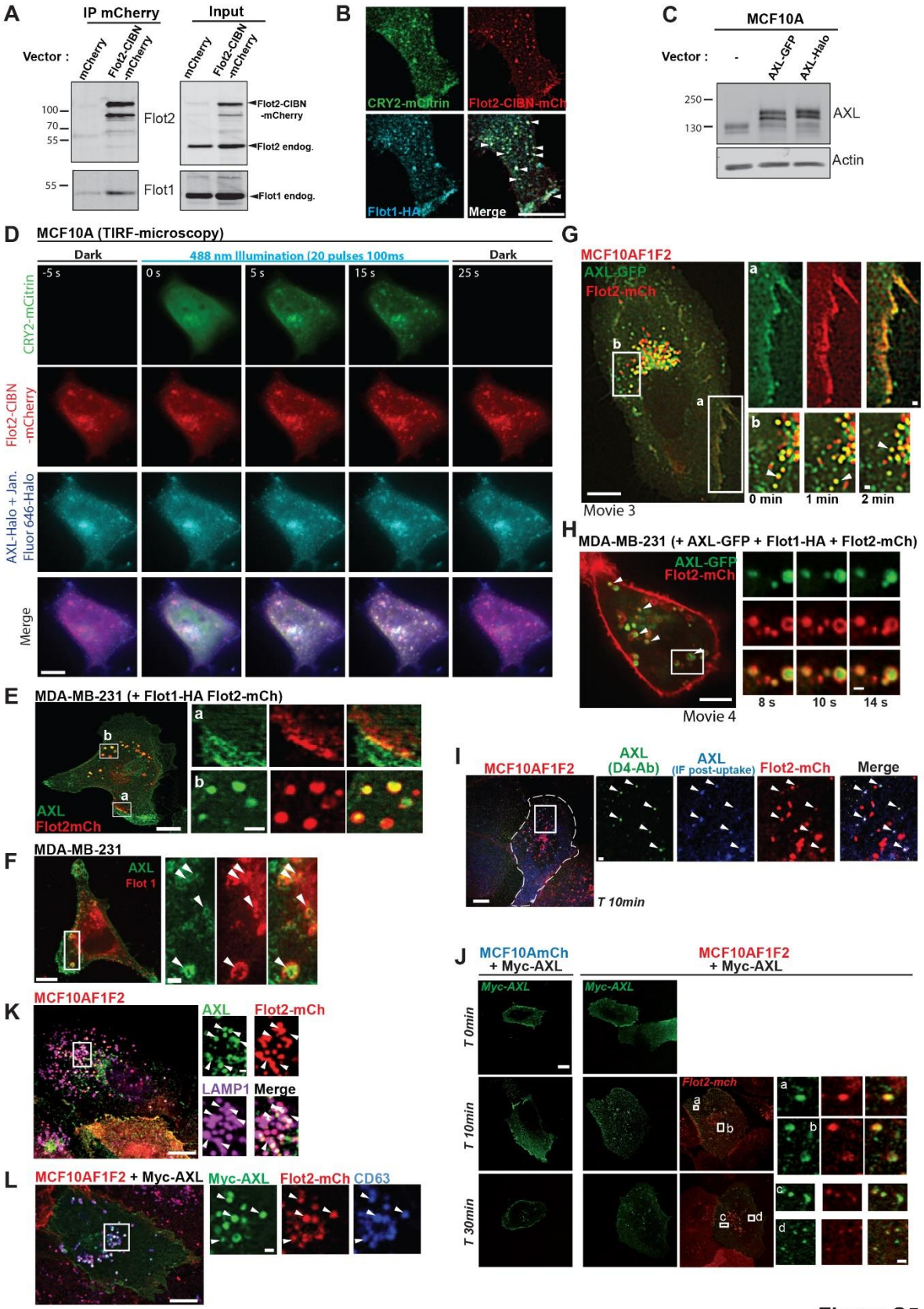
A
IP mCherry
Input
Vector :
mCherry
Flot2-CIBN -mCherry
100
70
55
Flot2
Flot1
Flot2-CIBN -mCherry
Flot2 endog.
Flot1 endog.
B
CRY2-mCitrin
Flot2-CIBN-mCh
Flot1-HA
Merge
C
MCF10A
Vector :
-
AXL-GFP
AXL-Halo
250
130
AXL
Actin
D
MCF10A (TIRF-microscopy)
Dark
488 nm Illumination (20 pulses 100ms
Dark
-5 s
0 s
5 s
15 s
25 s
CRY2-mCitrin
Flot2-CIBN -mCherry
AXL-Halo + Jan. Fluor 646-Halo
Merge
E
MDA-MB-231 (+ Flot1-HA Flot2-mCh)
AXL
Flot2mCh
F
MDA-MB-231
AXL
Flot 1
G
MCF10AF1F2
AXL-GFP
Flot2-mCh
Movie 3
0 min
1 min
2 min
H
MDA-MB-231 (+ AXL-GFP + Flot1-HA + Flot2-mCh)
AXL-GFP
Flot2-mCh
Movie 4
8 s
10 s
14 s
I
MCF10AF1F2
AXL (D4-Ab)
AXL (IF post-uptake)
Flot2-mCh
Merge
T 10min
J
MCF10AmCh + Myc-AXL
MCF10AF1F2 + Myc-AXL
Myc-AXL
Flot2-mch
T 0min
T 10min
T 30min
K
MCF10AF1F2
AXL
Flot2-mCh
LAMP1
Merge
L
MCF10AF1F2 + Myc-AXL
Myc-AXL
Flot2-mCh
CD63

Figure S5

Fig. S5. Co-distribution of AXL and flotillins at the plasma membrane and in late endosomes.

A) *Flotillin2-CIBN-mCherry interacts with flotillin 1.* Immunoprecipitations using an antibody against mCherry (mCherry trap) and lysates from MCF10A cells that express mCherry alone or flotillin 2-CIBN-mCherry. Immunoprecipitates were then analyzed with antibodies to detect flotillin 1 and 2. Flotillin 1 was co-immunoprecipitated only in lysates from cells that express flotillin 2-CIBN-mCherry, but not mCherry alone. Results are representative of 3 independent experiments.

B) *Light-induced flotillin 2-CIBN-mCherry microdomains contain flotillin 1.* MCF10A cells that co-express flotillin 2-CIBN-mCherry, flotillin 1-HA and CRY2-mCitrin were illuminated at 488 nm for 1 min, fixed, incubated with an anti-HA antibody and imaged by confocal microscopy. CRY2-mCitrin patches containing flotillin 2-CIBN-mCherry (white arrows) also exhibit flotillin 1-HA signal. Results are representative of 3 independent experiments.

C) *Characterization of the AXL-GFP and AXL-Halo constructs.* MCF10A cells were transfected with empty vector (-) or plasmids encoding AXL-GFP or AXL-Halo. Expression of the proteins of the expected size (138+28=166 kDa for AXL-GFP) and (138+28=171 kDa for AXL-Halo) is shown. A doublet was observed for each tagged protein like for endogenous AXL.

D) *Still images from a TIRF-microscopy video of one MCF10A cell that co-expresses CRY2-mCitrin, flotillin 2-CIBN-mCherry and AXL-Halo labeled with Halo-Tag-Janelia Fluor 646*. The cell was imaged before, during, and after 488 nm illumination (22 pulses of 100 ms each every second). Merged signals in the same cell 15 s after starting the 488 nm illumination is shown in Fig. 4B.

E, F) *Distribution and colocalization of endogenous AXL with flotillins in MDA-MB-231 cells analyzed by confocal microscopy after immunofluorescence staining*. (E) The cell expresses flotillin 2-mCherry. Higher magnification images of the two boxed regions show AXL colocalization with flotillin 2-mCherry at the plasma membrane (a) and in intracellular vesicles (b). (F) Endogenous flotillin 1 was detected by immunocytochemistry. The boxed region shows AXL colocalization with flotillin 1 in intracellular vesicles.

G) *Co-trafficking of AXL and flotillins in MCF10AF1F2 cells.* Still images of a representative time-lapse series (movie 3) of a MCF10AF1F2 cell that expresses AXL-GFP to illustrate the co-localization of AXL-GFP and flotillin 2-mCherry at the plasma membrane (box a), and in intracellular vesicles (box b) and their co-trafficking. The white arrow allows following one vesicle over time.

H) *Co-trafficking of AXL and flotillins in MDA-MB-231 cells.* MDA-MB-231 cells were transfected with AXL-GFP, flotillin 2-mCherry and flotillin 1-HA-encoding plasmids. Live cells were imaged by spinning disk confocal microscopy. Three images from the boxed region, acquired at different times, show the the co-trafficking of AXL-GFP and flotillin 2-mCherry in intracellular vesicles (movie 4).

I) An MCF10AF1F2 cell (the same cell as shown in Fig. 4F) was incubated with the anti-AXL D4 antibody (against AXL extracellular domain) at 4°C followed by incubation at 37°C for 10 min to allow AXL internalization. After fixation and permeabilization, internalized AXL was labeled (green) with a FITC-conjugated secondary antibody against the D4 antibody. Immunofluorescence staining of AXL (blue) was also performed using an antibody against AXL cytoplasmic domain and an Alexa-633 conjugated secondary antibody. Arrowheads indicate flotillin 2-mCherry-positive vesicles in which AXL is internalized (green).

J) MCF10AmCh and MCF10AF1F2 cells that express Myc-tagged AXL were incubated with an anti-Myc antibody at 4°C, followed by incubation at 37°C for the indicated times. Myc-AXL distribution was analyzed by immunocytochemistry using an Alexa488-conjugated secondary antibody.

K) In MCF10AF1F2 cells, endogenous AXL is localized in flotillin 2-mCherry vesicles positive for the endolysosomal marker LAMP1 (confocal microscopy image).

L) Myc-tagged AXL expressed in MCF10AF1F2 cells is localized in flotillin 2-mCherry vesicles positive for the late endosomal marker CD63 (Confocal microscopy image after immunofluorescence). Images shown in B, D - K are representative of 3 to 5 independent experiments. In E, F, G, H, I, J, K and L scale bars = 10 µm in the main images and = 2 µm in the magnified images from the insets.

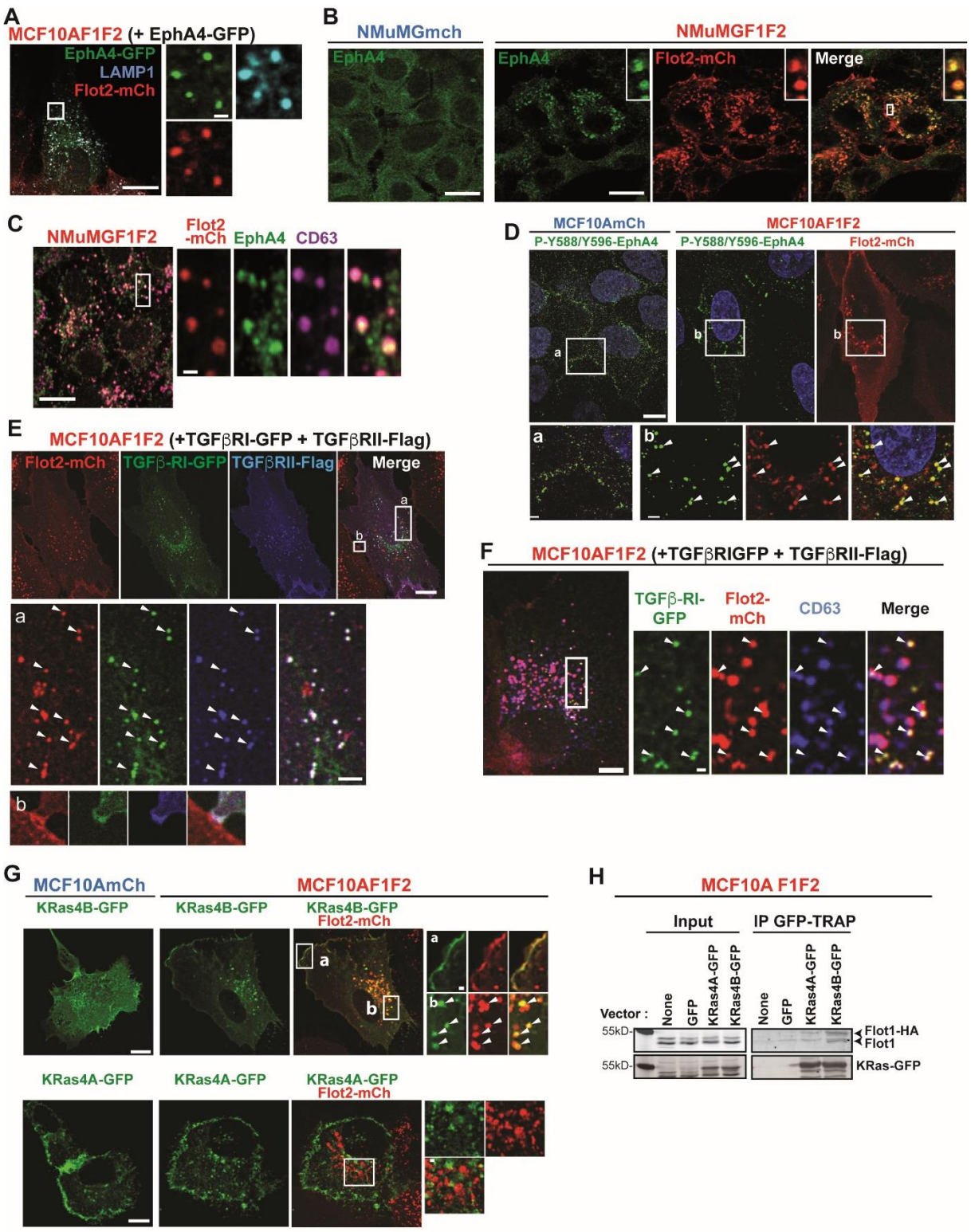

Figure S6

Fig. S6. The RTK EphA4, the TGFη receptors, and Kras4B are located in flotillin-positive late endosomes.

A). Confocal microscopy image of one MCF10AF1F2 cell that expresses EphA4-GFP and stained for LAMP1, showing flotillin 2/EphA4 co-localization in LAMP-1-positive vesicles.

B, C) Immunofluorescence analysis of NMuMGmCh and NMuMGF1F2 cells to detect endogenous EphA4. In NMuMGF1F2 cells, EphA4 relocates in intracellular vesicles, many of which are flotillin 2-mCherry- and CD63-positive (C).

D) MCF10AmCh and MCF10AF1F2 cells were analyzed by immunofluorescence using an antibody against EphA4 phosphorylated on Y588/Y596. In MCF10AmCh cells the signal is at cell-cell contacts (magnified image from the boxed area (a)), whereas it is concentrated in intracellular vesicles in MCF10AF1F2 cells where it co-localizes with flotillin 2-mCherry (magnified images from boxed areas (b)).

E) MCF10AF1F2 cells that co-express the TGFβ-RI (GFP-tagged) and TGFβ-RII (Flag-tagged) subunits were analyzed by immunofluorescence using an anti-Flag antibody and imaged by confocal microscopy. Both subunits are concomitantly found at the plasma membrane and in intracellular vesicles (white arrows) where they colocalize with flotillin 2-mCherry.

F) MCF10AF1F2 cells that co-express TGFβ-RI-GFP and TGFβ-RII-Flag were stained for CD63 and imaged by confocal microscopy. White arrows in the magnified images of the boxed area indicate co-localization of TGFβ-RI-GFP, CD63 and flotillin 2-mCherry in intracellular vesicles. Scale bars= 10µm in the main images and =1 µm in the magnified regions.

G) *Flotillin upregulation specifically relocates K-Ras4B to flotillin-positive endosomes.* Confocal images of MCF10AmCh and MCF10AF1F2 cells that express K-Ras4A-GFP or K-Ras4B-GFP. Unlike K-Ras4A-GFP (lower panels), K-Ras4B-GFP (upper panels) co-localizes with flotillins and its distribution is modified in MCF10AF1F2 cells compared with MCF10AmCh cells (upper panel). K-Ras4B-GFP is mainly present at the plasma membrane in MCF10AmCh cells. Conversely, in MCF10AF1F2 cells, it remains visible at the plasma membrane where it co-localizes with flotillin 2-mCherry (magnified images from the boxed region (a)), but it is also strongly recruited to flotillin 2-mCherry-positive vesicles and co-trafficked with flotillin 2 (magnified images of the boxed region (b)). In A, B, C, D, E, G, scale bars = 10 µm in the main images and = 2 µm in the magnified images from insets. In panels A-G, images are representative of several cells observed in 3 independent experiments.

H) *K-Ras4B forms a complex with flotillin 1.* Lysates from MCF10AF1F2 cells that express GFP alone, K-Ras4A-GFP, or K-Ras4B-GFP were immunoprecipitated with GFP-TRAP. Immunoprecipitates were probed by western blotting using anti-flotillin 1 and anti-pan-Ras antibodies. Both K-Ras isoforms are similarly expressed and immunoprecipitated. The signal for flotillin 1-HA and flotillin 1 in precipitates from K-Ras4B-GFP-expressing cells is clearly higher than the signal observed in precipitates from K-Ras4A-GFP-expressing cells that is similar to the background signal found in precipitates from GFP-expressing cells. Results are representative of 3 independent experiments.

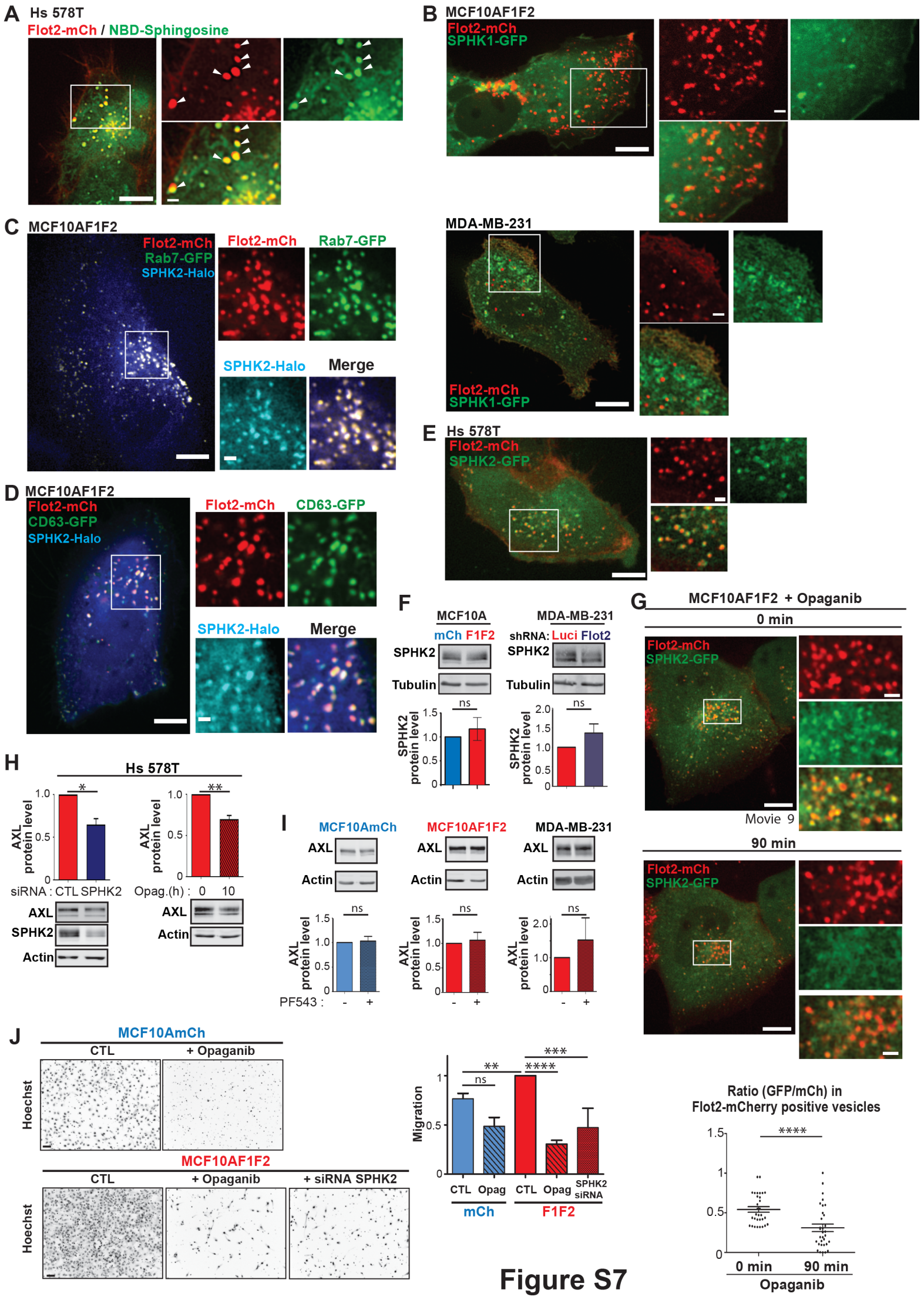

Figure S7

Fig. S7. Sphingosine, SPHK1 and 2 localization and effect of SPHK inhibitors.

A) *NBD-sphingosine accumulates in flotillin-positive late endosomes***.** Live Hs 578T cells that express flotillin2-mCherry were incubated with NBD-sphingosine. A still image acquired 5 min after the addition of the fluorescent lipid is shown. White arrows show flotillin 2-mCherry-positive vesicles where NBD-sphingosine accumulates.

B) *SPHK1 is barely detected in flotillin-positive endosomes.* Live MCF10AF1F2 cells that express SPHK1-GFP (left), and MDA-MB-231 cells that co-express flotillin 1-mCherry and SPHK1-GFP (right) were imaged by spinning disk confocal microscopy (see quantification in fig. 5D).

C, D) *SPHK2 colocalizes with flotillins in Rab7- and CD63-positive vesicles.* Still images of live MCF10AF1F2 cells that express SPHK2-Halo labeled with Halo-tag-Janelia Fluor 646 and Rab7-GFP (C), or CD63-GFP (D) imaged by spinning disk confocal microscopy. Images are representative of 3 independent experiments.

E) *SPHK2 is enriched in flotillin-positive late endosomes in Hs 578T cells.* Live Hs 578T cells that co-express flotillin 2-mCherry and SPHK2-GFP were imaged by spinning disk confocal microscopy. Still images are shown

F) *Flotillin level does not modulate SPHK2 protein expression.* SPHK2 and tubulin were assessed in whole cell extracts from MCF10AmCh, MCF10AF1F2, MDA-MB-231shLuci, and MDA-MB-231shFlot2 cells by western blotting using specific antibodies. The histograms show SPHK2 level (normalized to tubulin) expressed as fold-change compared with MCF10AmCh or MDA-MB-231shLuci cells, and data are the mean ± s.e.m. of 4 independent experiments.

G) *Opaganib induces the delocalization of SPHK2 from flotillin-positive vesicles.* Live MCF10AF1F2 cells that express SPHK2-GFP were imaged right after incubation with opaganib by spinning disk confocal microscopy every 15 min. The SPHK2-GFP signal associated with flotillin 2-mCherry positive vesicles was clearly decreased after 90 min of incubation. The histogram (mean ± s.e.m.) shows the GFP/mCherry signal ratio in flotillin 2-mCherry-positive vesicles at 0 and after 90 min of opaganib incubation (31 vesicles at T0 and 32 vesicles at T90 from 3 independent cells).

In panels A, B, C, D, E and G, scale bars = 10 µm in the main images, and to = 2 µm in the magnified images from the boxed area.

H) *SPHK2-inhibition decreases AXL in Hs 578T cells.* (Left) Hs 578T cells were transfected with siRNAs against luciferase (CTL) or SPHK2. In whole lysates, siRNA efficacy was tested by western blotting with antibodies against SPHK2, AXL and actin. (Right) Hs 578T cells were incubated with opaganib (50 µM, 10 h). AXL and actin were analyzed by western blotting of whole cell lysates. The histograms show the level of AXL normalized to the actin signal, expressed as fold-change compared with the control condition and are the mean ± s.e.m. of 4 independent experiments.

I) *SPHK1 inhibition does not influence AXL level in cells in which flotillins are upregulated.* MCF10AmCh, MCF10AF1F2 and MDA-MB-231 cells were incubated with the selective SPHK1 inhibitor PF543 (10 µM, 24h). AXL and actin levels were measured by western blotting in cell lysates. The histograms show AXL level, expressed as fold-change compared with the control condition (no PF543), and data are the mean ± s.e.m. of 4 independent experiments.

J) *Boyden chamber migration assay.* MCF10AmCh and MCF10AF1F2 cells were seeded in the top of Boyden chamber inserts in serum-free medium, and serum-containing medium, acting as chemoattractant, was placed in the bottom well. When indicated, opaganib (50 µM) was added in the upper and lower chambers, or MCF10AF1F2 were transfected with siRNAs against SPHK2 for 48h prior to seeding. Representative inverted-microscopy images of Hoechst-stained nuclei of cells that migrated through the pores. The histogram shows the number of cells that migrated compared with untreated MCF10AF1F2 cells, and data are the mean ± s.e.m. of at least 4 independent experiments. Scale bar: 50µm.

*P<0.05, **P<0.01 , ***P<0.001 and ****P<0.0001 were determined with the Mann-Whitney test, two-tailed P-values (F,G,H,I and J)

Table S1. The differential gene expression analysis was processed on three replicates per condition to compare the levels of the transcripts between MCF10AmCh and MCF10AF1F2 cells Confrontation of the results obtained from the Deseq2 and Tuxedo analyses

Click here to download Table S1

Table S2. List of the enriched GO terms and the enriched pathways obtained from the analysis of the 802 differentially expressed genes between MCF10mCh and MCF10AF1F2 using three distinct bioinfomatic tools (KEGG, DAVID, and Genomatix)

KEGG Enrichr pathways	KEGG David	Genomatix
Cell adhesion molecules (CAMs)_Homo sapiens_hsa04514	hsa04151:PI3K-Akt signaling pathway	Extracellular matrix organization
PI3K-Akt signaling pathway_Homo sapiens_hsa04151	hsa04514:Cell adhesion molecules (CAMs)	Cell-Cell communication
Proteoglycans in cancer_Homo sapiens_hsa05205	hsa05205:Proteoglycans in cancer	Cell junction organization
Hematopoietic cell lineage_Homo sapiens_hsa04640	hsa04640:Hematopoietic cell lineage	a6b1 and a6b4 Integrin signaling
Pathways in cancer_Homo sapiens_hsa05200	hsa05200:Pathways in cancer	Beta5 beta6 beta7 and beta8 integrin cell surface interactions
Rap1 signaling pathway_Homo sapiens_hsa04015	hsa04015:Rap1 signaling pathway	amb2 Integrin signaling
Malaria_Homo sapiens_hsa05144	hsa05144:Malaria	Alpha6Beta4Integrin
Inflammatory bowel disease (IBD)_Homo sapiens_hsa05321	hsa04060:Cytokine-cytokine receptor interaction	EGFR1
Insulin resistance_Homo sapiens_hsa04931	hsa05321:Inflammatory bowel disease (IBD)	Syndecan-2-mediated signaling events
AGE-RAGE signaling pathway in diabetic complications_Homo sapiens_hsa04933	hsa04931:Insulin resistance	Direct p53 effectors
Ras signaling pathway_Homo sapiens_hsa04014	hsa04014:Ras signaling pathway	FGF signaling pathway
Cytokine-cytokine receptor interaction_Homo sapiens_hsa04060	hsa04512:ECM-receptor interaction	Signaling by MST1
Prion diseases_Homo sapiens_hsa05020	hsa05323:Rheumatoid arthritis	Transport of small molecules
	hsa05230:Central carbon metabolism in cancer	Visual phototransduction
	hsa00601:Glycosphingolipid biosynthesis - lacto and neolacto series	Cytokine Signaling in Immune system
	hsa04750:Inflammatory mediator regulation of TRP channels	SHP2 signaling
	hsa04610:Complement and coagulation cascades	Beta2 integrin cell surface interactions
	hsa05412:Arrhythmogenic right ventricular cardiomyopathy (ARVC)	Angiopoietin receptor Tie2-mediated signaling
	hsa05218:Melanoma	Hemostasis
	hsa05202:Transcriptional misregulation in cancer	Validated transcriptional targets of TAp63 isoforms
	hsa04064:NF-kappa B signaling pathway	ion channels and their functional role in vascular endothelium
	hsa04144:Endocytosis	Signaling by Retinoic Acid
		Beta3 integrin cell surface interactions
		Blood coagulation
		Beta1 integrin cell surface interactions
		Plasminogen activating cascade
		Validated transcriptional targets of deltaNp63 isoforms
		ATF-2 transcription factor network
		Endogenous TLR signaling
		IL27-mediated signaling events
		Validated transcriptional targets of AP1 family members Fra1 and Fra2
		signal transduction through il1r
		inhibition of matrix metalloproteinases
		IL-7
		PI3K/AKT Signaling in Cancer

David version 6.8
https://david.ncifcrf.gov/home.jsp
DAVID users may publish or otherwise publicly disclose the results of using DAVID. Please acknowledge DAVID in your publications by citing the following two references:
Huang DW, Sherman BT, Lempicki RA. Systematic and integrative analysis of large gene lists using DAVID Bioinformatics Resources. Nature Protoc. 2009;4(1):44-57.
Huang DW, Sherman BT, Lempicki RA. Bioinformatics enrichment tools: paths toward the comprehensive functional analysis of large gene lists. Nucleic Acids Res. 2009;37(1):1-13.

KEGG Pathway DataBase
https://www.kegg.jp/kegg/pathway.html
Please cite the following article(s) when using KEGG.
Kanehisa, Furumichi, M., Tanabe, M., Sato, Y., and Morishima, K.; KEGG: new perspectives on genomes, pathways, diseases and drugs. Nucleic Acids Res. 45, D353-D361 (2017).
Kanehisa, M., Sato, Y., Kawashima, M., Furumichi, M., and Tanabe, M.; KEGG as a reference resource for gene and protein annotation. Nucleic Acids Res. 44, D457-D462 (2016).
Kanehisa, M. and Goto, S.; KEGG: Kyoto Encyclopedia of Genes and Genomes. Nucleic Acids Res. 28, 27-30 (2000).

Genomatix
http://www.genomatix.de/
Genomatix Software suite version 3.10

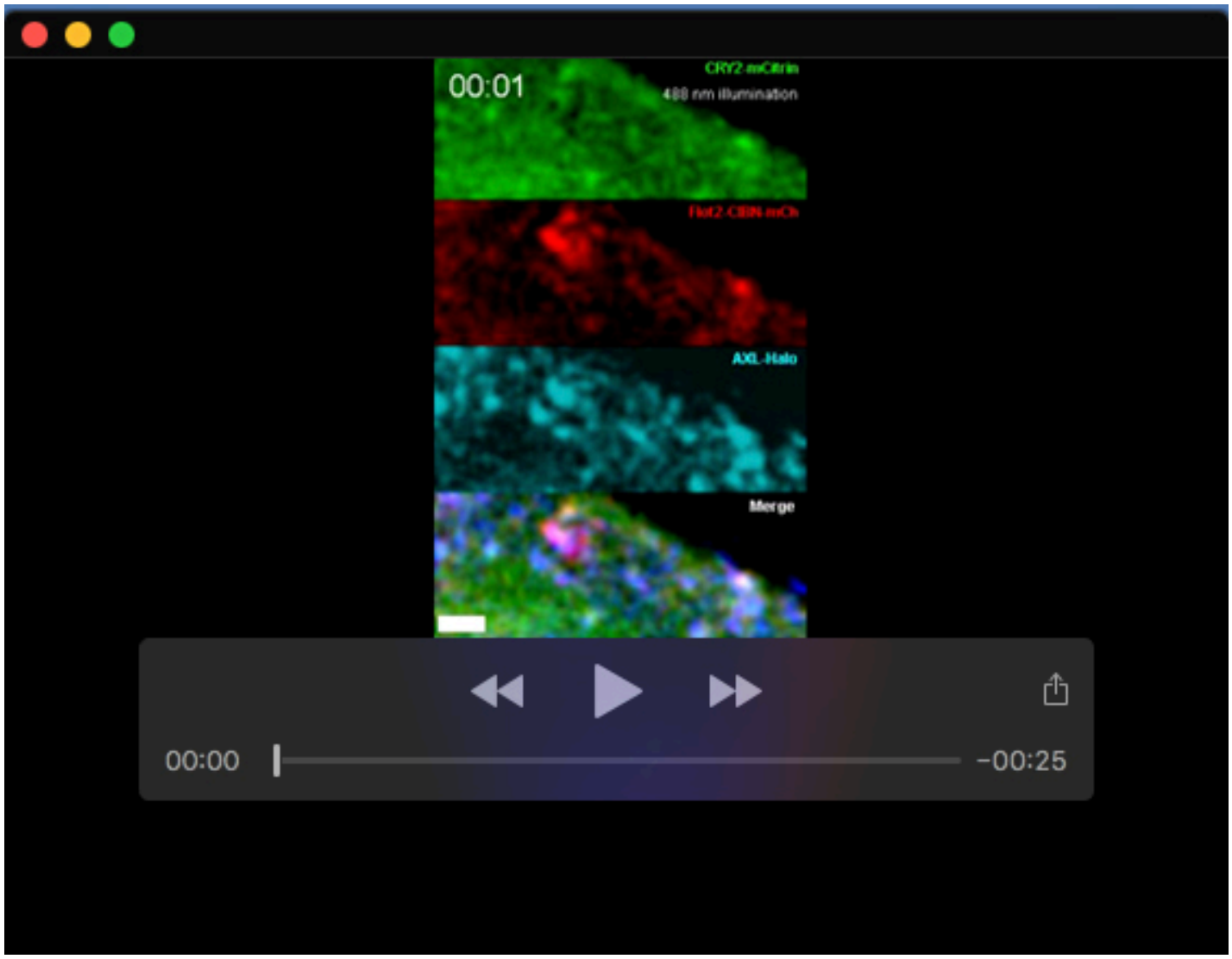

Movie 1. *Flotillin oligomerization induced by a CRY2-CIBN-based optogenetic approach promotes AXL co-clustering*. Movie of the boxed area from figure 4B. MCF10A cells that co-express CRY2-mCitrin (green), flotillin 2-CIBN-mCherry (red) and AXL-Halo (blue) labeled with Halo-Tag-Janelia Fluor 646 were imaged by TIRF microscopy. First, flotillin 2-CIBN-mCherry and AXL-Halo were imaged for 8 seconds before 488nm illumination. Then, cells were globally illuminated by 20 pulses (1 pulse/s, 100 ms time length for each) of 488nm-light to stimulate and visualize CRY2. During and after illumination, flotillin 2-CIBN-mCherry and AXL-Halo were continuously imaged. Two examples of flotillin 2/AXL-positive clusters induced by CRY2 oligomerization initiated by illumination are indicated (closed arrow). Co-localization events between flotillin 2-CIBN-mCherry and AXL-Halo are also visible independently of CRY2 oligomerization before illumination and correspond mostly to AXL-containing vesicles positive for flotillin 2 passing through the 200 nm depth of field illuminated by TIRF. Thanks to the high concentration of flotillin 2-CIBN-mCh in these vesicles, CRY2 translocation could be observed. Scale bar: 2 µm.

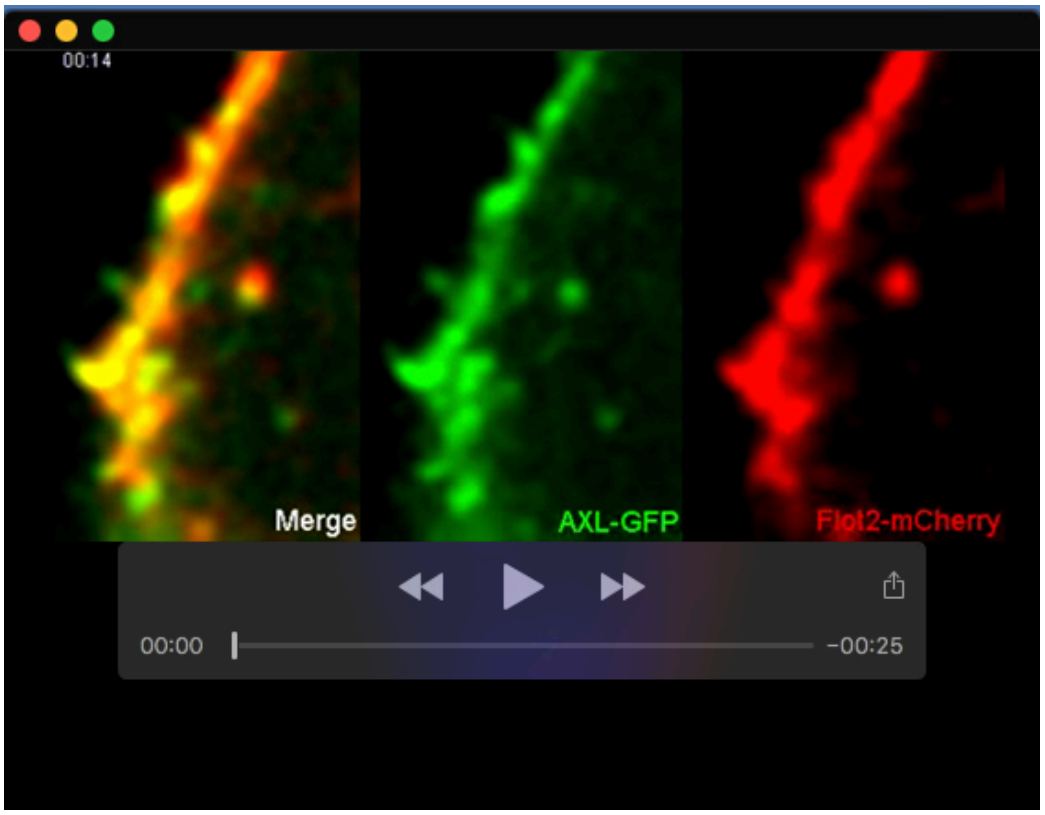

Movie 2. *Co-endocytosis of flotillin 2 and AXL after their co-accumulation at the plasma membrane.* MCF10AF1F2 cells that co-express flotillin 1-HA, flotillin 2-mCherry and AXL-GFP were imaged by spinning disk confocal microscopy (1 frame/1.3 s. Scale bar: 2.5 µm). Arrows indicate the site of co-accumulation of AXL and flotillin 2 and then the emerging endocytic vesicle.

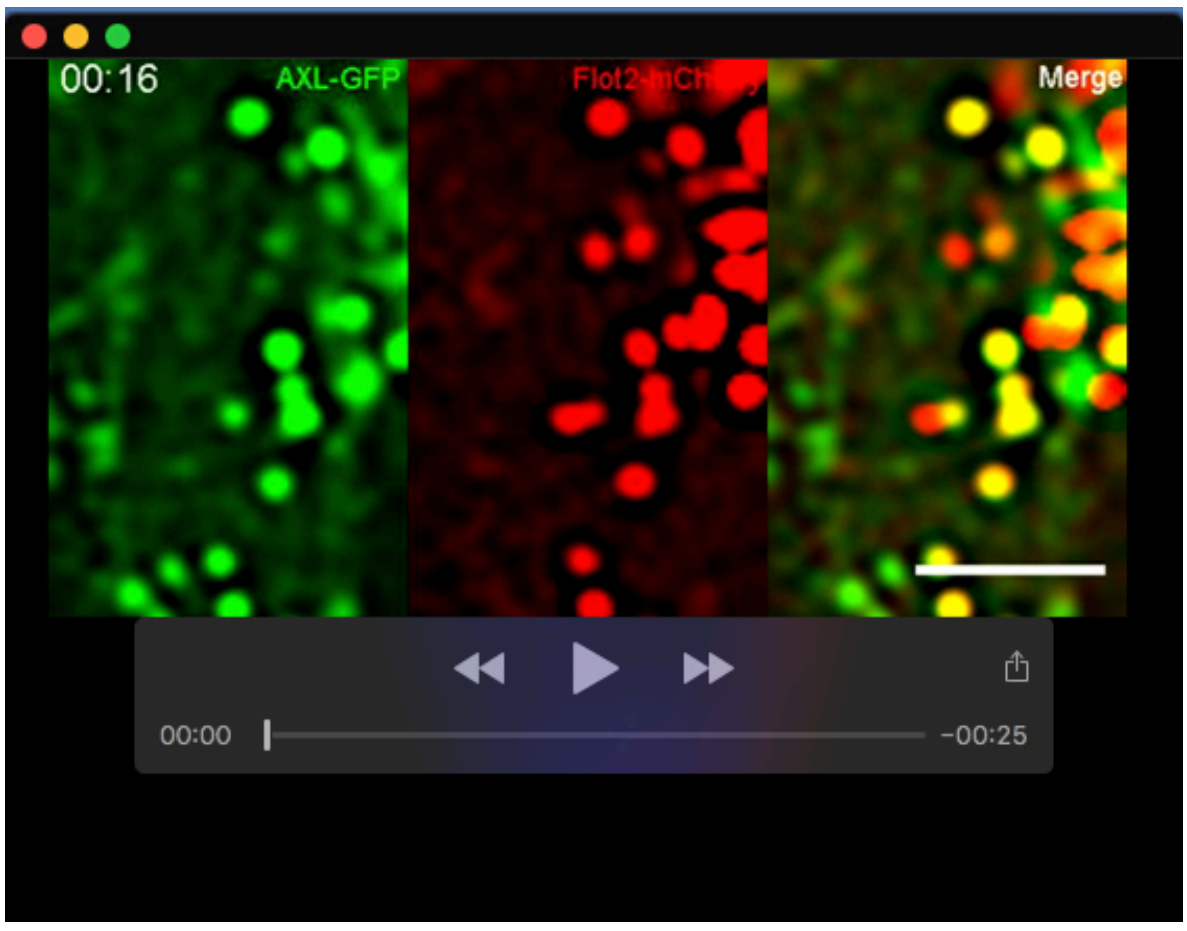

Movie 3. *Flotillin 2 and AXL colocalize in intracellular vesicles.* MCF10AF1F2 cells that co-express flotillin 1-HA, flotillin 2-mCherry and AXL-GFP were imaged by spinning disk confocal microscopy; 1 frame/1.3 s. Scale bar: 5 µm.

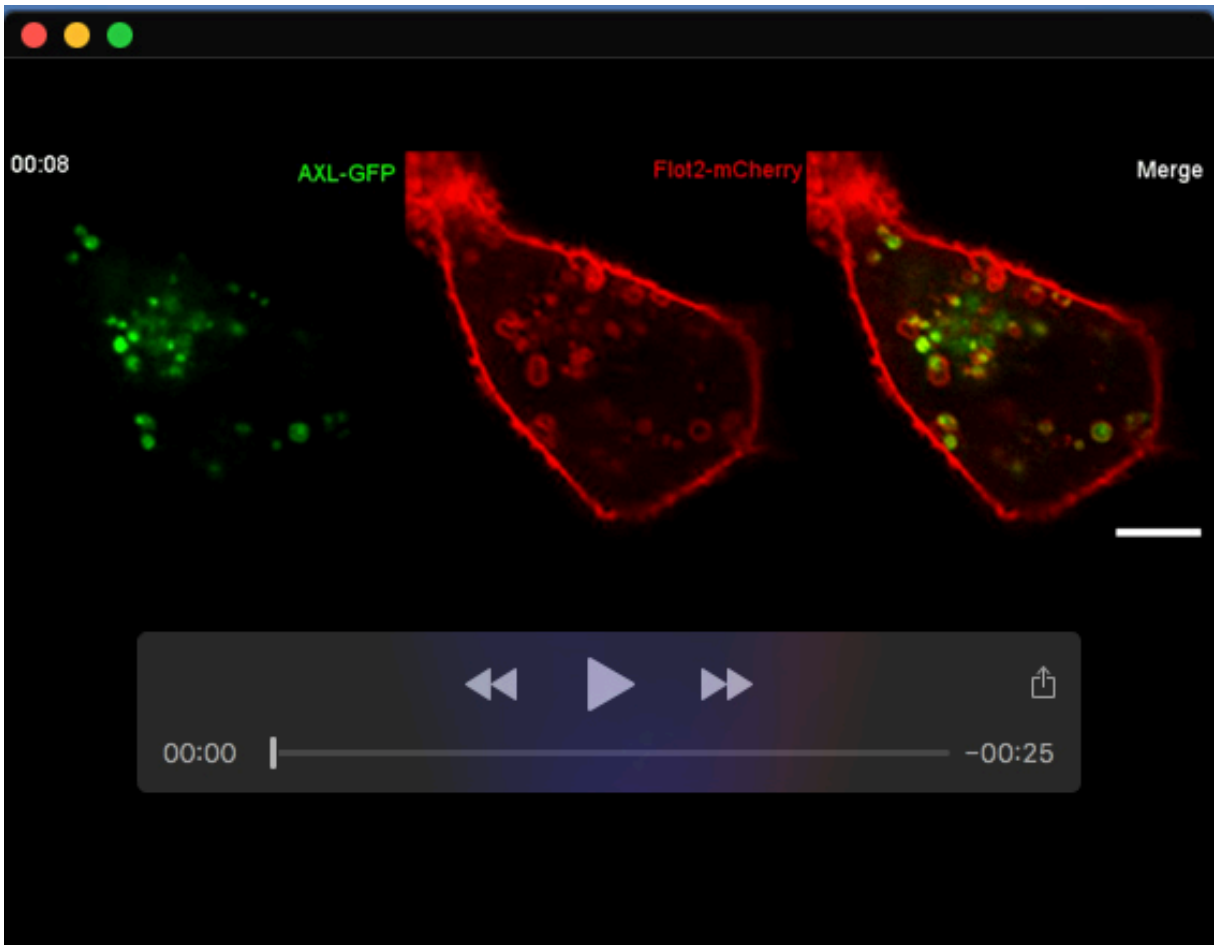

Movie 4. *Flotillin 2 and AXL colocalize in intracellular vesicles in tumor cells.* One MDA-MBA-MB-231 cell that co-expresses flotillin1-HA, flotillin-2-Cherry and AXL-GFP was imaged by spinning disk confocal microscopy; 1 frame/0.8 s. Scale bar: 10µm.

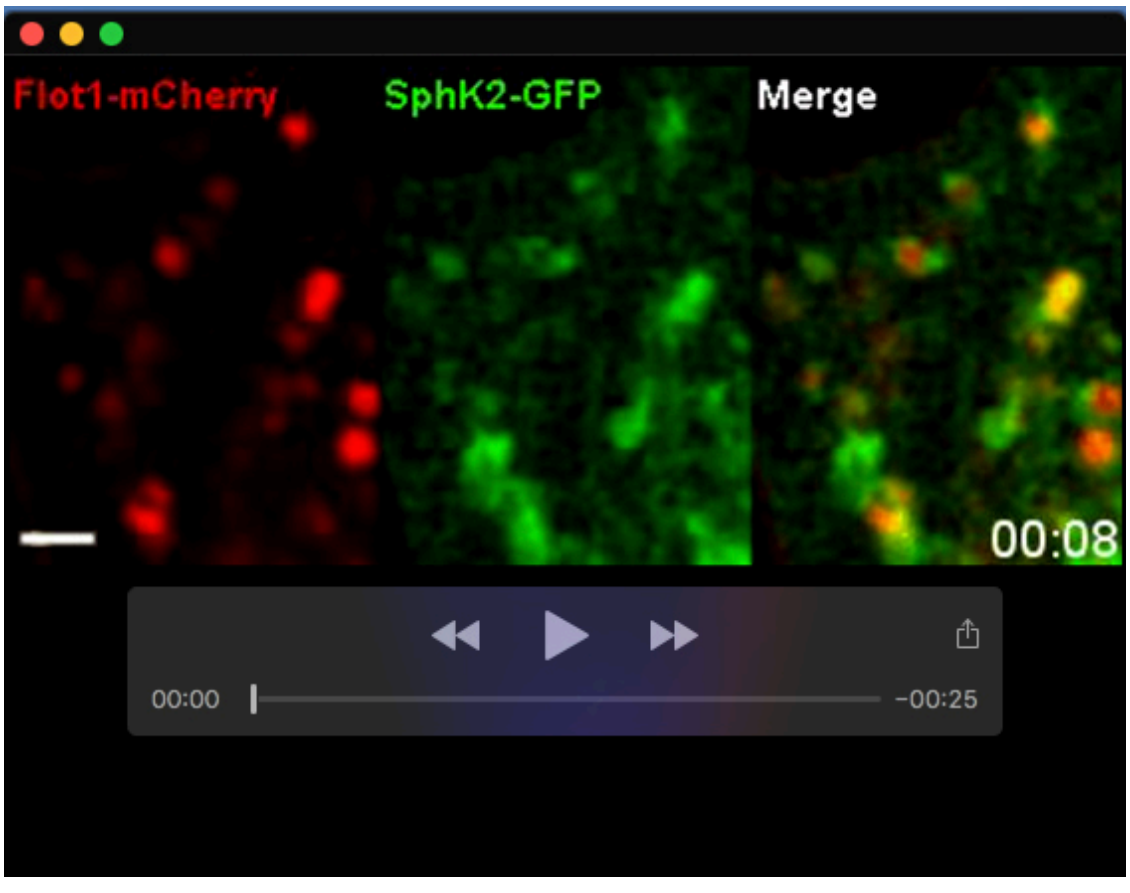

Movie 5. *SPHK2 is abundant in flotillin-positive late endosomes in MDA-MB-231 cells.* Movie of the boxed area shown in figure 5C acquired by spinning disk confocal microscopy of one MDA-MB231 cell that co-expresses flotillin 1-mCherry and SPHK2-GFP (1 frame/s. Scale bar: 2 µm).

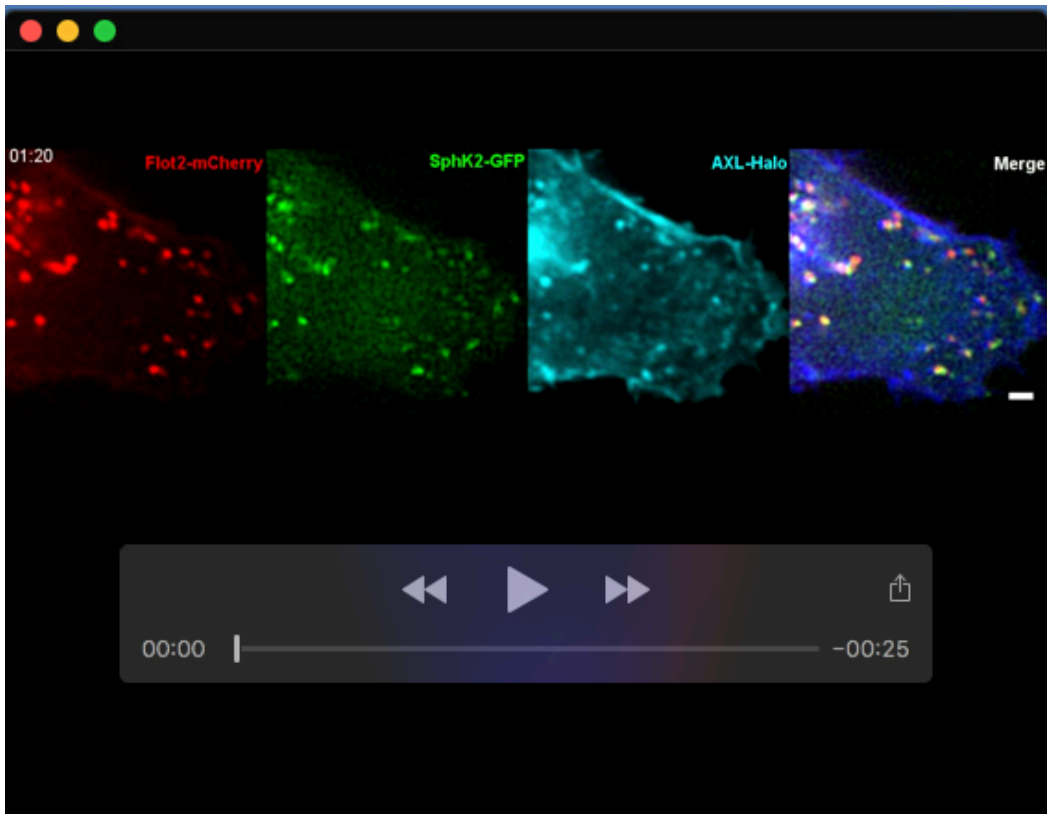

Movie 6. *Co-localization and co-trafficking of AXL-Halo, SPHK2-GFP and flotillin 2-mCherry in one MCF10AF1F2 cell.* Movie acquired by spinning disk confocal microscopy of one MCF10AF1F2 cell that co-expresses flotillin 2-mCherry (red), SPHK2-GFP (green) and AXL-Halo (blue) (labeled with Halo-tag-Janelia Fluor 646) (1 frame/10 s. Scale bar: 10 µm).

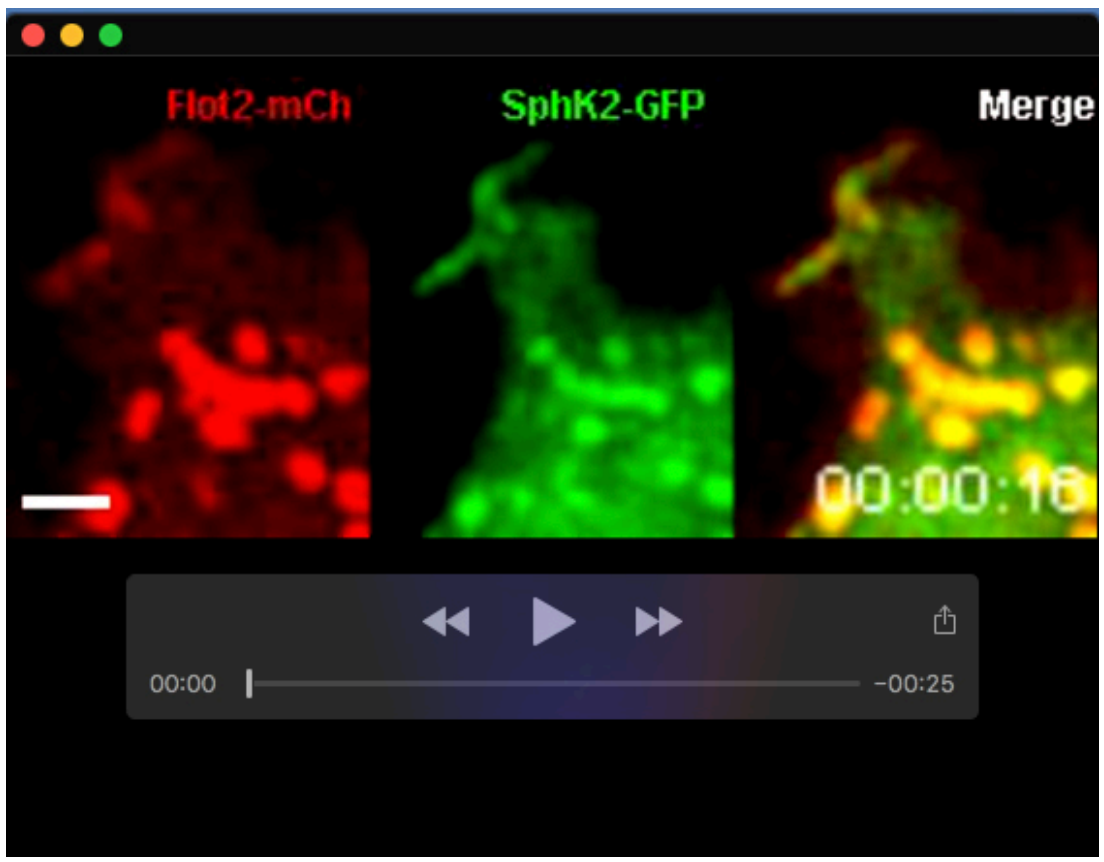

Movie 7. *Flotillin 2-mCherry/SPHK2-GFP co-endocytosis in MCF10AF1F2 cells.* Movie of the boxed area shown in figure 5E (upper panel) acquired by spinning disk confocal microscopy of one MCF10AF1F2 cell that co-expresses flotillin 2-mCherry and SPHK2-GFP (1 frame/2 s). At 34s, arrows indicate sites of flotillin 2-mCherry and SPHK2-GFP co-accumulation at the plasma membrane followed by endocytosis of a vesicle positive for both proteins. (Scale bar: 2 µm).

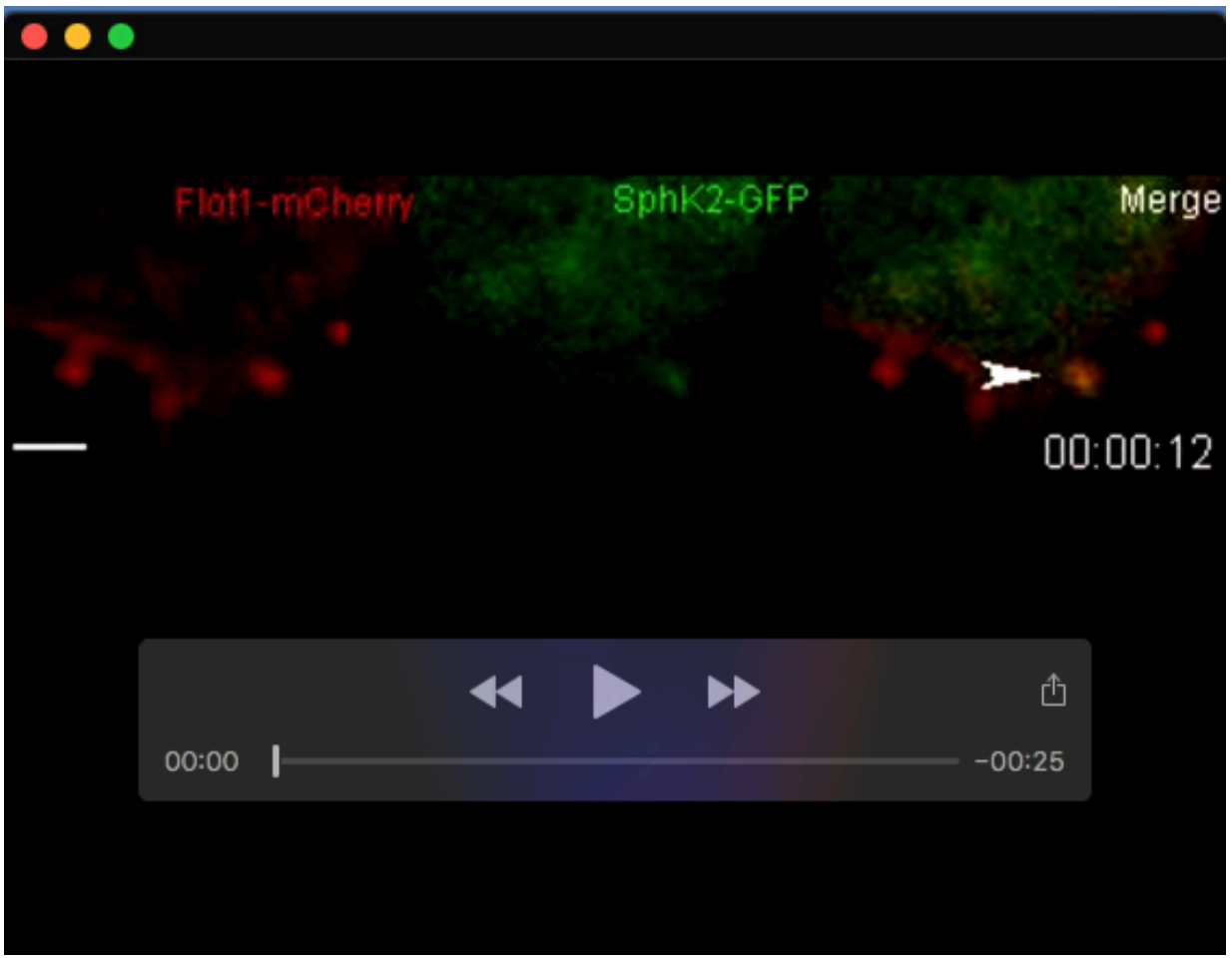

Movie 8. *Flotillin 1-mCherry/SPHK2-GFP co-endocytosis in MDA-MB-231 cells.* Movie of the boxed area shown in figure 5E (lower panel) acquired by spinning disk confocal microscopy of one MDA-MB-231 cell that co-expresses flotillin 1-mCherry and SPHK2-GFP. The arrow indicates the site of flotillin 1-mCherry and SPHK2-GFP co-accumulation at the plasma membrane followed by endocytosis of one vesicle positive for both proteins (1 frame/1 s). (Scale bar: 2 µm).

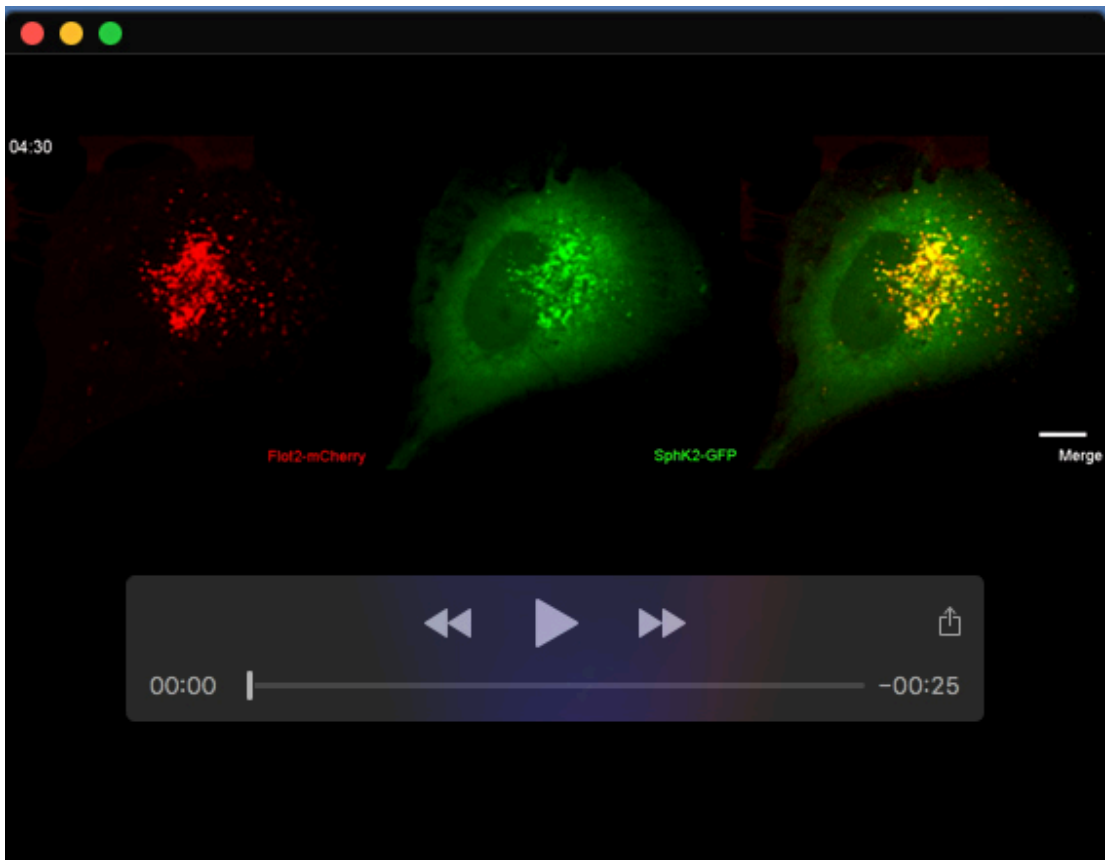

Movie 9. *Inhibition of SPHK2 catalytic activity induces its delocalization from flotillin-positive endosomes*. One MCF10AF1F2 cell that co-expresses SPHK2-GFP was imaged by spinning disk confocal microscopy immediately after addition of Opaganib (50 µM) (1 frame/30 s. Scale bar: 10 µm). The disappearance of the SPHK2-GFP signal in flotillin 2-mCherry-positive vesicles is clearly visible after 8 min and lasted for the rest of the movie (up to 28.5 min).